DESIGN AND MANUFACTURING OF DIMENSIONALLY CONTROLLED GRAPHENE BASED HYBRID STRUCTURES BY CORE-SHELL ELECTROSPINNING FOR ENERGY STORAGE SYSTEMS

by

LEILA HAGHIGHI POUDEH

Submitted to the Graduate School of Engineering and Natural Sciences

in partial fulfilment of the requirements for the degree of

Doctor of Philosophy

Sabanci University

July 2018

DESIGN AND MANUFACTURING OF DIMENSIONALLY CONTROLLED

GRAPHENE BASED HYBRID STRUCTURES BY CORE-SHELL

ELECTROSPINNING FOR ENERGY STORAGE SYSTEMS

APPROVED BY:

Prof. Dr. Mehmet Yıldız
   (Thesis Supervisor)

Asst. Prof. Dr. Bertan Beylergil

Assoc. Prof. Dr. Fevzi Çakmak Cebeci

Asst. Prof. Dr. Eralp Demir

Prof. Dr. Halit Türkmen

DATE OF APPROVAL: 30.07.2018

To my mother...

ABSTRACT

DESIGN AND MANUFACTURING OF DIMENSIONALLY CONTROLLED
GRAPHENE BASED HYBRID STRUCTURES
BY CORE-SHELL ELECTROSPINNING
FOR ENERGY STORAGE SYSTEMS

LEILA HAGHIGHI POUDEH

Materials Science and Engineering, PhD Dissertation, 2018

Thesis Supervisor: Prof. Dr. Mehmet YILDIZ

Co-Advisor: Assoc. Prof. Dr. Burcu SANER OKAN

Keywords: Graphene, energy storage systems, electrospinning, electrospraying, hybrid electrodes

In the first part of study, two-dimensional (2D) graphene oxide sheets were converted into three forms of fibers, foam, and spheres by using different carrying polymers through one-step core-shell electrospraying/electrospinning technique. In this work, graphene-based foam was produced for the first time by utilizing core-shell electrospraying technology instead of available chemical vapor deposition techniques. Electrospraying/electrospinning prevents the aggregations and crumbling of graphene sheets by constructing interconnected framework and provides homogeneous dispersion of graphene sheets in polymer solution under electric field. The proper polymer concentration and solution viscosity were determined by using Mark-Houwink-Sakurada equation. Morphology and dimension of the structures were controlled by tailoring solution and process parameters. Moreover, hollowness of the fabricated 3D graphene-based spheres was altered by changing the core solvent during process.

In the second part, platinum (Pt) decorated graphene-based spheres, foam, and fibers were prepared as electrodes *via* core-shell electrospinning/electrospraying technique followed by reduction and carbonization process. The effect of morphology and dimension of graphene-based carbon electrodes on the electrochemical behavior of electrodes were investigated by cyclic voltammetry and galvanostatic charge-discharge methods. Polyacrylonitrile (PAN) polymer was selected as a carrier to increase the interconnections in graphene network and carbon content. Among three different electrodes, Pt supported 3D graphene-based spheres exhibited the highest specific capacitance of 118 F/g at a scan rate of 1 mV/s as well as good cyclic stability owing to its unique structure and small size of Pt particles. On the other hand, Pt-decorated graphene-based fiber showed lowest specific capacitance of 8 F/g at a scan rate of 1 mV/s.

In the last part, a novel and hierarchical hybrid electrode was constructed by the addition of manganese oxide and polyaniline (PANI) into the fiber structure to further improve the electrochemical performance of graphene-based fibers. Manganese oxide with its high theoretical specific capacitance and low cost was integrated to the fiber structure during electrospinning. Whereby, at the last step of process, to enhance the electrical conductivity of electrodes, PANI was deposited on the surface of fibers through *in-situ* polymerization of aniline monomer. In order to fully understand the effect of graphene on the structure and electrochemical performance of electrodes, two types of graphene including thermally exfoliated graphene oxide (TEGO) and graphene nanoplatelet (GNP) were selected based on the number of graphene layers. Among two fabricated electrodes with different graphene sources, GNP/PANI/manganese oxide carbon fibers showed the highest specific capacitance of 454 F/g at a scan rate of 1 mV/s. The mentioned electrode exhibited a high cycling stability whereby only 11% of capacitance lost after 1000 cycles of charging-discharging. High oxygen functional groups of GNP is believed to enhance the interfacial interactions between electrode components by providing an exfoliated structure. This study especially brings a new insight into the fabrication of high-performance hybrid electrodes for energy storage devices.

ÖZET

ENERJİ DEPOLAMA SİSTEMLERİ İÇİN ÇEKİRDEK-KABUK YAPILI ELEKTRODOKUMA YÖNTEMİ İLE BOYUTSAL KONTROLLÜ GRAFEN TABANLI HİBRİT YAPILARIN TASARIMI VE ÜRETİMİ

LEILA HAGHIGHI POUDEH

Malzeme Bilimi ve Mühendisliği, Doktora Tezi, 2018

Tez Danışmanı: Prof. Dr. Mehmet YILDIZ

Tez Eş-danışmanı: Doç. Dr. Burcu SANER OKAN

Çalışmanın ilk bölümünde, iki boyutlu (2B) grafen oksit tabakaları, tek adımda çekirdek-kabuk elektrospreyleme/elektrodokuma tekniği ile farklı taşıyıcı polimerler kullanarak lif, köpük ve küre olmak üzere üç tip yapıya dönüştürülmüştür. Bu çalışmada grafen tabanlı köpük, mevcut kimyasal buhar biriktirme tekniklerinin yerine ilk defa çekirdek-kabuk elektrospreyleme teknolojisi kullanılarak üretilmiştir. Elektrospreyleme/elektrodokuma, birbirine bağlı yapı iskelesini oluşturarak grafen tabakalarının birikmesini önler ve elektrik alan altında polimer çözeltisine grafen tabakalarının homojen dağılımını sağlamaktadır. Uygun polimer konsantrasyonu ve çözelti viskozitesi, Mark-Houwink-Sakurada denklemi kullanılarak belirlenmiştir. Yapıların morfolojisi ve boyutu, çözelti ve süreç parametrelerinin uyarlanmasıyla kontrol edilmiştir. Ayrıca, 3B grafen tabanlı kürelerin boşluğu, işlem sırasında çekirdek çözücüyü değiştirerek kontrol edilmiştir.

Çalışmanın ikinci bölümünde, platin (Pt) emprenye edilerek üretilmiş grafen bazlı küreler, köpük ve lifler elektrot olarak hazırlanmış olup morfolojilerinin ve boyutlarının elektrokimyasal davranış üzerindeki etkisi siklik voltametri ve galvanostatik şarj-deşarj

yöntemleri ile incelenmiştir. Polialklonitril (PAN) polimeri hem grafen ağındaki hem de karbon içeriğindeki ara bağların arttırılması için taşıyıcı olarak seçilmiştir. Üç farklı elektrot arasında, Pt destekli 3B grafen bazlı küreler, eşsiz yapısı ve küçük boyutlu Pt parçacıklarına bağlı olarak 1 mV/s'lik bir tarama hızında 118 F/g'lik en yüksek özgül kapasiteyi ve iyi döngüsel stabiliteyi sergilemiştir. Diğer taraftan, Pt ile dekore edilmiş grafen bazlı fiber, 1 mV/s'lik bir tarama hızında 8 F/g'lık en düşük spesifik kapasitans göstermiştir.

Bu tezin son bölümünde, grafen bazlı fiberlerin elektrokimyasal performansını daha da arttırmak için manganez oksit ve polianilin (PANI) ilavesiyle yeni ve hiyerarşik bir hibrit yapı oluşturulmuştur. Yüksek teorik özgül kapasitansı ve düşük maliyeti ile manganez oksit elektrodokuma sırasında lif yapısına entegre edilmiştir. Bununla birlikte, işlemin son aşamasında elektrotların elektrik iletkenliğini arttırmak için, PANI polimer anilin monomerinin *in-situ* polimerizasyonu yoluyla fiberlerin yüzeyi üzerinde biriktirilmiştir. Grafenin elektrotun yapısı ve elektrokimyasal performans üzerindeki etkisini tam olarak anlamak için, tabaka sayısına göre termal olarak genleştirilmiş grafen oksit (TEGO) ve grafen nano tabakalar (GNP) içeren iki farklı tip grafen seçilmiştir. GNP/PANI/manganez oksit karbon fiberleri, 1 mV/s'lik bir tarama hızında 454 F/g yüksek spesifik kapasitans göstermiştir. Bahsedilen elektrot, 1000 devir şarj-deşarjından sonra kapasitenin sadece % 11'ini kaybetmiştir. GNP'de bulunan yüksek miktardaki oksijen fonksiyonel grupları, pul pul dağıtılmış bir yapı sağlayarak elektrot bileşenleri arasındaki ara yüzey etkileşimlerini iyileştirdiği düşünülmektedir. Bu çalışma, özellikle enerji depolama cihazları için yüksek performanslı hibrit elektrotların üretilmesine yeni bir bakış getirmektedir.

ACKNOWLEDGEMENTS

TABLE OF CONTENTS

LIST OF FIGURES

LIST OF TABLES

CHAPTER 1 **STATE-OF-THE-ART**

Graphene, a two-dimensional (2D) hexagonal lattice of sp^2 carbon atoms, has been the interest of many studies. The long-range π-conjugation in graphene yields intriguing properties such as high electrical and thermal conductivity [1], [2], large surface area [3], good chemical stability [4] and excellent mechanical strength [5] which makes it a great candidate in various applications such as energy storage systems, polymer composites, and sensors [3]. However, in practical applications, 2D graphene sheets tend to restack together due to strong π-π interactions and van der Waals forces, which lead to a significant decrease in electrical conductivity and surface area, and this affects negatively the utilization of graphene in many fields. To overcome this problem and provide advanced functions with improved performance, several graphene structures such as graphene networks [6], graphene fibers [7], and graphene spheres [8] have been constructed mainly by chemical vapor deposition (CVD), self-assembly, and template assisted methods. The combination of these structures and intrinsic properties of graphene provides high surface area, excellent mechanical strength, and fast mass and electron transport for graphene architectures.

Nevertheless, there are still some challenges in the production of graphene-based architectures. For instance, the size of constructed structures and their properties strongly depend on the building blocks (e.g. templates). Besides, the aforementioned techniques include many post-treatment steps as well as harmful chemicals. Therefore, there is a need to design new and feasible approaches that can prevent the re-stacking of graphene layers.

Taking these into account, core-shell electrospraying/electrospinning technique becomes an ideal approach for the fabrication of graphene-based structures since it is possible to attain multi-functionality and utilize different materials in one-step process by eliminating deposition steps as in the self-assembly and template-assisted methods [8], [9]. This technique brings an advantage in the energy-related areas since the electrodes produced *via* this method have ability to form a continuous network, which is essential for

the charge transport, and provide conducting framework and excellent interconnectivity. Moreover, this technique makes it possible to fabricate novel hybrid materials by the combination of graphene's high surface area and its excellent electrical conductivity with active materials' large specific capacity and high energy density.

In the first part of study, we designed a straightforward route for the converting 2D graphene sheets to 3D graphene spheres by using core-shell electrospraying technique [8]. To this end, PAN, PMMA, and PS polymers were used as templates and inhibited the agglomeration of graphene sheets by crawling into graphene layers forming intercalated structure. The appropriate polymer concentration for the sphere formation was determined by using Mark-Houwink-Sakurada equation. The hollowness of spheres was controlled by changing the core solvents. Moreover, the connectivity of graphene sheets in polymeric shell was improved by increasing carbon networks after carbonization process. Thus, graphene-based carbon spheres with controlled hollowness became an ideal structure for the electrode materials.

In the next step, in addition to graphene spheres, graphene-based fibers and foam structures were also fabricated through the same method and their electorchemical performances were investigated in details. In the electrospraying/electrospinning techniques, the final morphology is affected by various solution properties (such as viscosity and electrical conductivity) and process parameters (such as voltage, and flow rate) [10]. It is worth noting that graphene-based foam was produced for the first time by utilizing core-shell electrospraying technology instead of other available techniques like CVD. To further increase the catalytic activity of composites, platinum nanoparticles (Pt) were decorated on the surface of graphene-based spheres, fibers, and foam. Electrochemical results revealed that Pt decorated 2D graphene sheets as electrode materials did not show any capacitance behavior whereas the integration of graphene into 1D fibers and 3D foam and spherical structures in carbon network significantly improved the capacitance characteristics.

Graphene-based electrodes unlike their good power density, suffer from low energy density and poor capacitance. To solve this problem and enhance the electrochemical performance of fabricated composites, transition metal oxides and electrically conductive polymers can be integrated into graphene-based composites by fabricating a hybrid structure and thus fully utilize the advantages of each component in the combined system. Specifically, electrospun graphene-based fibers with their interconnected mesoporous texture provides a platform for the post-synthesis and integration of various *in-situ* materials like PANI into the fiber structure [11]. Therefore, in the last chapter of thesis, manganese oxide and PANI were integrated to the graphene-based fibers due to their high theoretical specific capacitance, low cost, and fast redox rate [12]. As the last attempt and to fully understand the effect of graphene on the structure and electrochemical performance of electrodes, two different types of graphene including thermally exfoliated graphene oxide and graphene nanoplatelets were added to the fibers based on the number of graphene layers and surface oxygen functional groups. Graphene with single nanoplatelets and higher surface oxygen functional groups exhibited enhanced performance due to the improved interfacial interactions between polymer matrix and other hybrid components. Consequently, ternary hybrid composites of PANI-manganese oxide- graphene nanoplatelets embedded carbon fibers exhibited a remarkable capacitance improvement when compared to other reported composites.

Material from this dissertation has been published in the following forms and a paper as well as a book chapter are under submission and publication processes:

L. Haghighi Poudeh, B. Saner Okan, J. Seyyed Monfared Zanjani, M. Yildiz, and Y. Z. Menceloglu, "Design and Fabrication of Hollow and Filled Graphene-based Polymeric Spheres via Core-Shell Electrospraying," *RSC Adv.*, vol. 5, pp. 91147–91157, 2015. (Published)

L. Haghighi Poudeh, D. Cakiroglu, F. Ç. Cebeci, M. Yildiz, Y. Z. Menceloglu, and B. Saner Okan, "Design of Pt-Supported 1D and 3D Multilayer Graphene-Based Structural Composite Electrodes with Controlled Morphology by Core–Shell

Electrospinning/Electrospraying," *ACS Omega*, vol. 3, no. 6, pp. 6400–6410, 2018. (Published)

L.Haghighi Poudeh, F. Ç. Cebeci, Y. Z. Menceloglu, M, Yildiz, B. Saner Okan, "Free-Standing Hierarchical Hybrid Electrodes Based on PANI Coated Mn_3O_4/Graphene Embedded Carbon Fibers for High Performance Supercapacitors" (Submission process)

L.Haghighi Poudeh, M. Yildiz, Y. Z. Menceloglu, B. Saner Okan," Three Dimensional Graphene-based Structures: Production Methods, Properties and Applications" Graphene- Growth, Synthesis and Integration Methods, Handbook on the Graphene Materials, WILEY-Scrivener Publisher, USA, 2018. (Accepted-under publication)

CHAPTER 2 **LITERATURE REVIEW**

2.1 Preparation of graphene

Graphene was first fabricated via micromechanical exfoliation of graphite [13]. By using this approach, it is possible to obtain single or few-layer graphene sheets with high quality. However, this technique is not suitable for mass-production. To address this problem, several alternative techniques including bottom-up and top-down approaches have been developed in order to synthesis 2D graphene sheets. Epitaxial growth [14] and chemical vapor deposition (CVD) method [15] are the most widely used bottom-up techniques whereas top-down approach includes electrochemical exfoliation [16] and chemical exfoliation of graphite oxide [17]. Among top-down methods, chemical approach has attracted great interest because of easy processability and large-scale production thus it could be utilized in many applications [18]. On the other hand, chemically derived 2D graphene sheets is the main component for the construction of 3D graphene structures [19]. This technique involves the oxidation of graphite, followed by the exfoliation process in order to obtain graphene oxide (GO) [20]. Figure 2.1 shows the schematic representation of the different methods for the fabrication of graphene [21]. Many studies have focused on the oxidation of graphite into graphite oxide. Brodie [22], first reported the synthesis of graphite oxide in the presence of potassium chlorate and nitric acid. Later, Staudenmaier [23] improved the procedure by adding concentrated sulfuric acid (H_2SO_4) to the mixture. However, this method was time consuming and hazardous. In 1958, Hummers [24] used a combination of potassium permanganate and concentrated H_2SO_4 in the presence of sodium nitrate. So far Hummers method with some modifications and improvements is the most common used route for the synthesis of graphite oxide [25], [26]. The synthesized graphite oxide is then exfoliated into single- or few-layered GO sheets dispersed in aqueous solutions or expanded by applying heat-treatment [27]. Finally, graphene oxide is reduced to graphene sheets by applying thermal annealing [28] or using reducing agents such as hydrazine [29], hydroquinone [30], sodium borohydride [31].

2.2 Preparation methods of 3D graphene architectures

In the past few years, large efforts have been devoted to the utilization of 3D graphene materials with different morphologies and functionalities. In this section, the preparation methods of 3D graphene structures are classified as assembly of GO sheets by using different techniques and direct deposition of 3D graphene architectures through CVD. All the methods and recent studies have been discussed in details.

2.2.1 Assembly of GO sheets

Assembly method is one of promising strategies for the construction of 3D graphene architectures because of its distinct advantages including high yield, low-cost, and easy functionalization of graphene [32]. In this technique, GO solution is preferred over graphene since GO behaves like an amphiphilic material with hydrophilic edges and hydrophobic basal plane [33]. Therefore, it could easily make a stable dispersion in aqueous solutions. At the final step of assembly technique and in order to obtain 3D graphene architectures, GO sheets are reduced whether by chemical routes or thermal annealing to the reduced graphene (rGO) [34]. It should be noted that the driving force behind formation of the 3D graphene architectures *via* assembly method is the interactions like van der Waals forces, hydrogen bonding, dipole interactions, electrostatic interactions and π-π stacking [35].
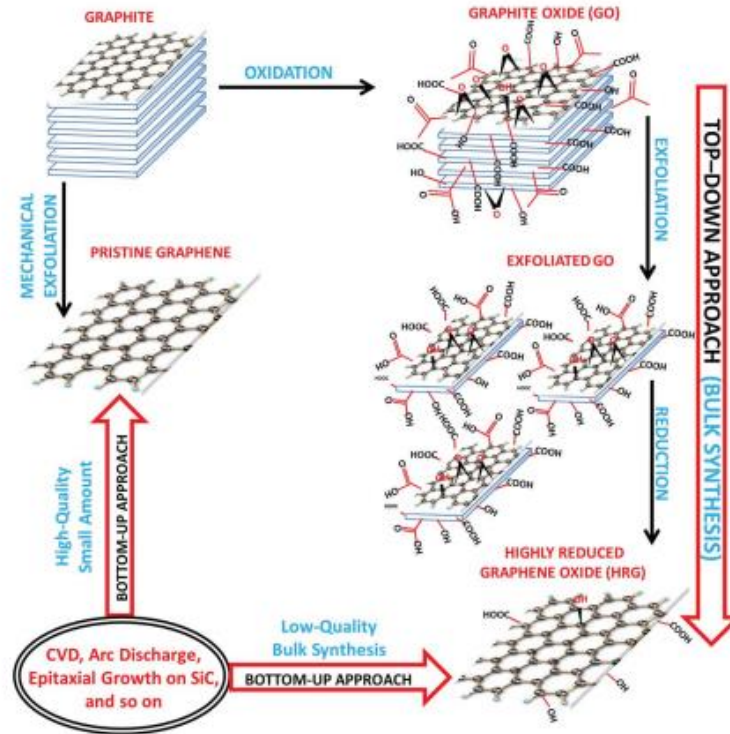
Figure 2.1 Schematic representation of the methods used for the synthesis of graphene [21].

2.2.2 Self-assembly method

Self-assembly is one of the most-widely used techniques that converts 2D graphene sheets to 3D macroscopic graphene architectures with different functionalities. The obtained structures have great potentials to be used in various applications such as energy storage devices [36], medicine [37], optoelectronics [38]. In this technique, 3D graphene structures are obtained through the gelation of GO dispersion followed by the reduction process of GO to rGO [34]. Basically, in colloidal chemistry gelation is occurred when the electrostatic forces between colloids are changed [39]. In the case of stable GO dispersion, there is a force balance between the van der Waals attractions of GO basal planes and the repulsion forces of functional groups of GO sheets. Once this force balance is broken, gelation process is started and subsequently GO sheets overlap and form different GO morphologies such as hydrogels, organogels, or aerogels which are physically or chemically linked to each other [40], [41]. At the final step, GO hydrogels

reduced to form 3D graphene networks. There are many ways to initiate the gelation process of a stable GO dispersion. For example, additive-free GO hydrogels was fabricated by changing the pH of dispersion [34] and applying ultrasonication technique [42]. During sonication, GO sheets fractured to the smaller sheets. As a result, produced new edges contain non-stabilized carboxyl groups. This change in the surface of GO initiate the gelation (Figure 2.2). Moreover, the addition of cross-linkers like polyvinyl alcohol (PVA) [43], DNA [44], and metal ions [45] to the solution can trigger the gelation process. Bai and co-workers [43] reported the synthesis of GO hydrogel by the addition of PVA, a water-soluble polymer, as cross-linker to the aqueous GO solution. The hydrogen bonding interactions between hydroxyl-rich polymeric chains and oxygen functional groups of GO form cross-linking sites and thus fabricate GO hydrogels.
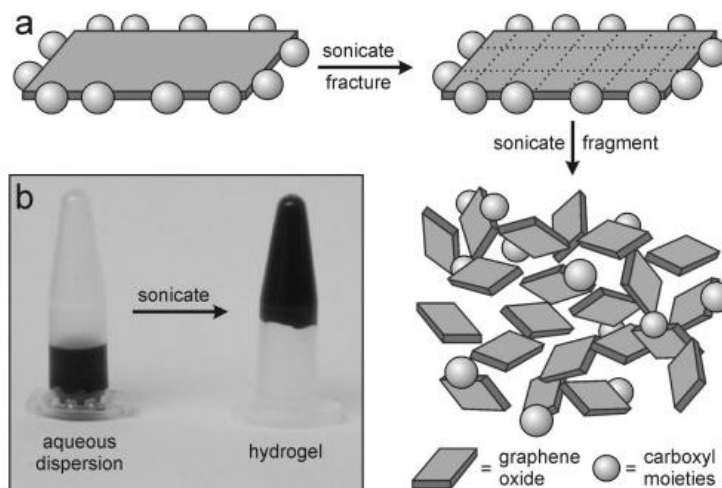
Figure 2.2 (a) Diagram illustrating the fracture and fragmentation of GO sheets during sonication, (b) Digital image demonstrating the conversion of an as-prepared aqueous graphene oxide dispersion (left) into a hydrogel (right) after sonication [42].

On the other hand, 3D graphene architectures can be directly obtained by the self-assembly of GO sheets *via* hydrothermal or chemical reduction processes. In these techniques, GO sheets are directly self-assembled and reduced to rGO at the same time [40]. For instance, an electrically conductive and porous 3D graphene network have been prepared *via* mild chemical reduction of GO by sodium bisulfide at 95 °C under atmospheric pressure and in the presence of iron oxide nanoparticles [46]. He *et al.* [47]

reported the facile fabrication of 3D graphene sponges containing palladium and indium by combination of the hydrothermal and chemical reduction techniques. In this study, GO aqueous solution containing palladium and indium salts and vitamin C as reducing agent were treated hydrothermally at 110 °C for 6 h.

Generally, after gelation and reduction of 3D graphene architectures, a drying procedure is needed to remove the water and organic molecules from the structure while preserving the main framework [48]. Freeze drying as one the feasible drying techniques, is usually applied as the final step of the assembly methods. By using this technique, it is possible to fabricate highly porous structures with improved mechanical and electrical properties since the pores size could be controlled by monitoring the process parameters like temperature [49]. Figure 2.3 shows the SEM images of 3D graphene structures which are freeze-dried at different temperatures [49].
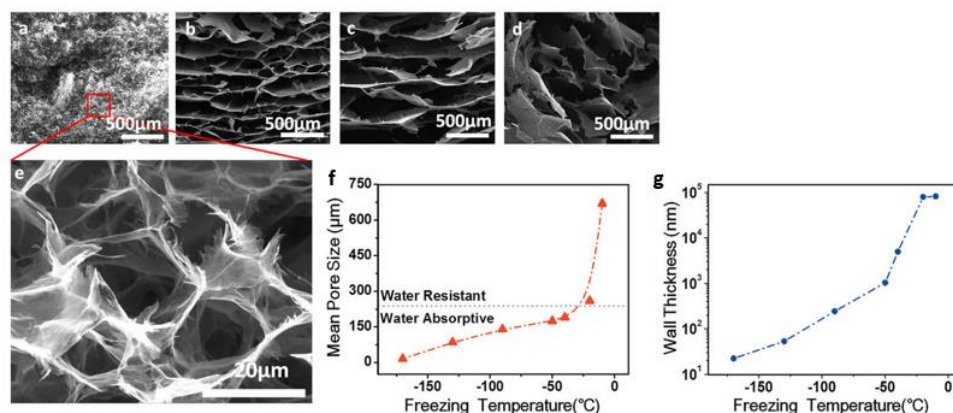
Figure 2.3 (a-d) Microstructures of sponge graphenes frozen at different temperatures (e) SEM image of the pore walls composed of graphene nanosheets corresponding to panel a. The mean thickness of the pore walls is 10 nm, (f) statistics of the average pore size, and (g) wall thickness as a function of freezing temperature [49].

Alternatively, electrochemical reduction as a well-known route is usually used to deposit active materials like 3D graphene architectures on the surface of the electrodes [50]. Chen *et al.* [51] fabricated 3D porous graphene-based composites involving two electrochemical deposition steps. As shown in Figure 2.4, GO sheets were first electrochemically reduced to a porous 3D graphene framework and then three different

components as conductive polymers, noble metals, and metal oxides were integrated to the 3D porous graphene network, separately via *in-situ* electrochemical deposition. Electrochemically deposited 3D graphene-based architectures can be directly used in the electrochemical devices as high performances electrode materials.
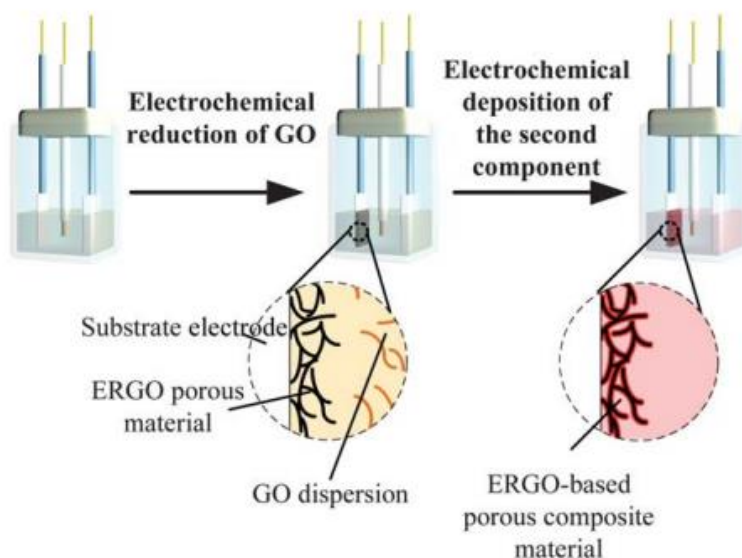
Figure 2.4 Schematic illustration of the self-assembly of GO sheets using electrochemical deposition [51].

2.2.3 Template-assisted method

3D graphene architectures can be fabricated with another feasible and convenient way by using pre-designed 3D templates such as polystyrene (PS) [52], and silicon dioxide (SiO_2) [53] following by the reduction of GO and removing the template from the structure. Generally, the used template is surrounded by the graphene sheets due to the electrostatic interactions between negatively charged graphene sheets and positively charged template. Compared to self-assembly strategy, by using this technique it is possible to obtain more controlled structure with desirable morphology [40]. However the size of architectures directly depends on the size of templates [8]. So far, considerable amounts of works have focused on the production of 3D graphene-based materials using template-assisted method. In one of the works, as shown in Figure 2.5a, positively charged

PS spheres as template were coated with GO sheets followed by the reduction of GO to rGO by using hydrazine. Finally graphene hollow spheres were fabricated after calcination at 420 ˚C for 2h to remove PS from the core [54]. Wu *et al.* [55] reported a facile synthesis route for the fabrication of graphene-based hollow spheres as electrocatalysts for oxygen reduction. As shown in Figure 2.5b, strong electrostatic interactions between polyethylenimine functionalized SiO_2 spheres and graphene sheets results in the formation of GO-SiO_2 spherical particles. After reduction process and washing with hydroflouric acid, graphene-based hollow spheres were obtained.
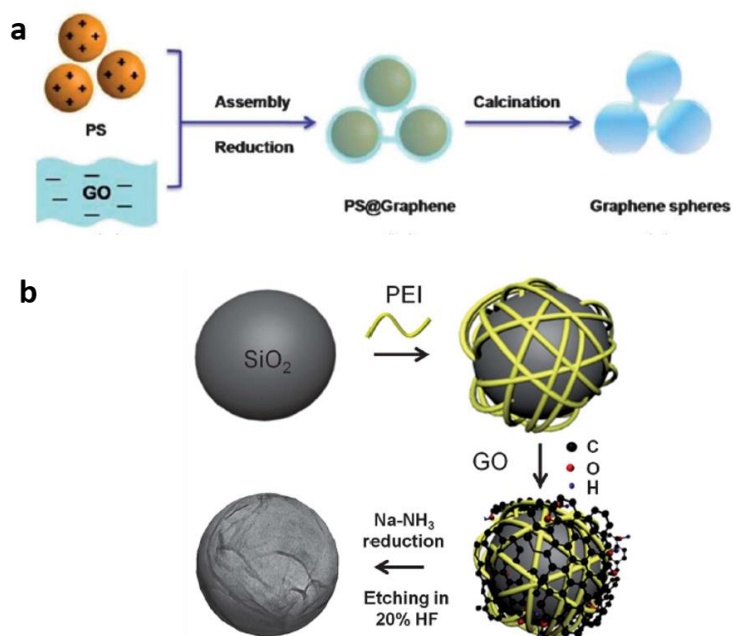
Figure 2.5 Schematic illustrations of the fabrication procedure of graphene-based hollow spheres using (a) PS [54] and (b) SiO_2 [55] as templates.

In an effort to produce 3D graphene architectures with more controlled manner, Huang and co-workers [56] reported a facile assembly method of porous graphene foams with controlled pore sizes by the help of hydrophobic interactions of GO sheets and functionalized SiO_2 spherical templates followed by the calcination and silica etching. Figure 2.6 represents the schematic illustration of synthesis procedure of the nanoporous graphene foam with a controllable pore size of 30-120 nm.
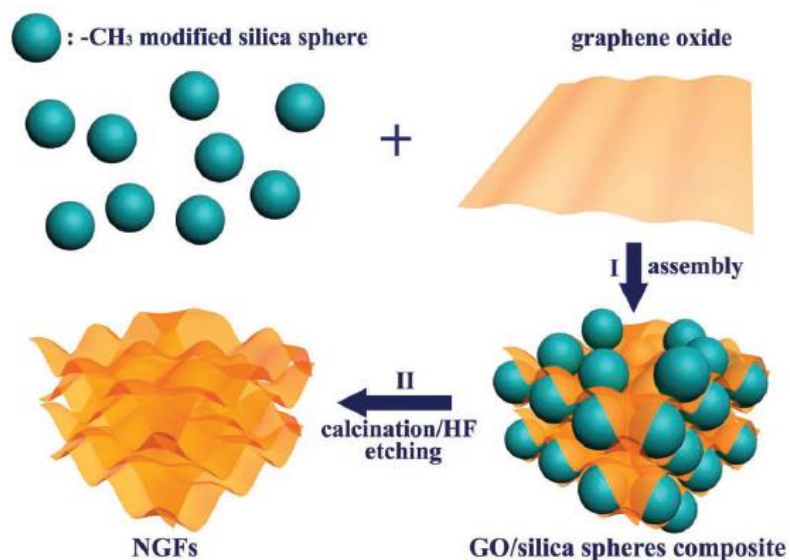
Figure 2.6 Schematic illustration of the synthesis procedures of the nanoporous graphene foams [56].

2.2.4 Electrospraying

Electrospinning/electrospraying is a simple and well-known technique to produce graphene-based fibers and spherical or bead-like structures with the diameters ranging from few micrometers to nanometer by adjusting the process parameters. In this process, a strong electric field is applied between a nozzle containing graphene-based solution and grounded metallic-plate as a collector. When the surface tension of solution at the tip of the nozzle is overcome to the electric field, the droplet stretches and forms a continuous jet which is collected as graphene-based fibers or spherical structures on the collector [57].

More recently, core-shell electrospinning/electrospraying has received great attention due to its possibility to attain multi-functionality and utilize different materials in one-step process by eliminating deposition steps as in the self-assembly and template-assisted methods and thus it expands the potential applications of fabricated structures in many areas including drug delivery, energy storage, sensors, and nanocomposites [8], [9]. In this technique, the final morphology is affected by various solution properties (such as viscosity and electrical conductivity) and process parameters (such as voltage, and flow

rate) [10]. Up to now there are lots of attempts for the integration of graphene into fiber structure using both classic and core-shell electrospinning technology [58]–[60]. However very recently, Poudeh *et al.* [8] proposed a new design of 3D graphene-based hollow and filled polymeric spheres through one-step core-shell electrospraying technique. In this study, the proper polymer concentration for the sphere production were determined by using Mark–Houwink–Sakurada equations since proper polymer concentration and solution viscosity are required in order to obtain desired spherical morphology. In the case of hollowness, core material should contain a solvent with a high vapor pressure than the shell solution. Figure 2.7 represents the schematic illustration of fabrication of graphene-based spheres using core-shell electrospraying method, which eliminates crumbling and agglomeration problem of 2D graphene sheets and provides better dispersion of graphene layers through polymer chains. The possible interactions between the polymeric chains and graphene sheets during sphere formation are also shown in Figure 2.7 (left).
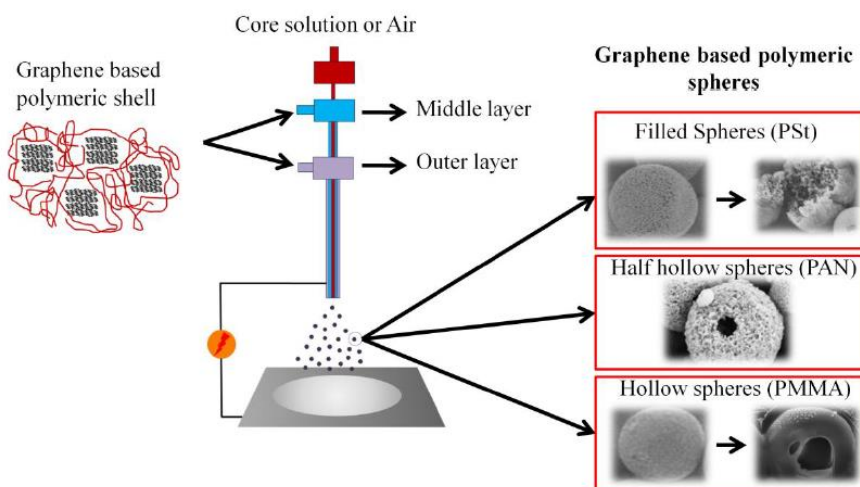
Figure 2.7 Schematic illustration of fabrication of 3D graphene-based spheres using core-shell electrospraying technique and (left) possible interactions between polymeric chains and graphene sheets during sphere formation [8].

2.3 Direct deposition of 3D graphene structures

Chemical vapor deposition (CVD) is a convenient method for the construction of 3D porous graphene networks with superior properties such as large surface area and high

electrical conductivity comparable to that of pristine graphene [15]. Over and above this, in the aforementioned 3D graphene synthesis routes, chemically derived graphene is the starting material and since during oxidation and reduction process of GO some defects are introduced to the system, the fabricated 3D graphene structures would exhibit low electrical conductivity when compared to 3D graphene structures growth with CVD. In this method, graphene directly grows from organic precursors on a substrate [61]. Compared to the classic CVD process, which uses flat metal substrates as template and is able to produce a low amount of graphene, 3D graphene architectures can be fabricated by using different 3D templates like nickel foam in large quantities [40].

Pioneered by Chen *et al.* [62], they reported a general strategy for the growth of graphene films directly on the 3D nickel template by decomposition of methane (CH_4) at 1000 ˚C under ambient pressure. The wrinkles present in the surface of graphene film, which is due to the difference between thermal expansion coefficients of nickel and graphene, provide better interactions of graphene films with polymers. Therefore, a layer of poly(methyl methacrylate) was easily deposited on the surface of fabricated graphene films in order to preserve the graphene network during etching the template. Lastly, nickel scaffold was etched in hydrochloric acid or iron chloride solution and then immersed in hot acetone to remove polymeric layer. Figure 2.8 shows the schematic illustration of production of 3D graphene foam by using nickel template.

It should be noted that the surface area of fabricated 3D graphene networks depends on the number of layers in the graphene film [63]. For instance, a high surface area of 850 m^2/g was reported in the case of three layer graphene foam [62]. Another important parameter is the pore size of the chosen templates since it directly affect the final properties of graphene foam [63]. Therefore, along with the 3D nickel foam, other template precursors have been explored. In one of the studies, 3D graphene was growth on an anodic aluminum oxide template with an average pore size of 95 nm at a temperature of 1200 ˚C for 30 minutes under the flows of argon, hydrogen, and methane [64]. Ning *et al.* [65] demonstrated that by using a porous MgO layer as template and methane as carbon precursor, one to two graphene layers with an extraordinary large surface area of 1654

m^2/g and an average pore size of 10 nm were formed on the surface of the template. In addition to the above-mentioned templates, the use of other templates such as metallic salts were also reported [66], [67]. Over and above this, in order to tailor the pore size of 3D graphene foam, Ito *el al.* [68] designed a novel nanoscale nickel template by electrochemically leaching manganese from a $Ni_{30}Mn_{70}$ precursor in a weak acid solution. Three dimensional graphene foam with a pores size of 100 nm to 2.0 μm was achieved by controlling the size of nickel ligaments by monitoring CVD time and temperature.
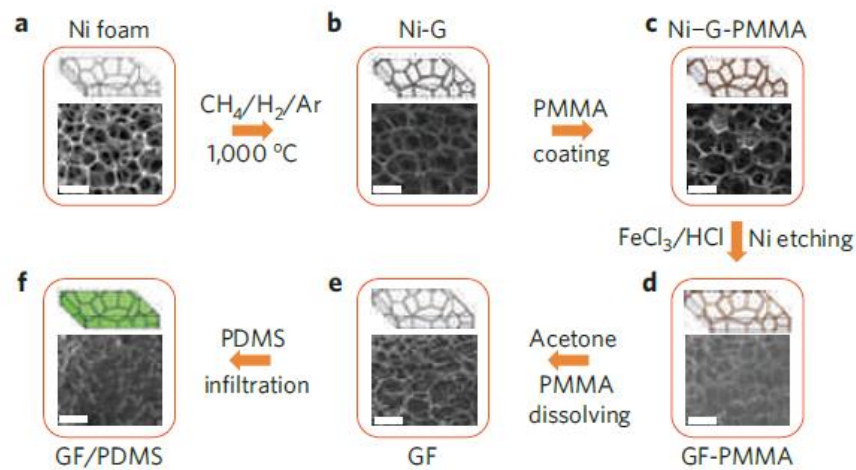
Figure 2.8 Synthesis of 3D graphene foam (GF) and integration with poly(dimethyl siloxane) (PDMS). (a-b) CVD growth of graphene films using nickel foam as the 3D scaffold template, (c) An as-grown graphene film after coating a thin PMMA supporting layer, (d) A GF coated with PMMA after etching the nickel foam with hot HCl, (e) A free-standing GF after dissolving the PMMA layer with acetone, and (f) A GF/ PDMS composite after infiltration of PDMS into a GF [62].

As an alternative approach, the non-template direct deposition of 3D graphene networks through plasma-enhanced CVD method was also reported. By using methane as carbon source and substrates like gold and stainless steel, graphene sheets were firmly adhered to the substrate and connected to each other to form 3D graphene architectures [69].

2.4 3D Graphene structures

In order to enhance the functionalities and performance of the graphene-based materials in different application areas, tremendous efforts have been devoted to develop new 3D graphene-based architectures with different morphologies. In this section, a review of the most typical structures, along with their characteristics have been discussed in details.

2.4.1 Spheres

Graphene-based spheres, thanks to their promising properties like high electrical conductivity and large surface area, are one of the most reported 3D graphene architectures. Template-assisted method and assembly approach are the main techniques for the fabrication of graphene-based spheres [55], [70], [71]. Typically, spherical templates like SiO_2 and PS are used to convert 2D graphene sheets to 3D graphene spheres. For example, hollow graphene/polyaniline (PANI) hybrid spheres were fabricated *via* layer-by-layer assembly of negatively charged GO sheets and positively charged PANI on the surface of sulfonated PS spheres followed by the removal of the template (Figure 2.9a) [71]. Recently, graphene nanoballs with crumpled structure were fabricated through using an aerosol-assisted capillary compression method shown in Figure 2.9b-c. To this aim, GO aqueous solution containing various metals or metal oxides (e.g. Pt and SnO_2), were sprayed into a tube furnace carrying nitrogen gas at a temperature of 800 ˚C which led to a rapid evaporation of solvent and thus compression and aggregation of GO sheets and formation of crumpled 3D graphene balls [72]. In another novel approach, hollow and filled graphene-based spheres was fabricated through one-step core-shell electrospraying technique without applying any post treatment or using any template (Figure 2.9d-e) [8]. Using precursor-assisted CVD technique, Lee *et al.* synthesized mesoporous graphene nanoballs in which, iron chloride and PS balls were used as the catalyst precursor and carbon source, respectively. The obtained graphene nanoballs which are given in Figure 2.9f, showed a large specific surface area of 508 m^2/g. Figure 2.9g illustrates the schematic representation of produced mesoporous nanoballs, where PS balls were first functionalized with carboxylic acid and sulfonic acid groups in order to enhance the

dispersion of PS balls in $FeCl_3$ solution and then annealed at 1000 °C under hydrogen atmosphere. During the process, the adsorbed iron ions on the surface of PS were reduced to ion metals and thus it acted as 3D domains and catalyst for the growth of graphene through CVD method [73].

2.4.2 Networks

Three-dimensional graphene networks, including graphene foams [74], [75], hydrogels [76], [77], aerogels [78], [79] , and sponges [80], [81], are the most reported 3D graphene architectures. CVD technique is the main method for the production of high quality 3D graphene networks where few layers of graphene are deposited on the surface of a metal substrate through carbon dissolution and segregation mechanism. Figure 2.10a-d represent the CVD grown-graphene networks before and after etching the template [82]. Obtained 3D graphene networks contains less defects than chemically derived graphene which can be also approved by Raman characterization technique [62], [82]. Since D-band ($\sim$1350 cm^{-1}), a characteristic peak in the Raman spectra of graphene, is related to disorderness and its intensity changes with the defects in the structure [83], thus disappearance of D band of CVD growth graphene network in the Raman spectra confirms the formation of defect-free graphene (Figure 2.10f) .
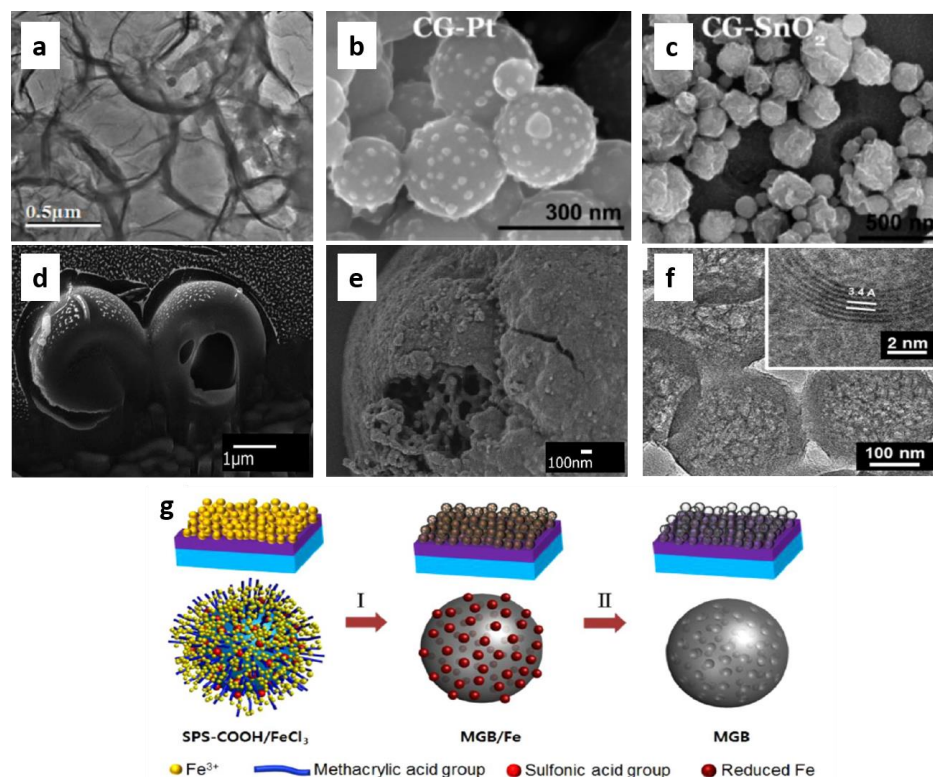
Figure 2.9 (a) TEM image of rGO/PANI hollow spheres *via* layer-by-layer assembly method [71], (b-c) SEM images of crumpled graphene balls composites synthesized by direct aerosolization of a GO suspension mixed with precursor ions: graphene balls composited with SnO_2 (a) and Pt (b) [72], (d) FIB-SEM image of core-shell electrosprayed hollow graphene-based PMMA spheres, (e) SEM image of core-shell electrosprayed filled graphene-based PS spheres [8], (f) High-resolution TEM image of mesoporous graphene nanoballs obtained by CVD, and (g) The fabrication process of mesoporous graphene nanoballs [73]

Despite their high quality, CVD growth graphene networks suffer from large pore sizes (e.g. hundreds of micrometers) , high porosity (e.g. ~99.7%) and thus low yield [62]. To address this problem, many studies have been focused on the using of different templates. In one of the works, Lee et al. [84] reported the fabrication of high-density 3D graphene networks by using nickel chloride hexahydrate as catalyst precursor by annealing it at 600 ˚C. After annealing, 3D graphene foam were grown at the different temperatures on the cross-linked nickel skeleton in the presence of hydrogen and argon atmosphere. Figure 2.11a-b show the difference between CVD growth 3D graphene networks with commercial nickel foam and cross-linked nickel skeleton. The pore size of

3D graphene networks grown from commercial nickel template was 1-2 orders of magnitude greater than the one grown with cross-linked nickel template. Consequently, the smaller pore size of annealed template led to the relatively higher density of 3D graphene networks ranging from 22 to 100 mg/cm^3, compared with that of the nickel foam (1 mg/cm^3).

The effect of growth temperature on the structure of 3D graphene networks was investigated by Raman spectroscopy (Figure 2.12a-b). Lee *et al.* [84] demonstrated that the quality of 3D graphene networks was improved by increasing the growth temperature up to 1000 °C since defects in the structure decreased and thinner graphene layers were formed as D-band (~1340 cm^{-1}) disappeared and the intensity of 2D-band (~2750 cm^{-1}) increased, respectively (Figure 2.12a). In the Raman spectra of graphene, the intensity ratio of 2D-band to G-band (~1575 cm^{-1}) together with the 2D-band full-width at half maximum estimate the number of graphene layers (Figure 2.12b) [83]. The existence of monolayer, bilayer and multilayer graphene at the same time in the structure was attributed to the various size of cross-linked nickel grains in the template (Figure 2.12 f-k).

In addition to CVD, 3D graphene networks could be synthesized through different approaches such as assembly methods [50], [85] and templated-assisted technique [86].
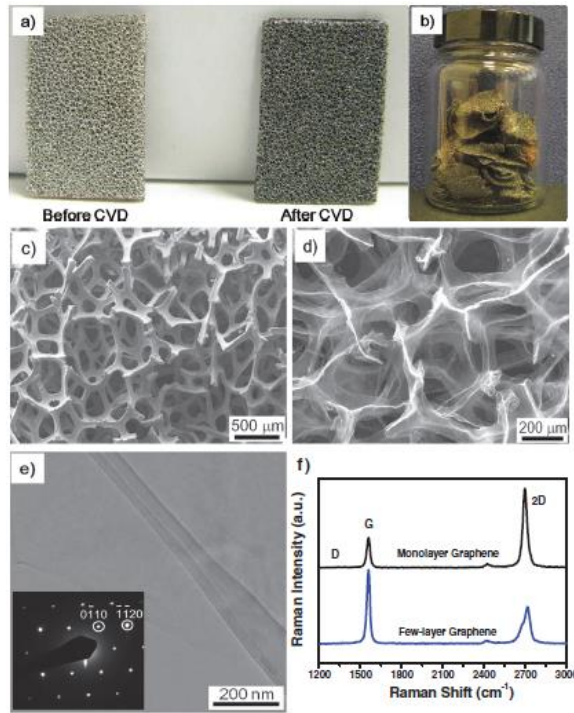
Figure 2.10 Photographs of (a) Ni foam before and after the growth of graphene, and (b) graphene networks obtained in a single CVD process. SEM images of (c) 3D graphene networks grown on Ni foam after CVD, and (d) 3D graphene networks after removal of Ni foam. (e) TEM image of a graphene sheet. (f) Raman spectra of 3D graphene networks [82].
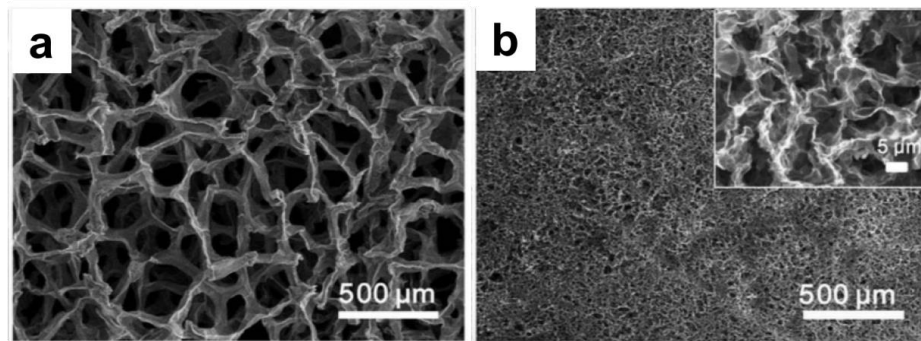
Figure 2.11. Comparison of 3D graphene networks obtained by using two different templates of (a) commercial nickel foam, and (b) cross-linked nickel skeleton [84].
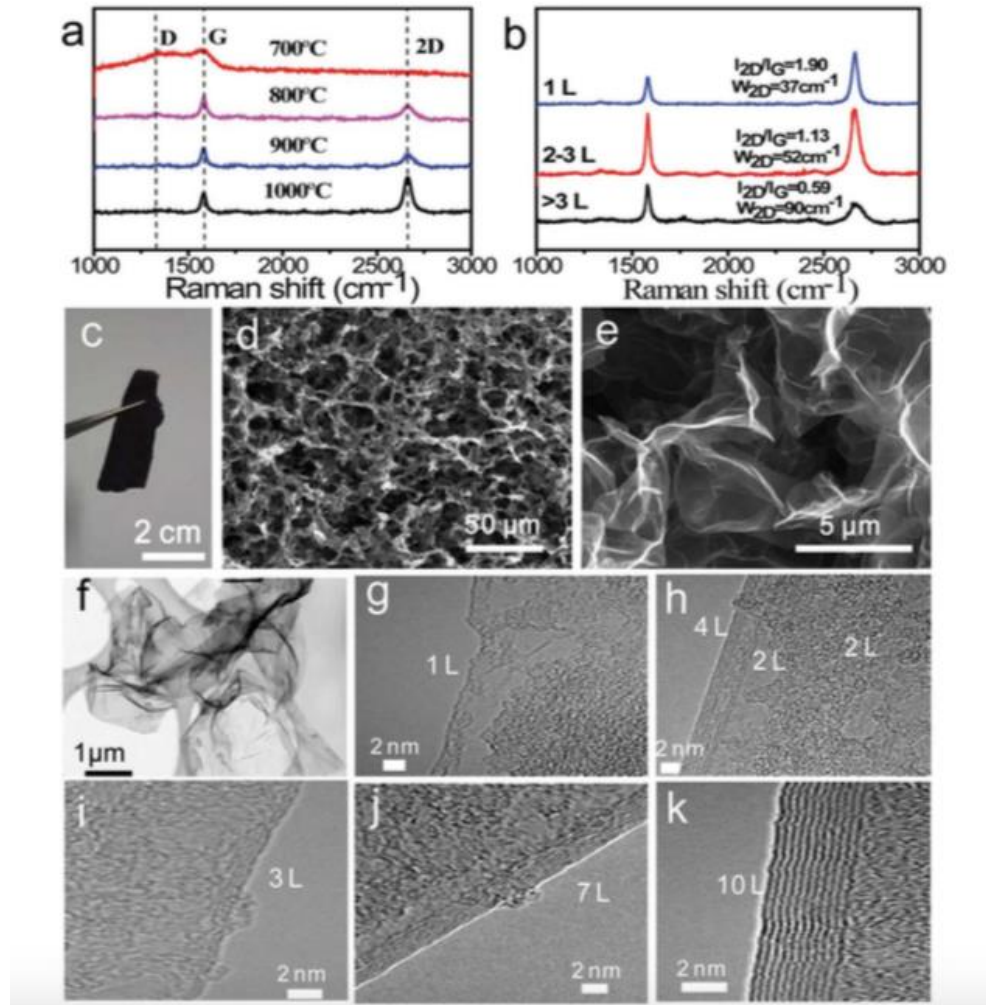
Figure 2.12 (a) Typical Raman spectra of 3D graphene network grown with different temperatures (b) Typical Raman spectra of a 3D graphene network. (c) A photograph of the free-standing 3D graphene network. (d, e) SEM images of honeycomb-like graphene layers after etching nickel template with $FeCl_3$/HCl solution at different magnifications. (f) Low-resolution TEM image of the graphene layers in 3D graphene network. (g–k) High resolution TEM images of different graphene layers in 3D graphene network [84].

2.4.3 Films

In the past few years many efforts have been devoted on the fabrication of 3D graphene films since it possesses large surface area, interconnected framework and good mechanical strength which make it an ideal candidate for many applications specially energy related areas. However, π- π interactions and van der Waals forces between 2D graphene sheets cause a significant loss in the surface area and thus limits the usage of

graphene films in practical applications [40], [87]. For understanding the behavior of graphene sheets in bulky structure, one can consider graphite as a packed case of graphene, although it lacks many of the superior characteristics of single sheet graphene as a consequence of dense packing [88]. To address this problem, further consideration such as addition of spacer materials is essential to inhibit intersheet restacking of sheets. Up to now, the incorporation of spacer materials such as polymers [89], noble metals [90], metal oxides and hydroxides [91], [92], carbon materials [93], and metal organic frameworks [94] in between the 2D graphene sheets have been reported. In addition to the above-mentioned materials, different templates (e.g. PS, PMMA and SiO_2 spherical particles) could be used to prevent the agglomeration problem of graphene sheets. Choi *et al.* [95] prepared MnO_2 deposited 3D macroporous graphene frameworks by using PS spherical particles as template following by the filtration and removal of the template (Figure 2.13). The proposed material exhibited high electrical conductivity and surface area, which makes it a great potential as electrode material for supercapacitors.

In another study, Yang *et al.* [88] by inspiration from nature demonstrated that the water molecules can act as a natural spacer for enlarging the space in-between the graphene sheets and inhibits the agglomeration. Therefore, the resultant graphene film could act as a high performance electrode material since water molecules provided a porous structure, allowing the electrolyte ions to access the inner surface area of each sheet individually. Interestingly, although the obtained film contained almost 92 wt% water, it showed a high electrical conductivity which might stem from face-to-face-stacked morphology of the wet film and provided electron transport paths in the structure.

At the same time, some different methods like tape casting [96], leavening [97], light scribing [98], and chemical activation [99] have been developed for the fabrication of porous graphene films without using spacer materials.
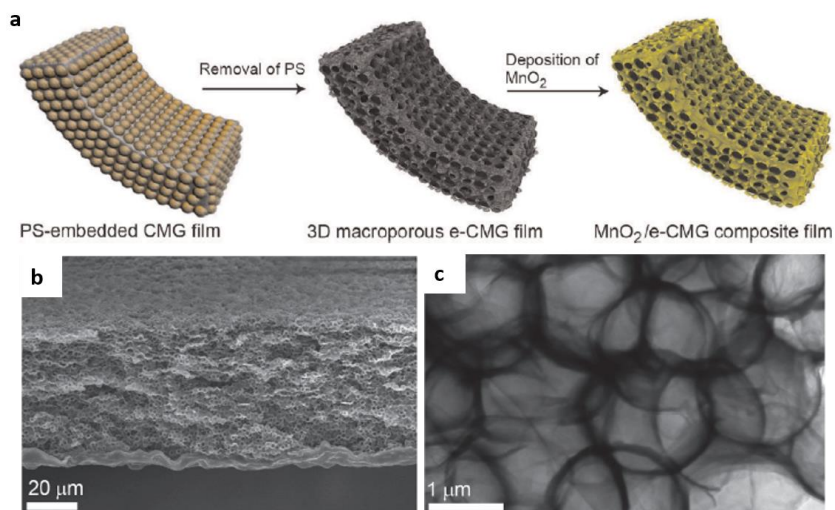
Figure 2.13 (a) Schematic illustration of the fabrication procedure of 3D macroporous MnO$_2$-chemically modified graphene films, (b) SEM and (c) TEM images of the chemically modified graphene films [95].

2.4.4 Other novel architectures

In addition to the aforementioned 3D graphene architectures, the fabrication of different structures like 3D graphene scrolls [100], tubes [101], and honeycombs [102] have also been reported. Figure 2.14 represented some of 3D graphene structures, which are reported in the literature. In a work reported by Zhang et *al.* [100], nitrogen-doped graphene ribbon assembled core-sheath MnO@graphene scrolls was fabricated by a combination of hydrothermally assisted self-assembly and an N-doping strategy (Figure 2.14 a-b). The obtained 3D architecture could serve as a high performance electrode in lithium storage devices.

In another study, 3D graphene microtubings were prepared through hydrothermal method and Cu wires as template. The morphology of graphene-based tubes is similar to that of CNTs although the inner diameter of tubes is much larger when compared to CNT. In this work, Cu wires were placed inside a glass pipeline and then GO dispersion was filled in the pipeline. During hydrothermal reduction, GO sheets were wrapped around the Cu wires and 3D graphene microtubings were obtained by removing the template and pipeline (Figure 2.14c-d) [101].

23

Honeycomb-like 3D graphene architecture was fabricated by a simple reaction of lithium oxide and carbon monoxide gas under low pressure at 550 °C, which is shown in Figure 2.14e-f. The obtained structure exhibited a high energy conversion efficiency which makes it a promising material in the energy storage devices [103].

Figure 2.14 (a) Schematic representation of the fabrication process for the 3D hierarchical MnO@N-doped graphene scrolls/graphene ribbons architecture (b) FESEM images of MnO@N-doped graphene scrolls/graphene ribbons at different magnifications [100]. (c) SEM image of a helical graphene microtubings made by using a twist of two Cu wires. (d) SEM image of the multichannel graphene microtubings with a channel number of 4 [101]. (e) High-angle annular dark field image and (f) TEM image of a honeycomb-structured graphene [103].

2.5 Applications of 3D graphene architectures

As discussed above, 3D graphene structures with improved performance and advanced functionalities compared to 2D graphene sheets have been widely used in many applications such as energy storage devices, sensors, polymeric composites, catalysis, etc.

2.5.1 Supercapacitors

Supercapacitors have drawn significant attention compared to other energy-storage devices owing to their advanced properties like high power density, long cycle life [104]. Based on energy storing mechanisms, supercapacitors divide into pseudo-capacitors and electrochemical double layer capacitors (EDLCs). Pseudo-capacitors like transition metal oxides and conducting polymers store the charges *via* chemical redox-reaction on the surface, whereas EDLCs (e.g. carbon-based materials) store the energy by ion adsorption on the electrode-electrolyte surface. Among various carbon-based materials, graphene as an EDLC electrode is widely used in the electrochemical energy storage systems owing to its rich variety of dimensionality and large surface area [105]. Very recently, 3D graphene structures became an attractive candidate for supercapacitors thanks to their porous structure, high surface area and interconnected network which improves the accessibility of electrolyte ions to the surface of electrode and increases the electrical conductivity [106]. So far, different structures of 3D graphene-based materials like spheres [52], networks [82], and films [107] have been reported as potential electrodes for supercapacitors. In following, the supercapacitor applications of the reported graphene structures and their related composites have been discussed in details.

Graphene spheres with hollow micro/nanostructures offer advanced characteristics such as high surface area and shortened diffusion length for charge and mass transport which can greatly enhance the performance as electrode for supercapacitor [108]. For instance, graphene-wrapped polyaniline hollow spheres were fabricated by deposition of PANI polymer on the sulfonated PS spherical templates followed by the removal of template to obtain hollow PANI spheres. Then negatively charged GO sheets were wrapped on the positively charged PANI hollow spheres *via* electrostatic interaction and then were reduced to graphene through electrochemical reduction (Figure 2.15a-b). Obtained graphene-wrapped polyaniline hollow spheres exhibited an excellent specific capacitance of 614 F/g at a current density of 1 A/g and over 90% retention of the capacitance after 500 charging-discharging cycles (Figure 2.15c-d) [109]. In another work reported by Lee *et al.* [73], mesoporous graphene nanoballs as electrode for

supercapacitors were prepared by using CVD method and showed high specific capacitance of 206 F/g at a scan rate of 5 mV/s. After 10000 cycles of charging-discharging even at high current density, mesoporous graphene nanoballs still exhibited 96% retention of capacitance.

Three-dimensional graphene networks like graphene foam, sponges, and hydrogels have attracted great attention due to their desired porous structure which enhances the movement of electrolyte ions inside the graphene frameworks and thus increases the electrical conductivity and electrochemical performance of the electrode materials [48]. Sponge-like graphene nano architectures fabricated by microwave synthesis of graphene and CNT, exhibited a high energy density of 7.1 W·h/kg at an extra high power density of 48000 W/kg and retention of 98% after 10000 cycles of charging-discharging in 1M sulfuric acid as electrolyte. The high performance of the obtained structure may attributed to the large surface area of 418 m^2/g and fully accessible porous network [80].

Up to now, considerable efforts have been dedicated for the fabrication of flexible supercapacitors as the potential power supplies for future wearable and portable devices like electronic textiles [110]. Concerning this, Xu *et al.* [111] produced a flexible solid-state supercapacitor from graphene hydrogel film as electrode and polyvinyl alcohol and sulfuric acid as electrolyte. The obtained electrode with a thickness of 120 μm showed a high gravimetric capacitance of 186 F/g at a current density of 1 A/g and excellent cycling capability of 91.6% retention after 10000 charge/discharge cycles (Figure 2.15f-g). Besides, 3D graphene hydrogel films with interconnected networks presented high electrical and mechanical robustness, which is essential for the flexible supercapacitor applications. Recently, He *et al*. [112] presented an ultralight and freestanding flexible supercapacitor of graphene/MnO_2 composite networks, shown in Figure 2.15e, *via* CVD growth of graphene on the nickel foam subsequently followed by electrochemical deposition of MnO_2 on the 3D graphene network. A high specific capacitance of 130 F/g at a scan rate of 2 mV/s and a low resistance variations upon bending up to 180° was achieved which confirms the excellent electrochemical performance of the obtained 3D graphene networks.

2.5.2 Lithium-ion batteries

In the recent years, 3D graphene structures have been extensively studied for their potential use as active electrodes in batteries. The integration of 3D graphene into the structure of electrodes improves the lifetime and energy density as well as the electrochemical performance of the electrodes since the batteries usually suffer from low reversible capacity and cyclic life when compared to supercapacitors. Therefore, in the design of batteries (e.g. Lithium ion batteries, LIBs) one should consider the importance of the LIB components (e.g. electrodes and electrolyte) role in the improvement of the battery performance. By virtue of outstanding characteristics like high surface area, porous structure, fast mass/charge transfer, and interconnected network, 3D graphene architectures became an outstanding candidate for high performance LIBs.
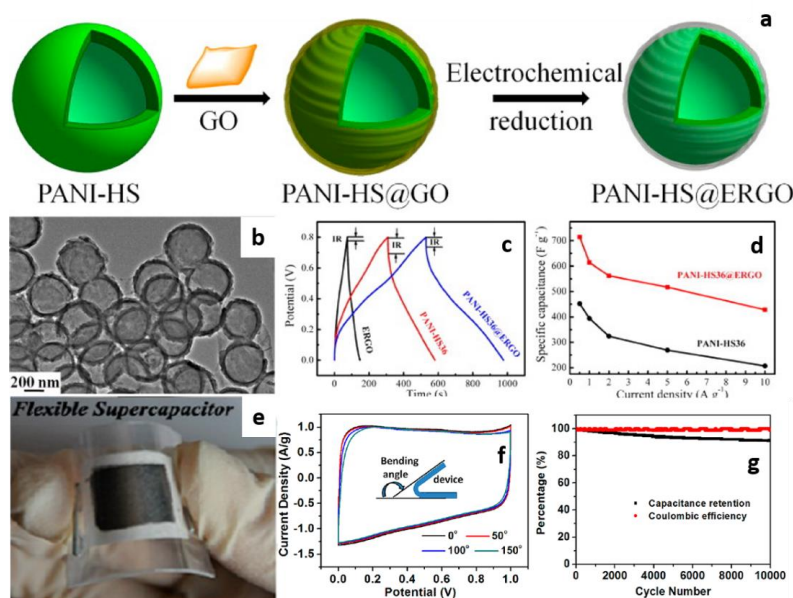
Figure 2.15 (a) Schematic illustration of the preparation steps, and (b) TEM image of graphene wrapped hollow PANI spheres. (c) Galvanostatic charge−discharge curves of electrochemically redued GO, PANI hollow spheres, and graphene wrapped PANI holow spheres (d) Plots of specific capacitance for PANI hollow spheres and graphene wrapped PANI hollow spheres at various current densities [109]. (e) Digital photograph of 3D graphene/MnO₂ composite networks [112]. (f) CV curves of the flexible solid-state supercapacitor based on the 3D graphene hydrogels at 10 mV/s for different bending angles. (g) cycling stability of the flexible solid-state supercapacitor based on the 3D graphene hydrogels at a current density of 10 A/g [111].

So far the incorporation of various metal or metal oxides (e.g. Sn [113], NiO [114], Fe_3O_4 [115], $LiFePO_4$ [116]), and CNT [117] with graphene sheets and fabrication of 3D graphene composites have been studied. Yu and co-workers [118] developed a mesoporous TiO_2 spheres embedded in 3D graphene networks by a facile hydrothermal self-assembly strategy. The as prepared composite as a negative-electrode for LIBs exhibited an excellent high-rate capacitance of 124 mA.h/g at a current rate of 20 C when compared to that of pure TiO_2 as 38 mA.h/g (Figure 2.16a-b). Such an improvement in the electrochemical performance of the as prepared composite may attributed to the high contact area between the electrolyte and electrode, desired diffusion kinetics for both electrons and lithium ions and high electrical conductivity of the 3D graphene networks as well as porous structure of TiO_2 spheres.

Using microwave-assisted synthesis of self-assembled 3D graphene/CNT/Ni, Bae *et al.* [117] developed a new electrode for LIBs in which CNTs were grown on graphene sheets through tip growth mechanism by Ni nanoparticles and acted as spacer by preventing the re-stacking of 2D graphene sheets. The synthesized 3D composite as anode electrode for LIBs showed a reversible specific capacity of 648.2 mA.h/g after 50 cycles at a current density of 100 mA/g.

Due to its high theoretical capacity, low cost, and nontoxic properties, Fe_3O_4 has been considered as a promising electrode for LIBs. However, high volume expansion and the low conductivity of Fe_3O_4 prohibit stable performance of electrodes. Integration of conductive nanomaterials like graphene and construct 3D architectures is one the main strategies to improve the performance of Fe_3O_4 based electrodes. To this aim, Luo *et al.* [115] prepared 3D graphene foam supported Fe_3O_4 LIB which exhibited a high capacity of 785 mA.h/g at 1C charge-discharge rate without decay up to 500 cycles. The electrochemical properties of the graphene supported Fe_3O_4 LIB electrodes are given in Figure 2.16c-d.

In all of the above-mentioned studies, 3D graphene provides short path length for Li ion as well as electron transport, increases the conductivity by eliminating the agglomeration, and thus improves the electrode performance.

2.5.3 Sensors

In recent years, graphene-based materials decorated with metals and metal oxides have been studied in the various sensing devices (e.g. electorchemical sensing and bio-sensing) due to graphene's excellent optoelectronic properties as well as high catalytic activity of the metals/metal oxides [119]. For example, Yavari *et al.* [120] prepared a 3D graphene network for the detection of NH_3 and NO_2 at room temperature and atmospheric pressure with a high sensitivity of gas detection in the ppm range. In another study, Kung *et al.* [121] designed a platinum-ruthenium bimetallic nanocatalysts integrated 3D graphene foam as a sensor for the detection of hydrogen peroxide by enhancing the surface area and improving the effective transport in the reaction. The proposed material exhibited a high performance toward electrochemical oxidation of H_2O_2 with a high sensitivity of 1023.1 mA/mM.cm^2 and low detection limit of 0.04 mM.

Large-area 3D graphene interconnected GO intercalated by PANI nanofibers for the determination of guanine and adenine have been constructed by Yang *et al.* [122]. By the help of strong π-π interactions and electrostatic adsorption, positively charged guanine and adenine adsorbed to the negatively charged proposed structure. High sensitivity, long-term stability, and low detection limit of the prepared material makes it a reliable approach for the determination of other small molecules.
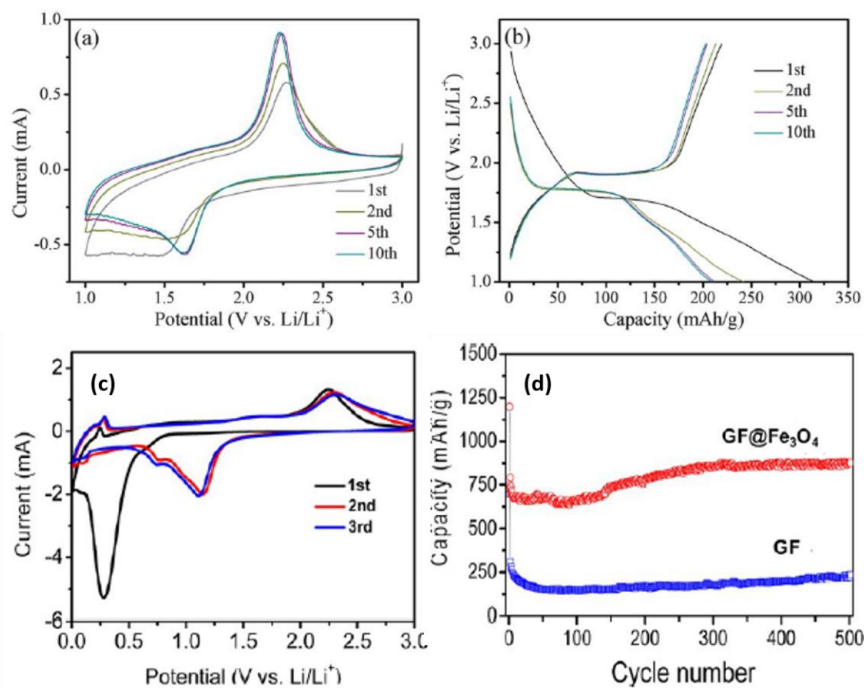
Figure 2.16 (a) Representative cyclic voltammograms of the TiO_2 spheres embedded in 3D graphene networks at a scan rate of 1 mV/s. (b) charge–discharge voltage profiles of the TiO_2 spheres embedded in 3D graphene composite at a current rate of 0.5 C [118]. (c) CV curves of the graphene foam supported Fe_3O_4 electrode. (d) Cycling profiles of the graphene foam and graphene foam supported Fe_3O_4 electrodes [115].

2.5.4 Fuel cells

Nowadays, the finite nature of fossil fuels and rapid increase in energy consumption persuade the scientists to design and develop renewable energy sources. To this aim, 3D graphene architectures have attracted great attention in the fuel cells as catalysts or catalyst carrier supporting metals and alloys in oxidation and oxygen reduction reactions (ORR) and thus improve the performance of the fuel cell [48]. Microbial fuel cells (MFCs) convert the chemical energy in biodegradable organic materials into electricity *via* bio-oxidation process and thus provide environmental bioremediation. However, most of the commercially available MFCs suffer from low power density and low bacteria loading on the surface of the electrodes. To address this problem, many studies have focused on the integration of catalysts materials to the both anode and cathode of the MFCs [123], [124]. Very recently, the use of 3D graphene as catalysts or support material has gained great

attention because of the large surface area and high electrical conductivity of 3D graphene structures. In one of the studies, Yong *et al.* [124] suggested a macroporous and monolithic anode electrode based on PANI hybridized 3D graphene. Owing to large surface area of graphene, the ability of integration with bacterial films have improved and thus more electrons passed through multiplexing and conductive pathways. The schematic illustration of the interface and interactions between 3D graphene/PANI electrode and bacteria is shown in Figure 2.17a. As shown in Figure 2.17b-c, obtained MFC exhibited a high power density of 768 mW/m^2, which is 4 times higher than that of the carbon cloth MFC under the same conditions. Similarly, 3D graphene aerogel decorated with Pt nanoparticles have been fabricated as a freestanding anode for MFCs with an excellent power density of 1460 mW/m^2. The superior performance of prepared MFC was attributed to the high bacteria loading capacity, easy electron transfer between the bacteria and the 3D graphene/Pt, as well as fast ion diffusion in 3D pores [125].
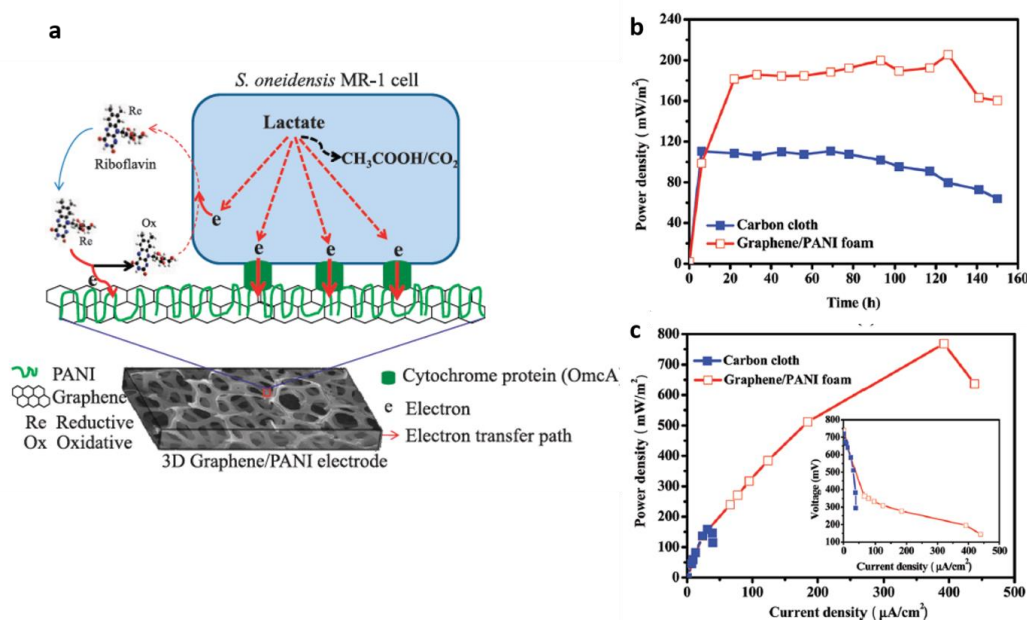
Figure 2.17 (a) Schematic illustration of the interface between 3D graphene/PANI monolith electrode and *S. oneidensis* MR-1 bacteria. (b) Time courses of the power density output of the MFCs equipped with a carbon cloth anode or a graphene/PANI foam anode. (c) Polarization curves of the two types of MFCs. The inset shows the I-V relation [124].

2.6 Conclusions and perspectives

This review summarized the recent developments in 3D graphene-based materials with different morphologies along with their properties and applications. So far, considerable efforts have been devoted to the design and fabrication of 3D graphene materials with different morphologies like spheres, films, and networks. Three-dimensional graphene not only preserve the intrinsic properties of 2D graphene by inhibiting the re-stacking and aggregation of sheets, but also provide advanced functionalities with desired characteristics in the various applications like supercapacitors, fuel cells, batteries, sensors, etc. The main approaches for the construction of 3D graphene architectures are assembly method, template-assisted techniques, chemical vapor deposition and electrospraying technology. Nevertheless, there are still some challenges in the production of the 3D graphene architectures. For instance, the size of constructed structures and their properties strongly depend on the building blocks (e.g. templates). Besides, the main problem of the graphene sheets is their tendency to agglomerate which strongly decreases the electrical conductivity and utilization of graphene in bulk application. Therefore, there is a need to design new and feasible approaches that can prevent the re-stacking of graphene layers and fabricate an ideal 3D graphene structure. Finally, low-cost as well as mass production of 3D graphene materials are critical issues for the practical applications. Taking these into account, 3D graphene architectures could provide a new platform to offer advanced functionalities in various applications in the near future.

CHAPTER 3 DESIGN AND FABRICATION OF HOLLOW AND FILLED GRAPHENE-BASED POLYMERIC SPHERES VIA CORE-SHELL ELECTROSPRAYING

3.1 Introduction

Graphene with a 2D honeycomb-like structure of carbon atoms has been used in many applications including microchips, sensors, energy storage devices, and composites due to its unique mechanical, thermal and electronic properties[126]. There are two main approaches in the synthesis of 2D graphene; bottom-up approach consisting of epitaxial growth on silicon carbide and chemical vapor deposition (CVD) method, and top-down approach including micromechanical cleavage, electrochemical exfoliation and chemical exfoliation of graphite. The advantage of using bottom-up approach is controlling the morphology and structure of the produced graphene sheets [127], whereas top-down methods have some drawbacks of preserving 2D structure of graphene and limitations in the utilization of graphene in polymer matrix and transferring graphene sheets on different templates [128]. Graphene sheets have tendency to agglomerate in matrix and form crumpled structure which causes a significant decrease in the surface area, electrical and other characteristic properties [48]. To overcome this problem, several studies have focused on the development of 3D graphene materials with different structures and morphologies such as graphene fibers [7], [129], graphene tubes [101], graphene balls [130] and, graphene networks [95], [131]. CVD technique is one of the widely used bottom-up approaches for the production of 3D graphene networks, 3D porous graphene films and macroporous structures over templates such as conductive substrates and 3D metal substrates (e.g. nickel foam) by using different carbon sources at different conditions [62], [132], [133]. It is also possible to convert 2D graphene sheets into 3D structures by wet chemistry methods like water-in-oil emulsion technique without using any surfactant [134] and hydrothermal process by mixing graphene oxide (GO) with carbon nanotubes and metal oxides to improve surface area, electrical conductivity and capacitance properties of 3D graphene structures [135], [136]. In the recent works, thermoelectric properties of graphene based nanocomposites have been improved by constructing 3D interconnected structures consisting different conducting polymers and reduced graphene

oxide (rGO) by in situ polymerization techniques [137]–[139]. Especially in flexible energy storage devices, graphene based fibers and 3D porous graphene polymer networks are fabricated as an electrode material in supercapacitors to enhance specific capacitance and provide long-term cyclic stability [140], [141].

For the production of hollow 3D graphene structures, sphere-like templates such as polystyrene (PS), silicon dioxide (SiO_2), and titanium dioxide (TiO_2) were used in several published techniques. In one of the works, graphene hollow spheres were prepared by covering PS balls with graphene oxide (GO) sheets and then calcination was applied at 420°C for 2h to remove PS from the core [54]. In another work, graphene-based hollow spheres were fabricated by electrostatic assembly of GO sheets on polyethylenimine covered SiO_2 spheres in solution phase, and subsequently followed by washing with hydrofluoric acid and annealing processes to get hollow structure [142]. In order to improve the catalytic properties of hollow spheres, Pd nanoparticles were decorated in double-shelled hollow carbon spheres by using SiO_2 nanospheres as template during in situ process [143]. In the mentioned processes, the size of spheres directly depends on the templates. It is not an easy process to control the shape of spheres and hollowness and get higher yield of graphene balls due to the recovery process in wet-chemical methods.

Electrospinning is one of widely used techniques to produce fibers and spherical or bead-like structures with the diameters ranging from few micrometers to nanometer by adjusting the surface tension of the droplet and viscosity of the solution under electric field [144]. Recently, co-axial electrospinning process has received great attention due to its ability to produce core-shell 3D structures with different functionalities which have distinct advantages in comparison to structures fabricated by regular electrospinning technique [145]. In this technique, two dissimilar solutions in concentric tubes flow under a high electric field, which is applied between the tip of the nozzle and collector. As a result, the surface tension of a compound droplet at the tip of the nozzle is overcome whereby the droplet stretches and forms a continuous jet which is collected on the electrically grounded plate as a fiber [146]. In electrospinning and electrospraying, the final morphology of the product is affected by solution properties (such as viscosity and electrical conductivity) and process parameters (such as voltage, flow rate, and distance

between collector and nozzle). There are few attempts for the integration of graphene into the fiber structure by using classic and co-axial electrospinning techniques. In one of the studies, Promphet *et al.* [60] fabricated graphene based nanoporous fibers by electrospinning of graphene/polyaniline/polystyrene mixture to be used as an electrochemical sensor to detect heavy metals. In another work, aligned poly(3-hexylthiophene)–graphene nanofibers produced via two-fluid coaxial electrospinning technique were integrated into high-performance field effect transistors since graphene acts as an electronically conducting bridge between the polymer domains in the structure [147]. Shilpa *et al.* [148] synthesized core-shell composite nanofibers as an anode electrode for Li-ion batteries by co-axial electrospinning of rGO-polyacrylonitrile (PAN) solution as shell and zinc oxide with polymethyl methacrylate (PMMA) as core and then applied carbonization and calcination processes to this fiber mat. In all above mentioned relevant studies, for preserving the intrinsic properties of graphene materials in the bulk matrix, GO and rGO are incorporated into the fiber structure by electrospinning technique in one-step process.

One can conclude from literature that so far, considerable amount of works have focused on the production of polymeric bead structures and core-shell microcapsules and the investigation of their morphological changes by tailoring electrospinning parameters [149], [150]. In the present work, thermally exfoliated graphene oxide (TEGO) sheets are converted into 3D spheres with controlled hollowness and porosity by using three different carrier polymers through core-shell electrospraying technique. The effect of electric field on the exfoliation of graphene sheets is investigated by spectroscopic techniques to understand graphene dispersion behavior in polymeric shell during electrospraying process. In this study, shell polymers namely PS and PMMA are chosen due to their ease for the formation of spherical topology during electrospinning process since these two polymers are widely used as a template material for the production of 3D structures. Additionally, PAN polymer is used to form carbon network because of its high carbonization degree. The appropriate concentration for the production of spheres is verified by using Mark-Houwink-Sakurada equation. Hollowness of these spheres is controlled by changing core solvent and its flow rate. The dimension and morphology of

35

graphene based spheres are investigated and optimized by tailoring the parameters of polymer type, polymer concentration, solution viscosity, TEGO amount, solvent evaporation rate and flow rate.

3.2 Experimental

3.2.1 Materials

The following materials were used in the experiments: TEGO-grade 2 (Thermally exfoliated graphene oxide purchased from NANOGRAFEN Co., average number of graphene layers: 27 calculated from X-ray diffraction data, 4% oxygen content obtained from X-ray photoelectron spectroscopy), N, N-dimethyl formamide (DMF, Sigma Aldrich, 99%), and methanol (Sigma Aldrich, 99.7%). Polystyrene (PS), Polymethyl Methacrylate (PMMA) and Polyacrylonitrile (PAN) were synthesized through free radical polymerization method. A detailed synthesis procedure of PS and PMMA polymers and their characterization results were reported in our previous publication [57].

3.2.2 Preparation of electrospraying solutions

TEGO-based polymeric solutions were prepared as shell materials. PS and PMMA solutions were prepared with a concentration of 20 wt% in DMF solvent. DMF is considered as one of the most widely used polar solvents for electrospinning technique for to provide good and stable dispersion of graphene sheets and PAN in electrospun solution. For PAN polymer, 5 wt% and 3.5 wt% were selected as polymer concentration due to its high viscosity. TEGO was dispersed in DMF at different TEGO:DMF weight ratios of 0.005, 0.01, 0.02, and 0.05 % by probe sonicator (Qsonica, Q700) for 20 minutes with 5 seconds pulse on and 3 seconds pulse off time in ice bath to get homogeneous dispersions in solutions. Then, polymers were added into TEGO dispersed DMF solution and the mixtures were stirred at room temperature for 1 day to improve the stabilization of polymer chains. The chemical structures of synthesized polymers are given in Appendix A1.

3.2.3 Production of TEGO based 3D hollow and filled polymeric spheres by core-shell electrospraying

Core-shell electrospraying process was performed by following two different procedures. In the former one, the core was kept empty during spraying process and atmospheric air was used as a core material. In the latter one, methanol was used as a core solvent to study the effect of methanol on the hollowness and morphology of spheres. Three different polymeric solutions with different TEGO contents were used as shell materials. Figure 3.1 shows schematic representation of graphene based sphere fabrication by tri-axial core-shell electrospraying technique. The size of spheres was controlled by solution parameters (type of polymer, viscosity, surface tension, concentration, and evaporation rate of solvent) and system parameters (voltage, distance between collector and syringe, flow rate) through electrospraying process. Electrospraying is performed at ambient conditions by using tri-axial electrospinning equipment purchased from Yflow Company. At the initial step, the different distances between nozzle to collector were examined and the optimized distance of 10 cm was set in all of the experiments owing to homogeneous and continuous spraying process at this distance. The applied voltage was in the range of 10–20 kV. The flow rates of shell solutions varied between 10-20 µL/min. Methanol as a core solvent was sprayed with a flow rate in the range of 0.5-2 µL/min. Electrospraying parameters of the produced spheres are given in details in Appendix A2.
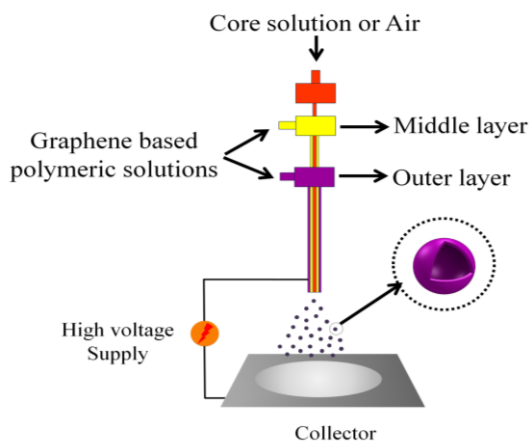
Figure 3.1 Schematic representation of fabrication of graphene based spheres by tri-axial electrospraying technique.

3.2.4 Carbonization process of produced spheres

Carbonization of TEGO based PAN spheres was completed in two steps. Firstly, spheres were stabilized by an oxidation process by heating up to 300°C under air, and then carbonization step was followed by increasing the temperature up to 1000°C under argon atmosphere. Stabilization process changes the chemical structure of spheres and the produced spheres become thermally stable at higher temperature without transition to melting phase [151].

3.2.5 Characterization

Molecular weights and polydispersity index of polymers are measured in DMF as an eluent by using Gel Permeation Chromatography (GPC) and the concentrations of polymers in column are converted to the intrinsic viscosity. The morphology and inside structure of spheres were analyzed by Leo Supra 35VP Field Emission Scanning Electron Microscope (SEM) and JEOL JIB 4601F Focused Ion Beam (FIB/SEM dual beam platform). Elemental analysis of spheres was conducted by using Energy-Dispersive X-Ray (EDX) analyzing system. X-ray diffraction (XRD) measurements were carried out by using a Bruker AXS advance powder diffractometer with a CuKα radiation source. Raman spectroscopy was used to identify the surface characteristics of samples by using a Renishaw inVia Reflex Raman Microscopy System with the laser wavelength of 532 nm at room temperature in the range of 100–3500 cm^{-1}. The functional groups of spheres were determined by Netzsch Fourier Transform Infrared Spectroscopy (FTIR).

3.3 Results and discussion

3.3.1 The effect of electric field on the exfoliation process of TEGO sheets

Electrospraying process enables graphene sheets to be dispersed homogeneously in polymer solution, prevents their agglomeration under electric field and enhances the intercalation of polymer chains into graphene layers. SEM images of TEGO sheets after the sonication and electrospraying processes are given in Figure 3.2 to promote understanding the effect of electric field on the morphological changes of TEGO sheets. Untreated TEGO has worm-like structure (Figure 3.2a). After sonication in DMF, layers

38

are separated from each other, and hence, flake dimension decreases (Figure 3.2b); however, the structure still has multi-layered graphene [30]. Upon the being subjected to applied electric field, the layers become more flattened whereby more transparent sheet formation is observed (Figure 3.2c). Electric field deforms the working fluid during electrospraying which causes loosely broad graphene layers.
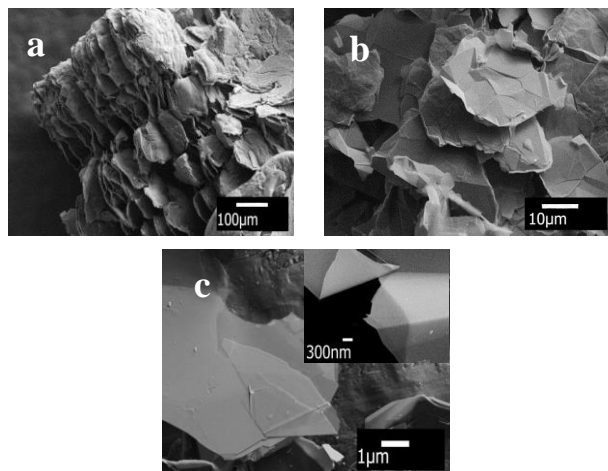
Figure 3.2 SEM images of (a) as received TEGO sheets, (b) sonicated TEGO sheets in DMF, and (c) electrosprayed TEGO sheets in DMF without polymer.

In order to detect the changes in the number of graphene layers, Raman Spectroscopy analysis was conducted for as received, sonicated and electrosprayed TEGO sheets and the results are presented in Figure 3.3. Raman spectrum of TEGO has three sharp main peaks: 1338 cm^{-1}, 1577 cm^{-1}, and 2750 cm^{-1}, refer to as D, G, and 2D peaks, respectively [83]. D peak is related to disorderness and its intensity changes with the defects in the structure. G peak corresponds to in-plane vibrations of sp^2 bonded carbon atoms and its intensity is altered due to the variation in the number of graphene layers [27], [83]. It is known from literature, as the ratio of D to G intensities (I_D/I_G) increases, sp^2 bonds are broken implying that there are more sp^3 bonds and more defects in the structure[83]. In the current study, after the sonication process, there is a slight decrease in I_D/I_G of untreated TEGO sample from 0.2 to 0.1. After eletrospraying of TEGO sheets, D band completely disappears indicating that defect-free multi-layer graphene sheets are

obtained. This decrease in D band intensity comes from the reduction in the thickness of graphene layers which is due to the deformation of solvent. In addition, shape, width and position of 2D peak determine the graphene layers [83]. The reduction in the intensity ratio of G to 2D peaks (I_G/I_{2D}) indicates the decrease in the number of graphene layers. I_G/I_{2D} values of untreated TEGO and sonicated TEGO, and electrosprayed TEGO are 2.3, 2.0 and 2.0, respectively. This shows that the sonication process breaks down graphene layers, which are bonded by weak van der Waals forces, and then initiates the exfoliation process. On the other hand, multi-layer structure is still preserved after electrospraying process because there is no notable change in I_G/I_{2D} value. Furthermore, the intensity values of 2D peak increases after each process, and 2D peak of electrosprayed TEGO gets sharper and thus number of graphene layers decreases slightly when compared to sonicated TEGO. The peak positions and intensity ratios are given in Appendix A3.
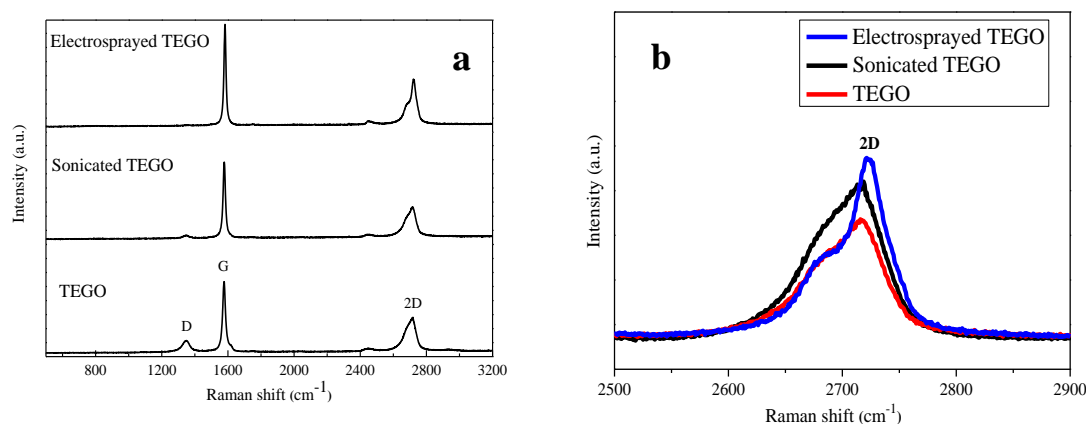
Figure 3.3 (a) Raman spectra of as received TEGO, sonicated TEGO and electrosprayed TEGO and (b) the comparison of 2D peak intensities

3.3.2 The effect of polymer type, polymer concentration and TEGO amount on the structural properties of graphene-based spheres

In the electrospraying process, the viscosity of solution is one of the important parameters, which determines the morphology of structure. The higher the viscosity is, the greater the electric field should be to be able to deform the droplet at the nozzle tip to initiate the polymeric jet formation. The viscosity of solution depends on the molecular

weight of polymer and polymer concentration. PS, PMMA, and PAN as thermoplastic polymers are chosen as shell materials in the production of polymer-based composites via core-shell electrospraying process. Weight average molecular weight (Mw), number average molecular weight (Mn), polydispersity index (PDI) and intrinsic viscosity values of the used polymers are given in Table 3.1. These polymers have similar Mw values but their intrinsic viscosity values are different and this directly affects polymer concentration and viscosity of electrospun solutions.

Table 3.1. Mw, Mn, PDI and intrinsic viscosity values of shell polymers from GPC analysis

Polymer type	Mw (g/mol)	Mn (g/mol)	PDI	Intrinsic viscosity (dL/g)
PMMA	41645	20798	2.00	0.3404
PS	49283	29686	1.66	0.0781
PAN	44489	32293	1.38	0.7261

Selected polymers can form spherical structures by the optimization of the system (applied voltage, syringe and collector distance, flow rate) and solution parameters (polymer concentration and TEGO content). In addition to these mentioned parameters, polymer chain entanglements affect the structural formations during electrospinning process. The degree of entanglement is determined by calculating two limiting concentrations, C^* and C_e. C^* corresponds to the solution concentration where the hydrodynamic volumes begin to overlap and C_e is the entanglement concentration which separates the semi-dilute unentangled and semi-dilute entangled regimes. C^* is calculated using the following equation:

$$C^* = 1/[\eta] \tag{1}$$

where $[\eta]$ is the intrinsic viscosity [149]. C_e value is approximately equal to $10C^*$ for neutral polymers in good solvent systems [152]. When polymer concentration, C, is higher

than C_e, bead free fibrous structures are produced due to the extensive chain entanglement. When $C^*<C<C_e$, bead dominant structures are generated [149]. In this study, C* values of PMMA and PS are about 29.4 mg/mL and 128.1 mg/mL, respectively and the adjusted concentrations (C) of PMMA and PS are 200 mg/mL which is in the range of $C^*<C<C_e$. In case of PAN based spheres, C* is about 13.8 mg/mL and polymer concentrations of 3.5 wt% and 5 wt% are 35 mg/mL and 50 mg/mL, respectively, and these values are between C* and C_e.

Moreover, the optimum concentration for the fabrication of polymer based TEGO spheres was investigated by using Mark-Houwink-Sakurada equation (Eq.2):

$$[\eta]=K_H M^a \tag{2}$$

where the constants "K_H" and "a" depend on the polymer type, solvent and temperature. The Mark-Houwink-Sakurada constants of PMMA, PS, and PAN are given in Appendix A4. By combining Eq.1 and Eq.2, following expressions based on C* and molecular weight is obtained for each polymer:

$$C^* = 4\times10^4 Mw^{-0.625} \qquad\qquad \text{PMMA} \tag{3}$$

$$C^* = 3.15\times10^4 Mw^{-0.603} \qquad\qquad \text{PS} \tag{4}$$

$$C^* = 5.65\times10^4 Mw^{-0.780} \qquad\qquad \text{PAN} \tag{5}$$

Figure 3.4 shows the entanglement concentration $C_e=10C^*$ as a function of molecular weight of PMMA, PS, and PAN polymers. Solid lines represent the concentration threshold of each polymer obtained from Eq.3 (black line), Eq.4 (red line) and Eq.5 (blue line), and each point corresponds to the polymer concentrations which are selected for the fabrication of spheres. As seen in Figure 3.4, all of the corresponding points attributed to the used polymer concentrations stay on the lower region of threshold line (C_e) where bead formation is dominant.
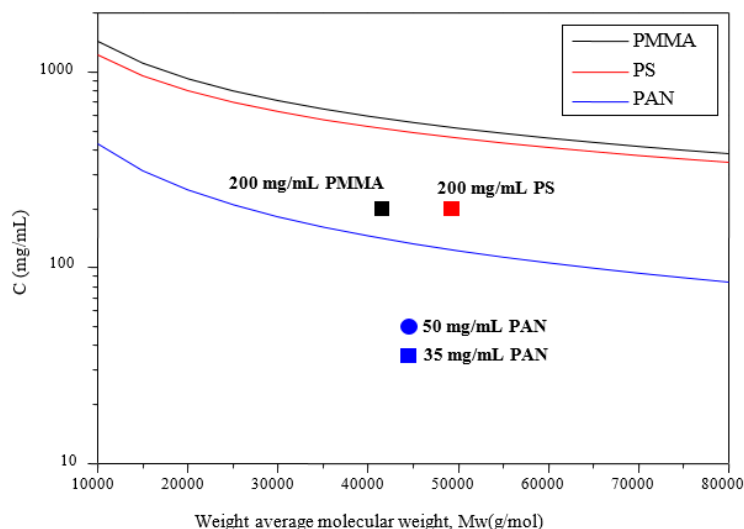
Figure 3.4 Entanglement concentration Ce=10C* as a function of the molecular weight of PMMA, PS, and PAN polymers.

Polymeric solutions were purged through outer syringe by keeping core syringe empty during co-axial electrospraying. Table 3.2 summarizes the synthesis conditions and characteristic properties of spheres made of PMMA and PS polymers and shrinkage percentages of polymeric spheres after the integration of TEGO into the structure. By the addition of TEGO in electrospun solutions, there is a significant decrease in the diameter of TEGO based spheres when compared to neat polymeric spheres. Herein, TEGO sheets start the shrinkage of the spheres under electric field since the surface forces increase on droplets. After increasing the amount of TEGO, a gradual increase is observed in sphere diameter. For instance, as seen in Table 3.2, PMMA spheres shrink by about 38% through the addition of 0.005 wt% TEGO and the shrinkage values decreases down to 29% and 20% with 0.01 wt% and 0.02 wt% TEGO loadings, respectively. The decrease in diameter shows the dense stacking of graphene layers in polymeric shell. It is known that oxygen functional groups of GO in aqueous and organic solutions are negatively charged [153], and hence, the electrostatic interaction between these negatively charged GO sheets and positively charged polymers minimizes the size of the spherical structure. Carbon/oxygen ratio of GO is changed regarding the type of chemical exfoliation process [24], [30]. Most of surface oxygen functional groups can be removed by applying thermal treatment and

hydrophilicity of GO decreases and this allows for controlling the surface chemistry of graphene [154]. In addition, thermal treatment extends the distance between graphene layers and ease intercalation process is achieved during electrospraying process. Therefore, TEGO is preferred as filler for the production of composite spheres. Increasing TEGO amount in electrospun solution gradually imbalances the electrostatic interaction between charges, and enlarges the sphere diameter.

Table 3.2: Synthesis conditions and characteristics of TEGO based PMMA and PS spheres and their shrinkage percentages.

	TEGO amount (wt%)	Average diameter of spheres (μm)	Average shrinkage of spheres (%)
PMMA	0	4.7 ± 0.1	-
	0.005	2.9 ± 0.1	38
	0.01	3.4 ± 0.3	29
	0.02	3.8 ± 0.1	20
PS	0	4.5 ± 0.2	-
	0.005	2.2 ± 0.1	51
	0.01	2.6 ± 0.1	42
	0.02	3.1 ± 0.4	32

Figure 3.5 exhibits SEM images of spheres sprayed by using air at atmospheric pressure in the core of the syringe. After electrospraying process without any core materials, it is observed that all types of polymers form porous and filled sphere structures. After the addition of TEGO into the polymer, it is noted that the diameter of these spheres decreases. Furthermore, Figure 3.6 presents SEM images of neat PS spheres and TEGO based PS spheres at higher magnification. By the incorporation of TEGO, the porosity of spheres decreases and the surface becomes smoother.
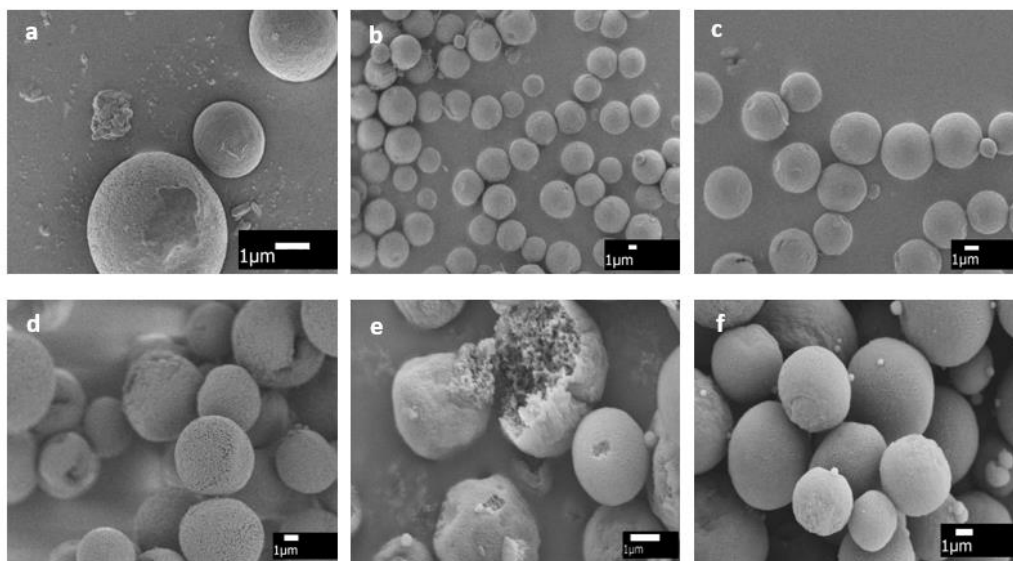
Figure 3.5 SEM images of spheres produced by (a) PMMA, (b) PMMA-0.01 wt% TEGO, (c) PMMA-0.02 wt% TEGO, and (d) PS, (e) PS-0.005 wt% TEGO, (f) PS-0.02 wt% TEGO.
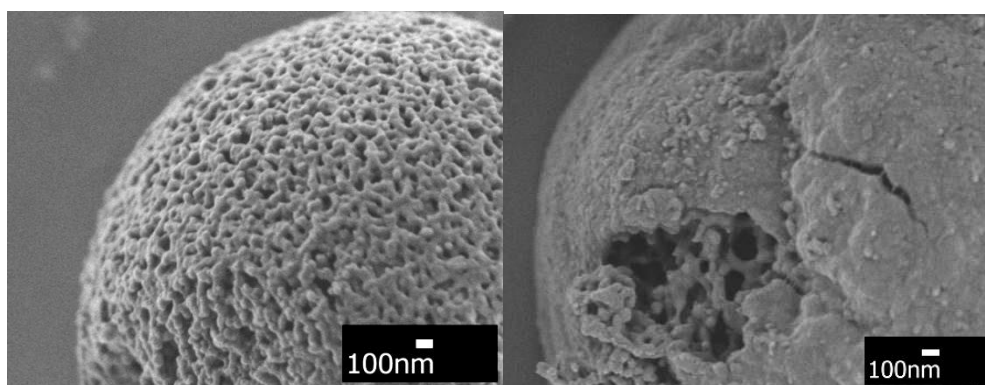
Figure 3.6 SEM images at higher magnifications of (a) PS spheres and (b) PS-0.005 wt% TEGO spheres.

XRD characterization was performed in order to prove the presence of TEGO in polymer spheres. In Figure 3.7, TEGO has a characteristic 002 peak at 26.5°. In the XRD analysis of polymer-graphene based nanocomposites, 002 peak can either completely disappear or shift to the lower region due to the intercalation of polymeric chains into graphene sheets [155], [156]. In Figure 3.7a, PMMA shows a wide diffraction peak spanning from 10° to 20° with a maximum intensity at $2\Theta\approx14.4°$ and the intensity of this peak decreases as TEGO amount increases and 2Θ shifts to lower angel values due to the

45

complete coating of multi-layer graphene by polymer chains. Also, the diffraction peak broadens and its intensity decreases by the incorporation of TEGO and thus composite becomes completely amorphous structure. In Figure 3.7b, PS has a broad diffraction peak between 15˚ and 25˚ and as the value of TEGO increases, PS diffraction peak shifts towards lower angles and its peak becomes wider by increasing TEGO amount.

The slight shifting of polymer diffraction peak to the lower angle region and the disappearance of 002 peak of TEGO bespeak that the electric field enhances the distribution of graphene sheets in polymer solution so that multi-layer graphene sheets are completely coated by polymer during sphere formation. Figure 3.8 also shows schematically how complete coverage occurs between TEGO and polymer chains and avoids restacking of multi-layer graphene sheets under electric field.
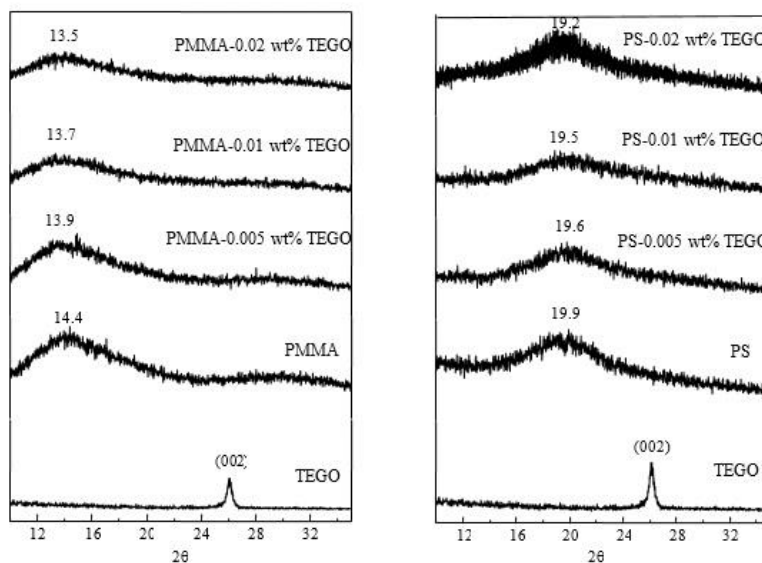
Figure 3.7 XRD spectra of (a) PMMA-TEGO spheres and (b) PS-TEGO spheres
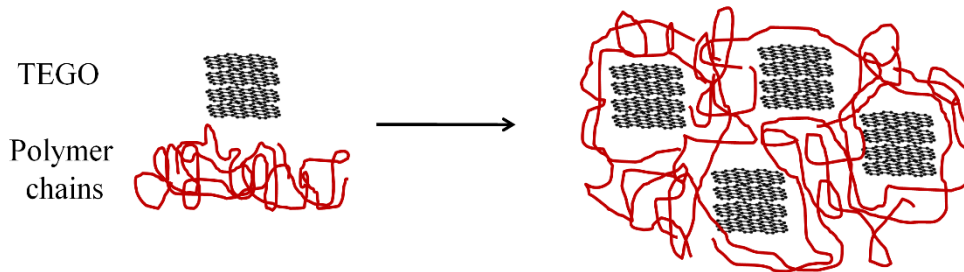
Figure 3.8 Schematic illustration of interactions between polymeric chains and TEGOsheets during sphere formation

46

Figure 3.9 shows Raman spectra of TEGO, PS, and PS-TEGO spheres. PS has characteristic Raman peaks at 3050 cm^{-1} and 2900 cm^{-1} due to the vibration of C-H bonds, 1600 cm^{-1} attributed to C=C vibrations and 995 cm^{-1} related to aromatic carbon rings [157]. In the Raman spectrum of the PS-0.02 wt% TEGO, the characteristic peaks of TEGO do not appear because of the low amount of TEGO in the polymeric spheres and overlapping of polymer main peaks with TEGO peaks. On the other hand, significant decrease in Raman peaks of PS was observed by the integration of TEGO, which also proves the presence of TEGO in the spheres.
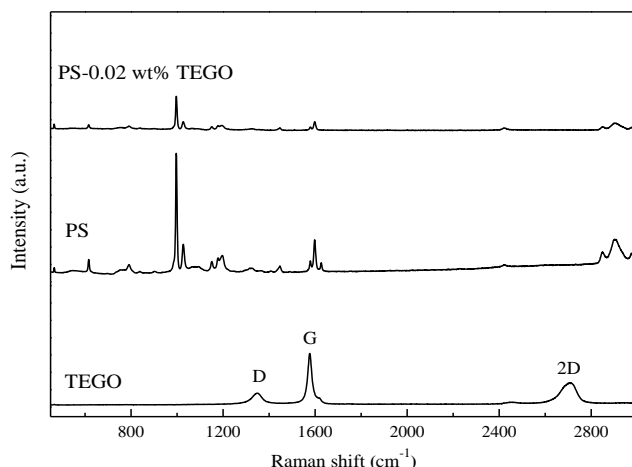
Figure 3.9 Raman spectra of TEGO, PS spheres, and PS-0.02 wt% TEGO spheres

3.3.3 The effect of core material on the hollowness of TEGO based polymeric spheres

In order to observe the effect of the core material on the hollowness of PMMA-TEGO spheres, methanol was used as a core solvent in electrospraying process. The shell solvent of polymer solution is DMF with a vapor pressure of about 516 Pa whereas methanol has higher vapor pressure about 13020 Pa. Shell formations and hollowness can be controlled by increasing solvent vapor pressure and tailoring flow rates. In addition, the evaporation rate depends on the flow rate of core solution so that three different flow rates are investigated to tailor the hollowness formation in the present study. Other system (voltage, distance between collector and syringe) and process (polymer concentration, type of solvent, TEGO amount) parameters were kept the same in each trial to see the

effect of flow rate on the morphologies of spheres. As the evaporation rate of the core solvent increases, the solvent will have sufficient time for the evaporation. Hence, low flow rate of the core solution causes hollow sphere formation, the shell is formed initially and then core solvent evaporates through the pores of shell until the spheres reaches the collector. Surface forces have a significant role in shaping the surface of the jet and controlling the porosity [158]. As the flow rate of core solvent increases, the fast evaporation of core solvent causes local phase separation, and the solvent-rich regions leaves behind porous structures during the electrospraying process and thus porous and filled spheres are formed. Increasing the flow rate further (i.e., 5 µL/min) leads to fiber formation instead of spheres.

The produced spheres were cut by using an ion beam source of FIB-SEM instrument to investigate the inside of microstructures. Figure 3.10 displays FIB-SEM images of 0.02 wt% TEGO+PMMA spheres produced utilizing the methanol as core solvent with the lowest flow rate. Before the ion bombardment, spherical structure is clearly seen in Figure 3.10a. After the ion bombardment, the shell material starts to melt upon increasing the current of the ion beam whereby one can clearly observe the hollowness within the sphere as seen in Figure 3.10b. Figure 3.11 yields the FIB-SEM images of TEGO based PMMA spheres produced with a flow rate of 2 µL/min during the ion beam bombardment process. The porous core structure is detected at the end of complete melting of shell materials as seen in Figure 3.11c. This proves that increasing the flow rate of core solvent facilitates the penetration of core solvent through shell and induces phase separations and thus leads to porous core structure. The average diameter of spheres changes from 3.4 µm to 4.6 µm by increasing the flow rate of core material because higher flow rate speeds up the evaporation process of solvent. Spraying methanol with a high flow rate of 5 µL/min totally changes the morphology and fiber formation is detected among spheres.
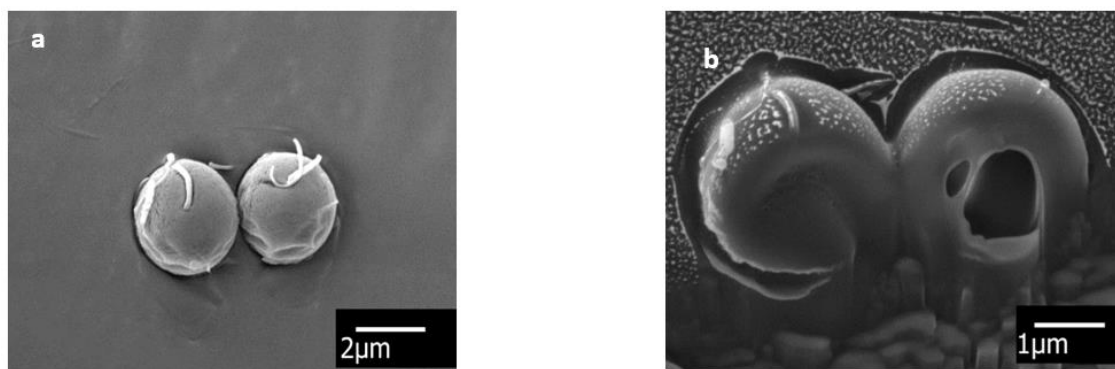
Figure 3.10 FIB-SEM images of PMMA spheres containing 0.02 wt% TEGO using methanol as a core material and a flow rate of 0.5 µL/min (a) before and (b) after ion bombardment.
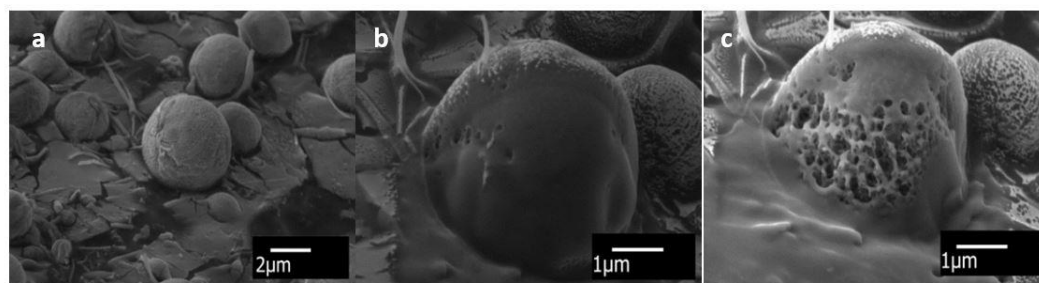
Figure 3.11 FIB-SEM images of PMMA spheres containing 0.02 wt% TEGO using methanol as a core material and a flow rate of 2 µL/min (a) before and (b) during and (c) after ion bombardment.

In addition, FIB-SEM technique is used for the observation of porous core in PMMA spheres produced by using atmospheric air in core syringe. Figure 3.12 displays FIB-SEM images of these spheres after the ion bombardment. The structure of spheres is noticeably porous even at longer bombardment period.
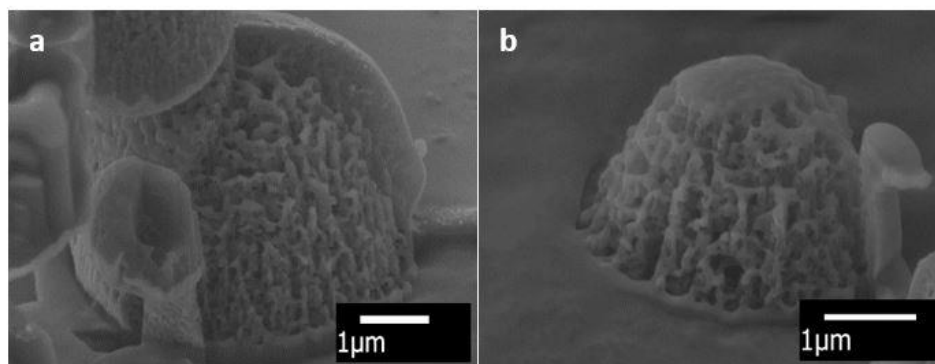
Figure 3.12 FIB-SEM images of 20 wt% PMMA spheres containing 0.02 wt% TEGO by using atmospheric air as a core material (a) and (b) after ion bombardment.

3.3.4 The effect of carbonization on the morphology of TEGO based polymeric spheres

PAN polymer is one of the most important precursors of carbon source in the production of polymeric composites. Carbonization makes PAN polymer promising especially in energy applications because its electrical and mechanical properties are significantly improved by increasing carbon content up to 95% [151]. Instead of PS and PMMA used as template materials having lower degradation temperatures between 300-400°C, PAN is chosen as a carrying polymer for the carbonization process to form carbon network with graphene sheets since PAN undergoes heating process at high temperature in the range of 800-3000°C [151].

At the initial step of our process, 5 wt% PAN, 5 wt% PAN-0.02 wt% TEGO and 3.5 wt% PAN-0.05 wt% TEGO solutions were sprayed separately without using any core material to produce PAN-based spheres. Fabricated spheres containing 5 wt% PAN and 5 wt% PAN-0.02 wt% formed half hollow spheres (donut-shaped structures) and carbonization does not affect the morphologies of these structures as seen in Figure 3.13. The reason for donut-shaped formation might be due to the combined effects of low polymer concentration, high intrinsic viscosity and applied electric forces. Thus, a rather interesting sphere structure is formed during the discharge process of the polymeric mixture from the tip of syringe. Average diameters of 5 wt% PAN and 5 wt% PAN-0.02 wt% TEGO spheres are about 1.6 μm and 2.9 μm, respectively. The incorporation of TEGO enlarges the diameter of spheres, which might stem from better dispersion and alignment of multi-layer graphene sheets in higher viscosity of PAN solution during electrospraying process when compared to the results of PMMA and PS solutions.

After the carbonization process, both neat PAN and TEGO based PAN spheres shrink about 75%, and the diameters of PAN and TEGO based PAN spheres decrease down to nanometer scale and become 400 and 700 nm, respectively. Carbonization leads

to the formation of more packed spheres having less porosity (Figure 3.13b and Figure 3.13d).
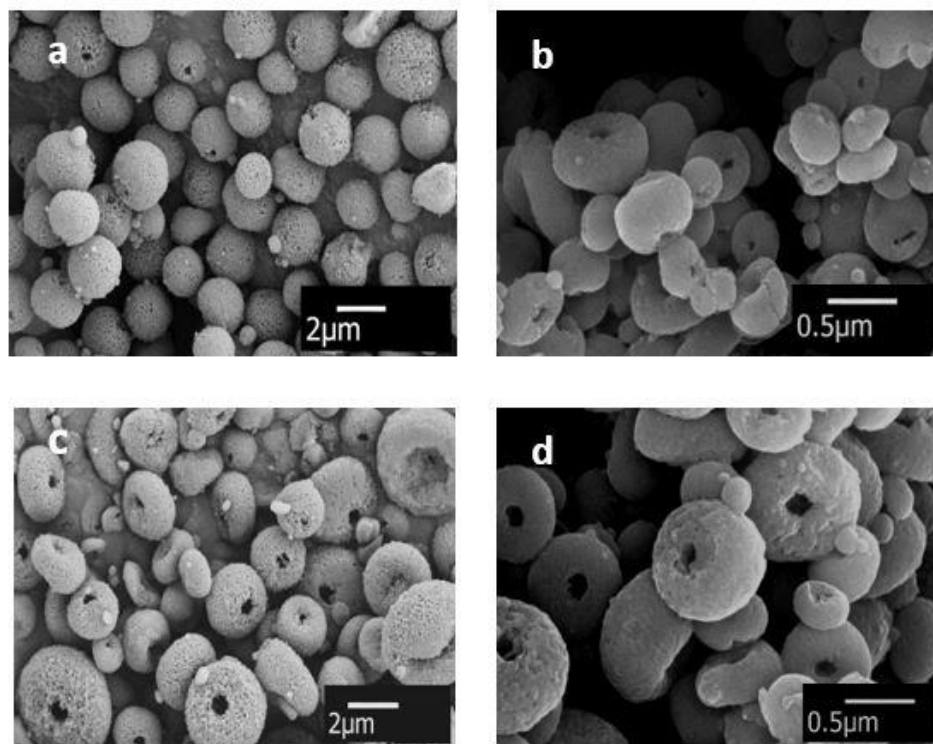
Figure 3.13 SEM images of 5 wt% PAN spheres (a) before and (b) after carbonization, and 5 wt% PAN-0.02 wt% TEGO spheres (c) before and (d) after carbonization.

In another PAN sphere production, TEGO amount increased up to 0.05 wt% and polymer concentration decreased down to 3.5 wt% in order to investigate the changes in morphologies of spheres. By increasing TEGO content, the zero shear viscosity of electrospun solution is expected to increase which will require larger electric field strength to deform the droplet whereby the diameter of spheres gets bigger. Figure 3.14 shows SEM images of 3.5 wt% PAN-0.05 wt% TEGO before and after carbonization. The average diameter of spheres before carbonization is about 6.5 μm. In Figure 3.14b and Figure 3.14c, one can immediately notice an interesting microstructure composed of two disjointed spheres which might have been formed due to phase separation because of high TEGO amount in electrospun solution. EDX results confirm that the average carbon wt% in outer sphere shell is about 71 whereas the inner sphere shell has 62 % carbon. High

carbon content in outer sphere and the wrinkles in Figure 3.14b point to the high amount of graphene sheets and less polymer intercalation in the outer part of the structure. Consequently, TEGO starts phase separation after the complete diffusion of polymer chains through graphene layers and spheres are entwined together and isolated from each other. Moreover, since the inner layer should have smaller viscosity than the outer layer referring to the graphene content as measured by the EDX, during electrospraying process, the inner layer should be deformed much easier than the outer layer by the combined surface forces (i.e., electric and surface tension forces).

After heat treatment, TEGO based PAN spheres collapses totally and the boundaries on the surface of layers and the smooth surfaces are clearly seen in Figure 3.14d. When compared to the results having high polymer concentration and low TEGO amount given in Figure 3.13, the porosity of surfaces in Figure 3.14 decreases significantly by increasing TEGO and reducing polymer concentration. These results confirmed the significance of solvent evaporation rate, solution viscosity, polymer concentration and TEGO amount on sphere morphology.
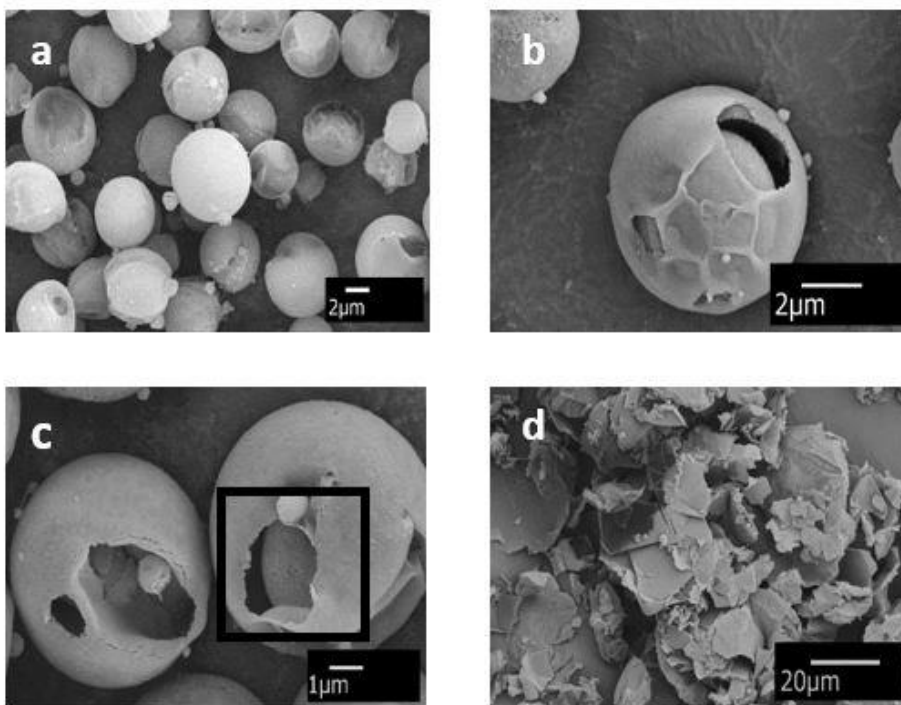
Figure 3.14 SEM images of 3.5 wt% PAN-0.05 wt% TEGO spheres (a-c) before and (d) after carbonization

Raman spectra of TEGO and 5 wt% PAN-0.02 wt% TEGO spheres before and after carbonization are shown in Figure 3.15a. In the Raman spectrum of carbonized TEGO based PAN spheres, two peaks appears: the peak at ~1340 cm^{-1} related to D band of graphene and the peak around ~1580 cm^{-1} attributed to G band. I_D/I_G ratio of carbonized spheres is approximately 0.9 higher than I_D/I_G ratio of TEGO as 0.2 which shows the growing of graphene-like structures and reordering of aromatic groups towards graphene networks at higher temperatures [159]. Figure 3.15b shows FTIR spectra of TEGO and produced PAN spheres. In the FTIR spectrum of TEGO, there is no sharp peak since thermal exfoliation of GO removes most of the oxygen functional groups and the resultant material has high carbon content. Only a weak peak at around 1722 cm^{-1} appears which is assigned to carbonyl stretching of C=O [160]. PAN spheres show characteristic peaks at 2930 cm^{-1}, 2250 cm^{-1}, and 1450 cm^{-1} which are associated with C-H bonds in CH$_2$, nitrile bond (C≡N), and tensile vibration of CH$_2$, respectively [161]. By the incorporation of TEGO into the structure, a sharp peak at 1720 cm^{-1} can be distinguished easily related to the stretching vibration from carbonyl group (C=O) of TEGO. Thus, this confirms the presence of TEGO in the structure. After applying heat treatment, the reduction in peak intensities at 2930 cm^{-1} and 1450 cm^{-1} and the disappearance of the peak at 2250 cm^{-1} indicate the cyclization and dehydrogenation of TEGO based PAN spheres during carbonization process.
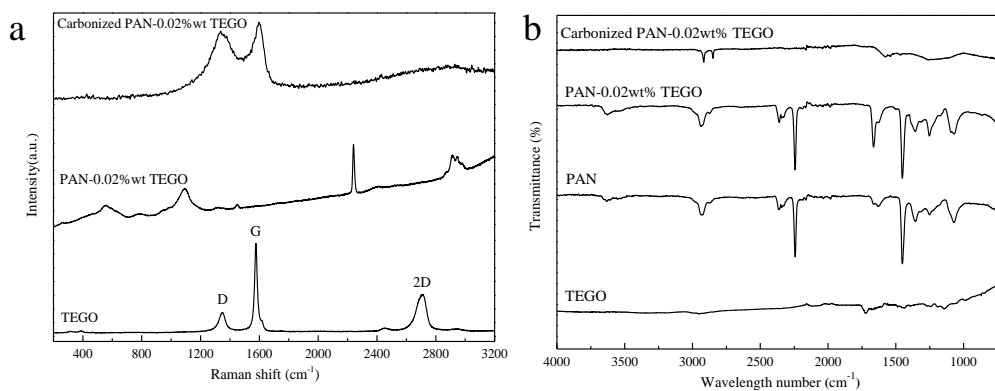
Figure 3.15 (a) Raman spectra and (b) FTIR spectra of TEGO, and 5 wt % PAN-0.02 wt% TEGO spheres before and after carbonization.

3.4 Conclusions

In this study, hollow and filled graphene based polymeric spheres are successfully produced by using core-shell electrospraying technique. Without applying any post treatment or using any template, it is possible to control the hollowness of spheres by using core solvent and changing its flow rate in one-step process. This technique also diminishes crumbling and agglomeration of 2D graphene sheets and provides better dispersion of graphene layers through polymer chains. In this study, PS and PMMA are used as carrier polymers to convert 2D graphene sheets into 3D dimensional spheres since these polymers are easily processable for bead formation and are widely used as templates to produce hollow structures. In addition, PAN polymer is preferred as a carrier polymer to improve connections between TEGO sheets, and after carbonization, carbon content of spheres and graphene-like growing significantly increase. Decreasing PAN concentration and increasing TEGO amount lead to the formation of disjointed spheres in the same structure and this phenomenon is still under investigation. The control of solution parameters in bead formation might give new direction to several applications including aerosols, surface coatings, membranes, and drug delivery systems. In order to find the proper concentration for the fabrication of polymeric spheres, a new diagram based on concentration and molecular weight of PMMA, PS and PAN in DMF solvent is constructed by using Mark-Houwink-Sakurada equations. The obtained data from the diagram is consistent with the experimental results. In the presence of graphene in the sphere structure, the intercalation and shifting in XRD patterns towards lower angles indicate the presence of graphene sheets in polymer matrix. In the proposed technique, the number of polymeric shells can be increased by increasing syringe number in electrospraying set-up, and multi-layer composite spheres having enhanced multi-functionality can be produced by using different polymers with different degree of hydrophilicity. In addition, catalysts can be deposited on the surface of polymeric shells and electrolytes can be inserted in core part during electrospraying. Consequently, multi-axial core shell electrospraying technique will increase accessible surface area of 2D

graphene sheets and preserve characteristic properties of graphene in bulk systems, and open up new directions especially in energy applications such as Li-ion batteries, fuel cells, and supercapacitors.

CHAPTER 4 **DESIGN OF Pt SUPPORTED 1D AND 3D MULTI-LAYER GRAPHENE-BASED STRUCTURAL COMPOSITE ELECTRODES WITH CONTROLLED MORPHOLOGY BY CORE-SHELL ELECTROSPINNING/ELECTROSPRAYING**

4.1 Introduction

In the recent years, a rapid increase in the global energy consumption persuades scientists to develop new eco-friendly energy storage devices. In the field of energy storage, electrode design plays a significant role by providing high surface area, fast electron mobility, high electrical conductivity and good chemical stability to attain high electrochemical performance [162]. Especially carbon materials are widely used as an electrode material in electrochemical energy storage systems owing to their rich variety of dimensionality and large surface area [105]. Among various carbon-based materials, graphene becomes a promising candidate since it has long-range π conjugation and thus fast electron mobility which makes it extremely attractive for energy storage devices [61]. There are different types of graphene production techniques by using top-down and bottom-up approaches. The main problem in the utilization of graphene in bulk applications is its restacking and agglomeration and the formation of crumpled structure leading to a significant decrease in the surface area, electrical conductivity and thus great loss of electrochemical activity. Up to now, many efforts have been made to overcome this obstacle by the integration of 2D graphene sheets into macroscopic structures through different methods including chemical vapor deposition, encapsulation, self-assembly and wet spinning [40], [163]. With these methods, it is possible to convert graphene into several structures such as graphene fibers [164], spheres [130], films [165], and networks [95].

Template-assisted method and self-assembly technique are the most common used strategies to obtain 3D graphene-based structures. In one of the studies, Fan *et al.* [109] fabricated graphene-wrapped polyaniline hollow spheres as an electrode material by using polystyrene spheres as template and obtained a high specific capacitance of 614 F/g at a current density of 1 A/g and maintained the capacitance at around 90% after 500 cycles.

In another work, Xu *et al.* [166] produced microporous carbon spheres incorporated into 3D graphene frameworks *via* wet chemistry and self-assembly techniques, which showed a specific capacitance of 288.8 F/g at a current density of 0.5 A/g. However, in these aforementioned processes, it is not easy to control structural properties such as porosity and hollowness since the morphology directly depends on the chosen templates. At this point, electrospinning is an alternative and easy method for the production of graphene-based structures in the form of spheres [8], [167] and fibers [168] by adjusting the polymer concentration and surface tension of droplet. The electrodes produced by electrospinning have an ability to form a continuous network, which is essential for the charge transport and provides conducting framework and excellent interconnectivity. In one of work, Kim *et al.* [169] examined the electrochemical behavior of graphene/carbon nanofiber composite electrode produced *via* classical electrospinning technique by using graphene oxide (GO) and polyacrylonitrile (PAN) as carbon precursor having high conductivity and a specific capacitance of 146.6 F/g at a current density of 1 mA/cm^{-2}. Recently, core-shell electrospinning has received great attention in order to attain multi-functionality and utilize different materials in one-step process by eliminating coating and deposition steps and thus expand the potential applications of fabricated structures [168], [170]. Kou *et al.* [171] fabricated polyelectrolyte-wrapped graphene core-sheath fibers as high-energy density electronics by co-axial electrospinning of reduced GO solution as core and sodium carboxymethyl cellulose as shell material following by reduction and washing processes. Instead of morphology design in electrode structures, the integration of noble metals improves electrical conductivity and electrochemical stability in graphene electrodes used in Li-ion batteries, fuel cells and supercapacitors [172]. Among them, Pt has gained great interest due to its lowest over potential and stability which facilitate the electron transport during redox reactions [172], [173]. For instance, Zhang *et al*. [174] fabricated graphene/Pt films having a high capacitance of 120 F/g at high scan rate of 50 A/g to enhance the conductivity of charges, and thus give higher reversible capacitance at high rates. So far, there are several attempts for the fabrication of graphene-based fibers as electrodes in the energy storage systems by applying classical and core-shell electrospinning techniques. To the best of our knowledge, there is no related work to

control the dimension of graphene based electrodes in different forms of foam and sphere by applying core-shell electrospinning technology.

In the present study, Pt deposited 1D graphene-based fiber and 3D graphene-based sphere and foam electrodes were produced by core-shell electrospinning/electrospraying techniques. Figure 4.1 shows the schematic representation of fabrication process for Pt decorated graphene-based foam, fibers and spheres by core–shell electrospraying. During electrospinning, thermally exfoliated multi-layer graphene layers were transformed into the three different forms of fiber, foam and sphere by using a carrier polymer by altering solution parameters of polymer concentration and molecular weight of polymer and process parameter of applied voltage. In the electrode structure, PAN polymer was used as a carrier to increase carbon network. Due to the high catalytic activity and good chemical stability against oxidation, Pt particles was chosen as catalyst and deposited at low loadings in the structures. Structural and morphological properties of structures were analyzed by spectroscopic and microscopic techniques in details. The electrochemical performance of Pt deposited graphene-based carbon structures as electrodes was investigated by cyclic voltammetry and galvanostatic charge-discharge.
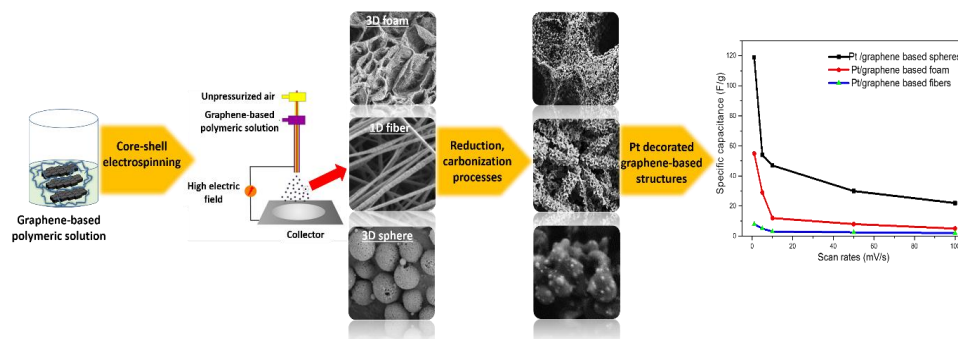
Figure 4.1 Schematic representation of the fabrication process of Pt decorated graphene-based foam, fibers, and spheres

4.2 Experimental

4.2.1 Materials

Polyacrylonitrile (PAN, M_w: 150000 g/mol), N, N-dimethyl formamide (DMF, 99%), chloroplatinic acid (H_2PtCl_6, 8 wt% in H_2O), and hydrazine hydrate (N_2H_4) were

purchased from Sigma-Aldrich. Low molecular weight PAN (M_w: 45000 g/mol) was synthesized through free radical polymerization method [175]. TEGO Grade 2 (thermally exfoliated graphene oxide) having average number of graphene layers of 27 calculated from XRD data by using Debye Scherer equations and 4% oxygen content was obtained from Nanografen Co. The characterization results of TEGO were given in Appendix B1.

4.2.2 Fabrication of graphene-based structures by core-shell electrospinning

Foam, fiber and sphere-like graphene-based structures were produced at ambient conditions by using tri-axial electrospinning equipment purchased from Yflow Company. PAN polymer containing graphene sheets were used as a shell material in the proposed structures. In the shell material, 0.02 wt% TEGO based on the weight of solvent was dispersed in DMF by probe sonicator for 20 minutes to get homogeneous dispersion. The optimum amount of 0.02 wt% TEGO was chosen for the production of electrospun structures and the detailed results about optimization process were given in our previous paper [8]. Two different polymer concentrations of 1 wt% and 5 wt% PAN with a molecular weight of M_w=150000 g/mol were adjusted to get foam and fiber structures, respectively. In case of graphene-based sphere production, low molecular weight PAN polymer (Mw=45000 g/mol) was used as 5 wt% PAN in 0.02 wt% TEGO/DMF mixture.

For the production of graphene-based foam, 1 wt% PAN solution was electrosprayed with an applied voltage of 18 kV and flow rate of 5 μL/min. In the case of fibers, as-prepared 5 wt% PAN solution was electrospun with an applied voltage of 10 kV and flow rate of 8 μL/min. For the production of graphene-based spheres, electric field was adjusted as 13 kV and flow rate was kept as 10 μL/min by using 5 wt% low Mw PAN based solution. All electrospinning/electrospraying experiments were performed with constant working distance of 10 cm and the core part of nozzle was kept empty during each process.

4.2.3 Pt deposition

In each material, H_2PtCl_6 was added into the solution to observe 0.05 wt% Pt based on the polymer weight in the final structure. The amount of Pt was optimized by the

addition of two different amounts of 0.05 wt% and 0.1 wt% of Pt in the fiber structure. As it can be seen in Appendix B2, high amount loading of 0.1 wt%, results in the serious agglomeration problem in the surface of fibers. Thus 0.05 wt% was selected as optimized amount for the decoration of Pt on the surface of graphene-based architectures. In case of graphene-based foam and fibers, Pt catalyst was dispersed in electrospun solution and impregnated in the matrix during electrospinning process in one step process. On the other hand, Pt particles were dispersed on electrospun graphene spheres after carbonization process to improve capacitance value.

In order to obtain Pt from H_2PtCI_6, hydrazine hydrate was used as reducing agent in distilled water (1:100, v:v). Aqueous hydrazine solution is used as a non-solvent for PAN polymer not to damage the structure [176]. Electrosprayed/electrospun graphene-based foam and fibers were immersed into hydrazine hydrate solution and kept for 1 day at room temperature and then washed several times with water and kept for drying in oven. After the reduction process, the color of the materials turned into gray indicating that Pt ions were reduced into Pt metal particles. For graphene-based spheres, the same steps of reduction were applied after carbonization process.

4.2.4 Carbonization process

Heat treatment of the produced fibers, spheres and foam was performed in two steps to increase carbon amount in the structure and thus improve electrochemical properties of the designed electrodes. In the first step, samples were stabilized by applying oxidation process by heating up to 300˚C under air for 30 min and thus the structures became more stable at higher temperature without transition into melting phase. In the second step, these samples were heated up to 1000˚C under argon atmosphere.

4.2.5 Electrode preparation and their electrochemical tests

Electrochemical performance of the carbonized samples was evaluated by PARSTAT MC (Princeton Applied Research) under a three-electrode system in 0.5 M H_2SO_4 aqueous electrolyte using platinum wire as a counter electrode and Ag/AgCl as a reference electrode in a typical potential range for aqueous electrolytes of 0-0.8 V.

60

Working electrodes were prepared by dispersing graphene-based materials in 3 mL distilled water using probe sonicator and then 0.5 mL of Nafion solution (10 wt%) used as a binder was added into the mixture and stirred for 1 hour to get complete wetting. Then, the solution was dispersed on the Toray carbon film by drop-casting and dried the electrode in a 90°C oven for 2 hours.

4.2.6 Characterization

The morphology of samples were analyzed by Leo Supra 35VP field emission, TESCAN LYRA3 focused ion beam Scanning Electron Microscopies (SEM) and JEOL ARM 200CF Transmission Electron Microscope (TEM). Elemental analysis of samples was conducted by using Energy-Dispersive X-ray (EDX) analyzing system. X-ray diffraction (XRD) measurements were carried out by using a Bruker AXS advance powder diffractometer with a CuKα radiation source. Raman spectroscopy was used to identify the surface characteristics of samples by using a Renishaw inVia Reflex Raman Microscopy System with the laser wavelength of 532 nm at room temperature in the range of 100-3500 cm^{-1}. The functional groups in the structures were determined by Netzsch Fourier Transform Infrared Spectroscopy (FTIR).

4.3 Results and discussion

4.3.1 The effect of polymer concentration on the morphology of electrospun structures

In the electrospinning process, viscosity of the solution plays an important role to determine the final morphology of electrospun structures. During electrospinning process, the droplet at the tip of the nozzle is being subjected to the electric field; it starts to distort which is a result of balancing force between electric field and surface tension of droplet. When the surface tension of droplet is overcome to the voltage, a polymeric jet is initiated from the nozzle tip to the collector. The viscosity of a solution depends on the polymer molecular weight and concentration of polymeric solution. In the case of low viscosity solution, the jet breaks up to the droplets, which cause the formation of spheres and foam-like structures. The greater the viscosity is, the more stable polymeric jet is be able to

travel through grounded collector [177]. In our previous work [8], we showed the effect of polymer concentration and molecular weight on the formation of different polymeric structures by using Mark-Houwink-Sakurada equation (Appendix B3). Figure 4.2 represents the concentration as a function of molecular weight of PAN where, solid line shows the concentration threshold of PAN polymer where above and on the line fiber formation is dominant (see Appendix B). By moving toward lower regions, spherical and foam-like structures are started to form. On the other hand, each point in the graph corresponds to the different PAN concentration with different molecular weight, which are selected for the fabrication of fibers, spheres, and foam colored as red, purple, and blue, respectively. Hence, it is possible to get the structures with the desired morphology and size such as spheres [8], foams, and fibers [57] by tailoring system (e.g. flow rate, applied voltage, working distance between nozzle and collector) and solution parameters (e.g. polymer concentration).
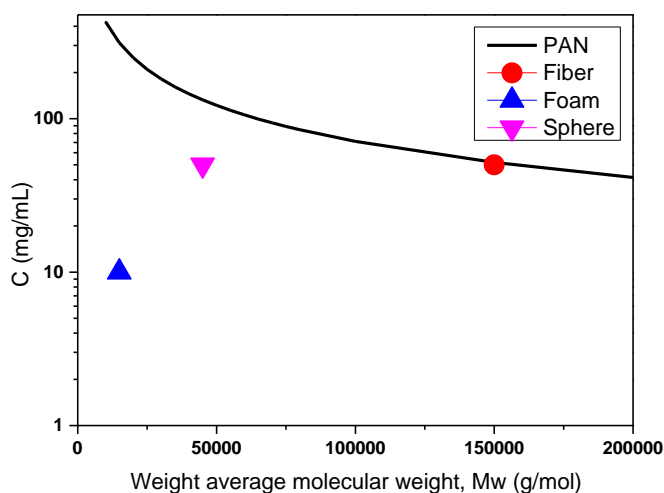
Figure 4.2 Entanglement concentration as a function of the molecular weight of PAN polymer.

In the first part of work, structural morphologies of electrospun/electrosprayed structures were tailored by controlling polymer molecular weight and polymer concentration. Three different polymeric solutions with different concentrations of 1 wt% and 5 wt% and different PAN molecular weights were prepared to monitor the effect of

concentration and viscosity on the morphology of structures. Table 4.1 summarizes the synthesis conditions of graphene-based structures. The results showed that low polymer concentration brought about the formation of porous interconnected foam. Figure Figure 4.3a represents SEM image of 1 wt% PAN electrospun foam with average pore size of 100 μm. On the other hand, as PAN concentration increased up to 5 wt%, homogeneous and uniform fibers having an average diameter of 150 nm were obtained as seen in Figure 4.3b. Graphene-based spheres having donut-shaped structure with an average diameter of 1.6 μm were fabricated by electrospraying 5 wt% PAN (M_w= 45000 g/mol) shown in Figure 4.3c and the production details of these spheres were given in our previous publication [8]. The reason behind the formation of donut-shaped structure is the combined effects of low polymer concentration, high intrinsic viscosity and applied electric forces at the tip of syringe during the discharge of electrospun solution [8]. Consequently, it is possible to convert TEGO sheets into 1D and 3D structures by using a carrier polymer by tailoring the parameters of applied voltage and solution viscosity.

Table 4.1 The effect of polymer molecular weight and synthesis conditions on the final morphology of structures

Morphology	Mw of PAN (g/mol)	Polymer concentration (wt%)	Applied voltage (kV)	Flow rate (μL/min)
Foam	150000	1	18	5
Fiber	150000	5	10	8
Sphere	45000	5	15	10
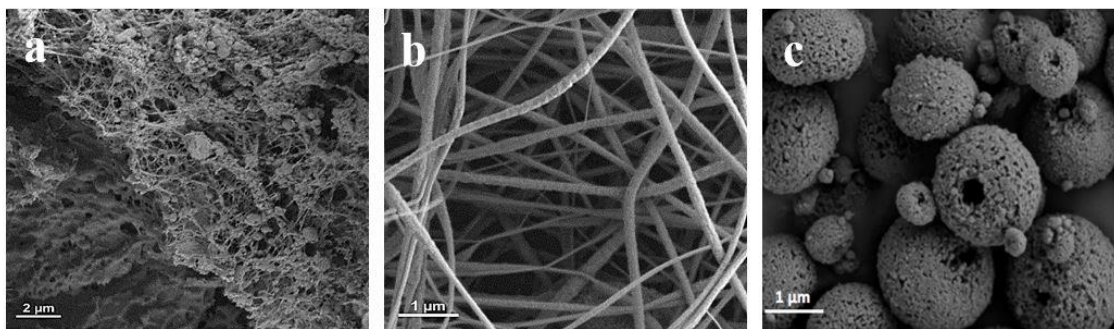
Figure 4.3. SEM images of (a) PAN-based foam, (b) PAN-based fibers and (c) PAN-based spheres

4.3.2 Pt decorated 1D and 3D graphene-based structures

Electrospinning/electrospraying technique provides homogenous distribution of graphene sheets into polymeric matrix by preventing their agglomeration and restacking under electric field [8], [178]. In order to increase the conductivity, Pt particles were integrated into graphene-based foam, fibers, and spheres during electrospinning and after post-process. In case of foam and fiber structures, Pt nanoparticles were integrated during electrospraying/electrospinning. Figure 4.4a shows SEM image of electrosprayed graphene-based foam having pores in the range of micron size. It should be noted that desirable pore size could be achieved by controlling the polymer drying time and adjusting solvent vapor pressure [179], [180]. After reduction process, structure still preserved its framework shown in Figure 4.4b. In order to improve carbon content, carbonization was applied on the reduced foam. Figure 4.4c represents SEM image of Pt decorated 3D graphene-based foam after carbonization process. Pt nanoparticles with an average length of 50 nm in cubical form were distributed homogeneously on the surface of graphene-based foam (Figure 4.4d). The large diameter of Pt might stem from the growth of Pt nanoparticles during the heat treatment of foam. According to Sellin *et al.,* [181] Pt grains under inert atmosphere (e.g. argon) started the reconstruction after 250 ˚C resulted in the grain growth and agglomeration of Pt particles.
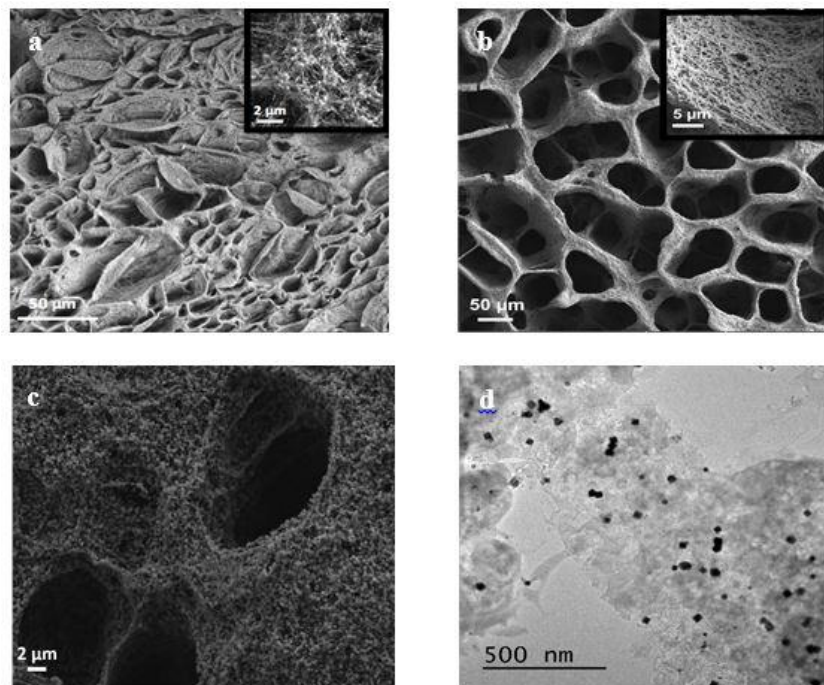
Figure 4.4 SEM images of **(a)** electrosprayed, **(b)** reduced and **(c)** carbonized Pt decorated graphene-based foam, and **(d)** TEM image of Pt decorated foam

Figure 4.5 shows the fabrication steps of Pt decorated graphene-based fibers. Graphene sheets and Pt nanoparticles were integrated into the PAN solution with a polymer concentration of 5 wt%, where higher concentration of PAN polymer resulted in the formation of homogeneous fibers with an average diameter of 100 nm. Figure 4.5a shows the SEM image of graphene-based fibers. After the reduction process, well-dispersed Pt nanoparticles appeared on the surface of fibers shown in Figure 4.5b where the diameter of reduced fibers increased up to 250 nm due to the growth of Pt nanoparticles all over the surface of fibers. Figure 4.5c represents the SEM image of carbonized graphene-based fibers having leaf-like structure owing to the expansion of graphene and the growth of Pt during carbonization. As seen in Figure 4.6a, after applying heat treatment, Pt particles with the average size of 45 nm were grown and graphene layers were exfoliated on the surface of carbonized fibers. The large diameter of Pt particles, as discussed above, is due to the Pt agglomeration during carbonization process. In this structure, Pt catalysts were on graphene sheets but not seen clearly in TEM image in Figure 4.6b since leaf-like exfoliation on fiber surface caused the formation of wrinkled

structures and catalysts were placed under these structures. In addition, it is noticeable that using unpressurized air as core material during electrospinning leads to the formation of the hollow fibers in Appendix B4.
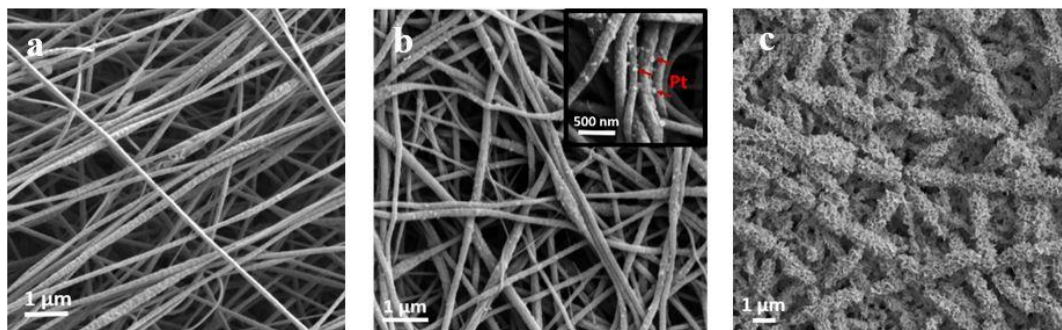
Figure 4.5 SEM images of **(a)** electrospun, **(b)** reduced and, **(c)** carbonized Pt decorated graphene-based fibers
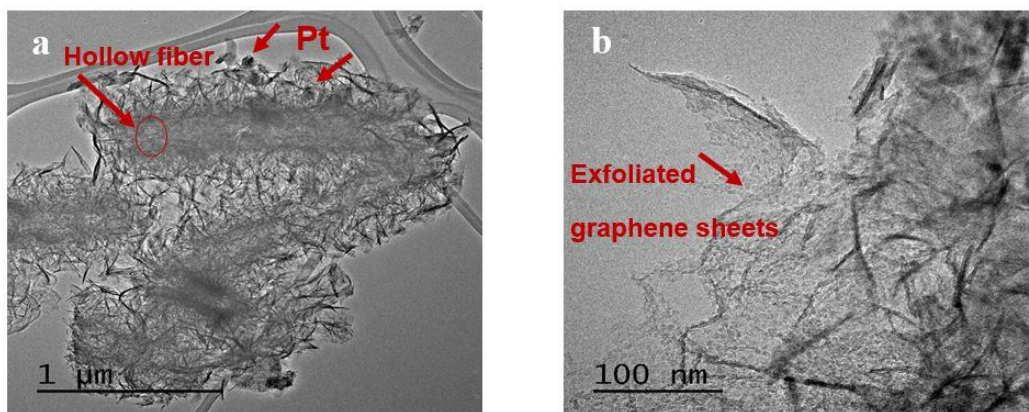
Figure 4.6 **(a)** and **(b)** TEM images of Pt decorated graphene-based fibers at different magnifications

Figure 4.7 represents SEM images of graphene-based spheres after electrospraying, carbonization and Pt deposition. Graphene spheres with an average diameter of 2.9 μm were fabricated by electrospraying of low M_w PAN solution containing graphene sheets (Figure 4.7a). Low Mw PAN having high intrinsic viscosity and high electric field during process are main parameters that cause the formation of donut-shaped spheres. After carbonization, graphene-based spheres shrank about 75%, and the diameter decreased down to 700 nm (Figure 4.7b) [8]. The decoration process of Pt nanoparticles was

performed on the carbonized graphene-based spheres shown in Figure 4.7c. Pt nanoparticles with an average diameter of 4 nm were decorated homogeneously on the surface of graphene-based spheres in Figure Figure 4.7d. The addition of Pt particles after carbonization process brought about the formation of smaller Pt particles rather than foam and fibers since heat treatment accelerates the growth process of Pt particles.
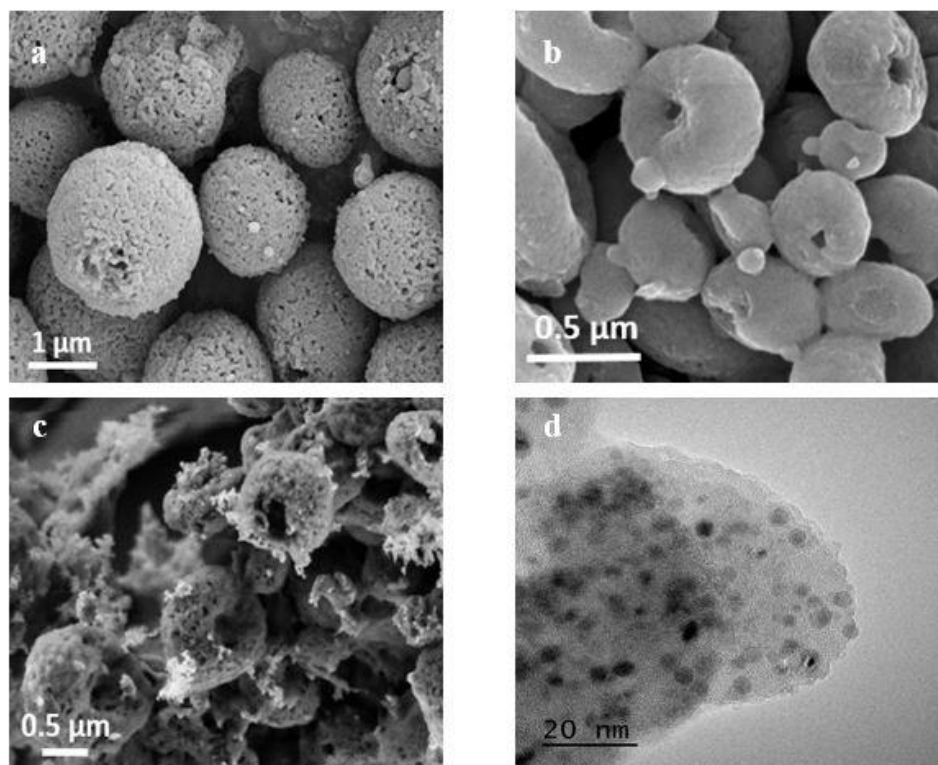
Figure 4.7. SEM images of (a) electrosprayed, (b) reduced, (c) carbonized Pt decorated graphene-based spheres, and (d) TEM image of Pt decorated spheres

Figure 4.8 represents the distribution of Pt on the surface of graphene-based foam, fibers, and spheres. Although Pt was loaded with equal amounts into the structures, there were variations in the distribution of Pt particles on the surface of structures coming from the morphological differences of the samples. EDX results confirm that the average Pt wt% in sphere structure is 20, whereas in the case of fiber and foam this amount decreases down to 5 and 9, respectively. The elemental mapping results of the samples are given in Appendix B5 and Appendix B6. The Pt particles on fiber and foam surface were distributed uniformly but during heat treatment, the size of Pt particles was increased to

45 nm and 50 nm, respectively due to the reconstruction and agglomeration of particles [181]. In the case of graphene-based spheres, Pt nanoparticles was distributed densely with a size of few nanometers.
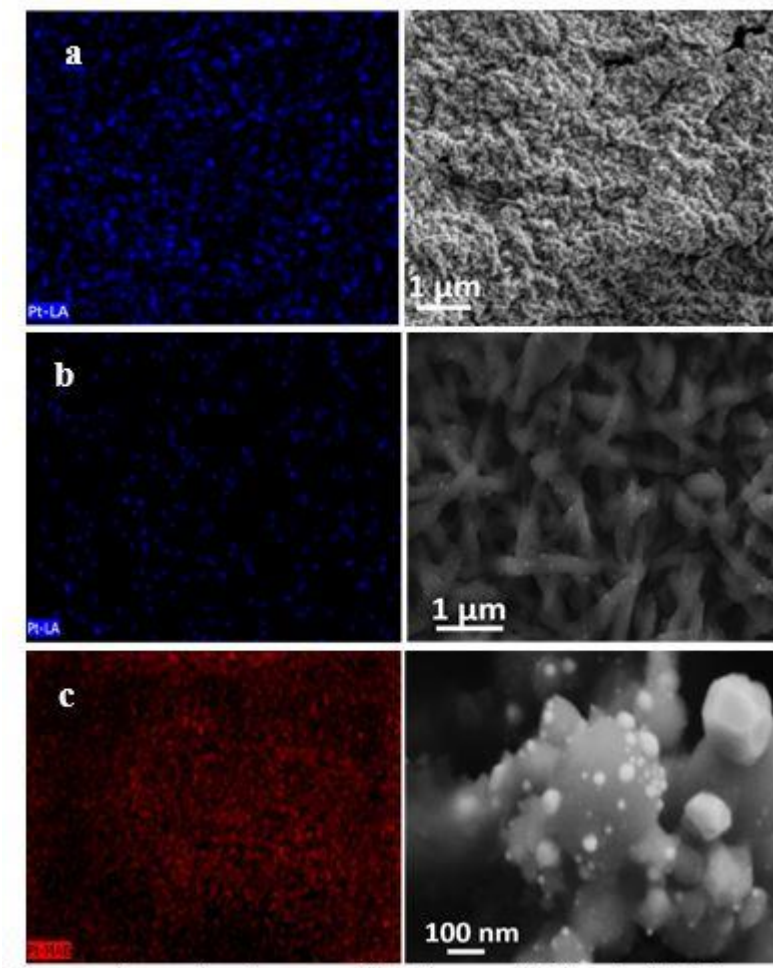
Figure 4.8. Elemental mapping images of Pt element (left) and SEM images (right) of Pt decorated graphene-based (a) foam, (b) fiber, and (c) sphere.

XRD characterization was performed to confirm the presence of Pt in graphen based structures.

Figure 4.9 shows the XRD spectrum of Pt decorated graphene-based fibers. TEGO shows a characteristic 002 peak at $2\theta = 26.5°$ [8]. On the other hand, the characteristic peaks at $2\theta = 39°$, $45.8°$, and $67°$ are attributed to the (111), (200), and (220) planes of the face-centered cubic (FCC) crystal lattice of Pt, respectively [182]. The high intensity of Pt

characteristic peaks compared to graphene characteristic peak may stem from the low amount of TEGO in the structure and growing of Pt particles during heat treatment process.
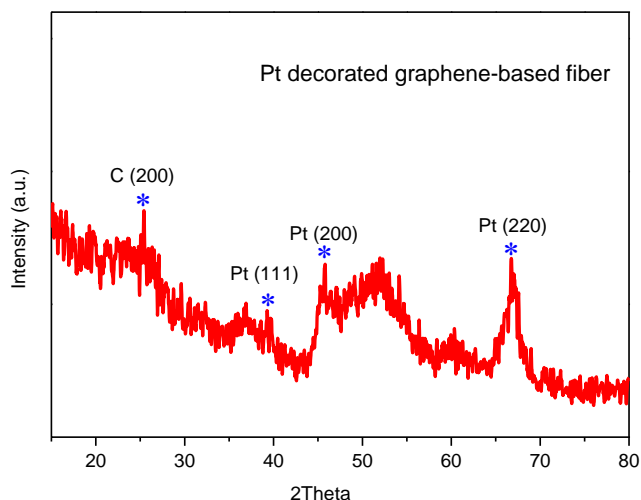
Figure 4.9 XRD spectrum of Pt decorated graphene-based fiber after carbonization process

Figure 4.10a exhibits FTIR spectra of Pt decorated neat electrospun, reduced and carbonized graphene-based fibers. PAN shows characteristic peaks at 2930 cm^{-1}, 2250 cm^{-1}, and 1450 cm^{-1} belonging to C–H bonds in CH$_2$, nitrile bond (C≡N), and tensile vibration of CH$_2$, respectively [161]. There is a significant decrease in the intensity of C=O bond at around 1660 cm^{-1} after hydrazine reduction and this proves successful reduction process and decrease in oxygen functional groups. After applying heat treatment, no characteristic peak was observed due to high carbon content in fiber structure. Figure 4.10b displays Raman analysis of TEGO sheets, Pt decorated fiber and Pt decorated graphene-based fiber. TEGO sheets have three main characteristic peaks at 1338 cm^{-1}, 1577 cm^{-1}, and 2750 cm^{-1} known as D, G, and 2D peaks, respectively [8]. On the other hand, in the Raman spectrum of Pt decorated fiber, the presence of D peak at 1342 cm^{-1} and G peak at 1596 cm^{-1} are attributed to the disordered carbon structure and in-plane vibration of sp^2 carbon atoms, respectively [178]. The ratio of D and G peak intensities (I_D/I_G) is a way to measure the defects in the carbon-based structures. As I_D/I_G increases, sp^2 bonds are broken and thus

more defects appear in the structure [83]. Pt decorated fibers show an I_D/I_G ratio of 0.93 whereas by the addition of TEGO to the structure, this value increases up to 0.98, which indicates the growing of carbon network on graphene sheets after carbonization. The structural properties of Pt decorated graphene-based foam and spheres are given in Appendix B7 and Appendix B8, respectively.
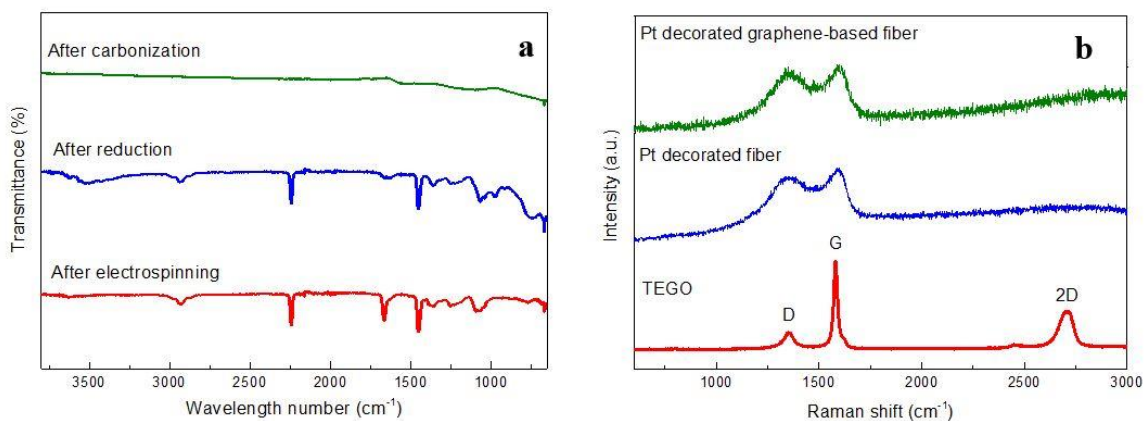
Figure 4.10 **(a)** FTIR spectra of neat, reduced, and carbonized Pt decorated graphene-based fibers, and **(b)** Raman spectra of TEGO, Pt decorated fibers without graphene and Pt decorated graphene-based fibers

4.3.3 Investigation of electrochemical performance of 1D and 3D electrodes

The electrochemical behavior of Pt decorated graphene-based structures with different morphologies was investigated by standard cyclic voltammetry (CV) and galvanostatic charge-discharge technique in a three-electrode cell. The specific capacitance of electrodes was measured using following equation:

$$C = IdV/(2m\vartheta\Delta V) \tag{1}$$

where C represents the specific capacitance (F/g), I is the current (A), m indicates the mass of active materials (g), ϑ is the potential scan rate (V/s), and ΔV is the applied voltage window (V). Table **4.2** gives the summary of CV results of fabricated electrodes regarding the dimension of the structures. In order to understand the dimension effect of graphene sheets on the electrochemical behavior of electrodes, CV test of Pt decorated 2D TEGO

70

sheets was also performed at the initial stage. TEGO-based electrode did not show any capacitance behavior due to its nearly linear CV curve as seen in CV plot of Pt decorated TEGO sheets (Appendix B9). Figure 4.11a exhibits the graphs of specific capacitance of Pt decorated graphene-based structures as a function of scan rates. Capacitance values of spheres, foam and fibers decreased gradually as the current rate increased. The specific capacitances of Pt decorated graphene-based structures at a scan rate of 1 mV/s were calculated as 118 F/g for spheres, 54 F/g for foam, and 8 F/g for fibers. An increase in capacitance values of hybrid electrodes when compared to neat TEGO-based electrodes stem from the diffusion of PAN polymer chains through graphene layers during electrospinning since PAN can serve as a spacer by preventing re-stacking of sheets and increase the electron mobility. In addition, Pt decorated TEGO showed poor capacitance behavior when it was utilized without using as a polymer carrier due to the sheet-sheet junctions that limit the conductivity and thus capacitance [183]. Another reason of low capacitance performance is the intercalation of Pt through layers and this decreases the catalytic activity of Pt particles. Afterwards, graphene sheets were converted into 1D fibers, the structure started to show capacitance activity but still has low value as about 8 F/g since electrospinning process buried Pt particles deeply inside the structure and hence electrochemical reaction was not observed effectively [184]. Figure 4.11b represents CV curves of graphene-based fibers at scan rates of 1, 5, 10, 50, and 100 mV/s where the capacitance value was calculated based on the lowest scan rate. Pt decorated graphene-based foam and spheres as 3D structures showed enhanced specific capacitance of 54 F/g and 118 F/g, respectively in comparison of 1D fibers. The CV plots of Pt decorated graphene-based foam are shown in Figure 4.11c. 3D graphene structures consist of micro and macro interconnected pores which results in a high surface area and fast ion/electron transport channels [106]. However, the diameter of Pt nanoparticles is considerably high as about 50 nm and thus the electrochemical activity of Pt decorated graphene-based foam decreased. Therefore, Pt decorated graphene-based foam although its unique structure did not show better capacitance behavior. In case of sphere electrode, Pt particle size decreased down to 5 nm and the structure became more porous as seen in SEM image of Figure 4.7c and thus electrode/electrolyte interface was improved and catalytic activity

increased in Figure 4.11d. As a result, Pt decorated graphene sphere electrode exhibited higher capacitance behavior due to its uniform structure since the morphologies of fiber and foam become more complex after carbonization process. Pt decorated graphene-based structures at low scan rates showed an approximately rectangular shape, which is the characteristic of an electric double layer capacitor. However, the rectangular shape started to distort by increasing the scan rate up to 100 mV/s. This comes from an increase in the polarization intensity and kinetically limited penetration of the electrolyte ions into pores of active materials at high scan rates [185].
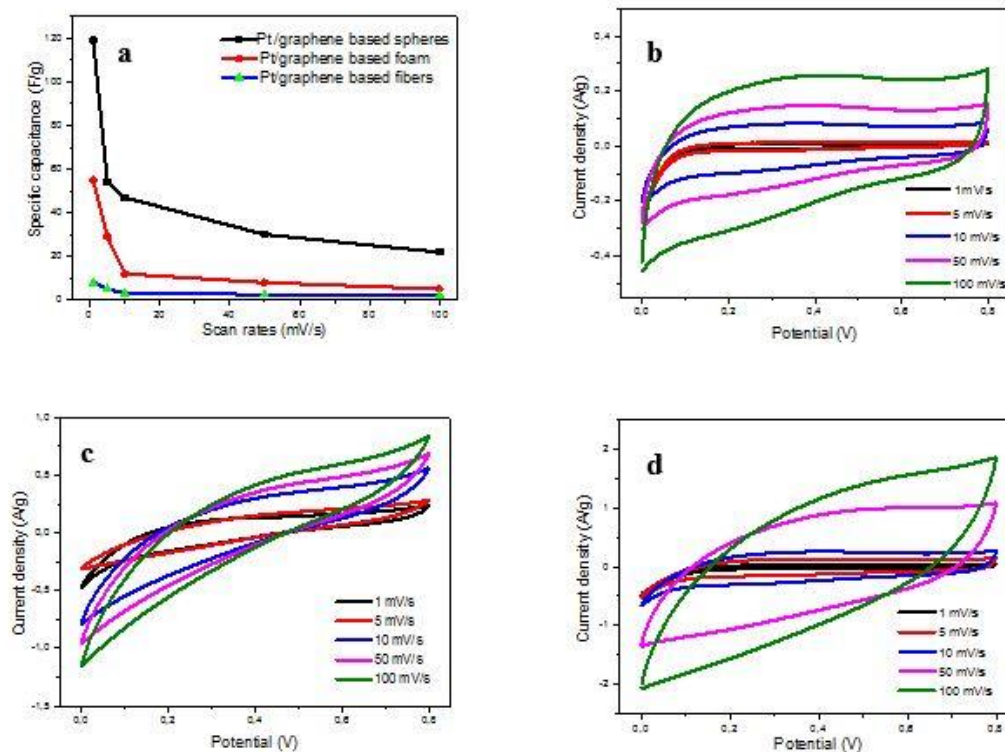
Figure 4.11 (**a**) Specific capacitance of Pt decorated graphene-based structures at different scan rates, CVs of Pt decorated graphene-based structures at different scan rates; (**b**) fibers, (**c**) foam, and (**d**) sphere electrodes

Table 4.2 CV results of Pt decorated graphene-based spheres, foam and fiber electrodes

Different dimensional electrodes	Specific capacitance (F/g) at a scan rate of 1 mV/s
Pt/TEGO	ND*
Pt/Spheres	118
Pt/Foam	54
Pt/Fibers	8

*ND: Not detected

The galvanostatic charge-discharge measurements were carried out in a 0.5 M H_2SO_4 electrolyte between 0 and 0.8 V at various current densities ranging from 2 to 10 A/g. The representative charge-discharge curves of Pt decorated graphene-based structures at a current density of 2 A/g are presented in Figure 4.12a. Pt decorated graphene-based structures showed nearly triangular shape, which is a behavior of electric double-layer capacitance electrodes [186]. On the other hand, Pt decorated graphene-based spheres showed a much longer discharge time at the same current density when compared to other structures. This indicates higher specific capacitance, which is also confirmed by CV results of graphene-based spheres. In practical electrodes, long-term cycling stability of electrodes is one of the critical parameters. In the present work, the cycling stability test was carried out under the current density of 5 A/g for 1000 cycles of charging-discharging. In Figure 4.12b, specific capacitance of Pt decorated graphene-based spheres decreased about 12% after 1000 cycles of charge-discharge whereas the values of Pt decorated graphene-based foam and fibers decreased 6% and 10%, respectively. The slight decrease in the cycle stability of spheres stem from a rapid shrinking of pores of spheres due to its 3D nature that results in a decrease in the capacitance as time passes which is in the agreement with coulombic efficiency results given in Appendix B10. Consequently, 1D and 3D graphene-based structures showed comparably higher cycling stability when compared to the other reported values in the literature [106], [187].
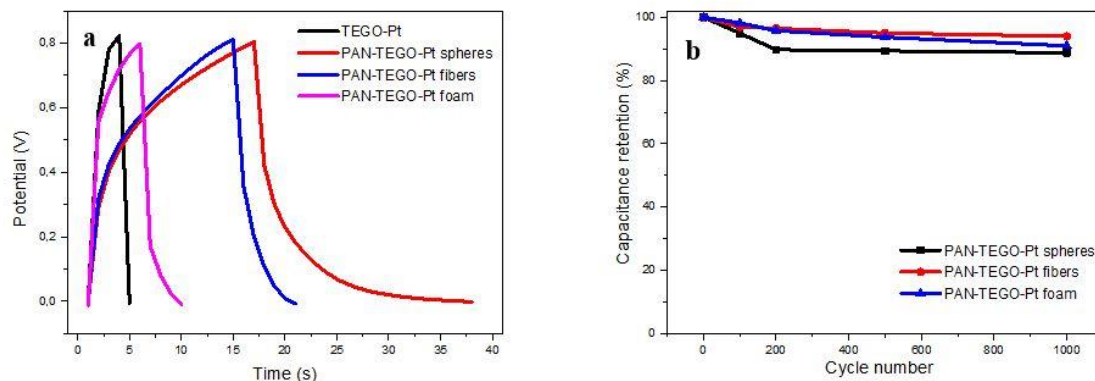
Figure 4.12 **(a)** Galvanostatic charge-discharge curves of Pt decorated graphene-based structures at a current density of 2 A/g, and **(b)** cycling stability of Pt decorated graphene-based structures upon charging-discharging at a current density of 5 A/g.

4.4 Conclusions

In the present work, Pt decorated graphene-based structures with different dimension and morphologies were successfully fabricated by core-shell electrospraying/electrospinning technology. Graphene foam was produced by electrospinning for the first time instead of CVD technique. PAN polymer was used as a carrier polymer to improve the carbon network and decrease the sheet-sheet junction of graphene sheets and thus enhance capacitance values. Pt were used as a catalyst to improve the catalytic activity of electrodes during CV analysis. Electric field during electrospraying/electrospinning enhanced the diffusion of polymer chains through graphene layers and provided better dispersion by converting graphene sheets into 1D fibers and 3D foam and spheres. The structural morphology was tailored by changing the molecular weight of PAN and polymer concentration in the electrospun solution and adjusting applied voltage during electrospinning. The relation between molecular weight of PAN and polymer concnetration on the formation of different structures was investigated by using Mark–Houwink–Sakurada equations in which, the obtained data was consistent with the experimental results. Structural properties of 1D and 3D structures were confirmed by FTIR and Raman spectroscopy. Electrochemical results showed that neat Pt/TEGO electrode did not show any capacitance behavior whereas the integration of TEGO sheets into 1D fibers and 3D foam and spherical structures in carbon network

74

improved capacitance characteristics. Specifically, a high capacitance was obtained from 3D graphene-based spheres having 118 F/g at a scan rate of 1 mV/s due to the homogeneous decoration of Pt particles with a diameter of 4 nm on the surface after post-treatment. After carbonization process, foam and fiber structures lost their uniformity, and graphene exfoliation and destruction in the structure and agglomeration of Pt particles caused to decrease their electrochemical performance. Therefore, the size and place of Pt particles are needed to be controlled for to get higher catalytic activity. After 1000 cycle of charging-discharging, Pt deposited graphene-based structures exhibited high cyclic stability and retention of capacitance due to the deposition of Pt particles into electrode structure. Consequently, core-shell electrospinning technology provided to adjust the dimension of structures by the embedment of graphene sheets and preventing agglomeration of graphene sheets by applying electric field to electrospun solutions. Especially this study brings a new insight for the fabrication of high performance electrode materials for energy storage devices.

CHAPTER 5 FREE-STANDING HIERARCHICAL HYBRID ELECTRODES BASED ON PANI COATED Mn₃O₄/GRAPHENE EMBEDDED CARBON FIBERS FOR HIGH PERFORMANCE SUPERCAPACITORS

5.1 Introduction

Supercapacitors, also known as ultracapacitors, are considered as one of the promising energy storage devices which offer long cyclic life, high power density and safe operation [188], [189]. According to energy storing mechanisms, supercapacitors are divided into two common groups, which are pseudo-capacitors and electrochemical double layer capacitors (EDLCs). Pseudo-capacitors such as transition metal oxides and conducting polymers store the charges *via* fast chemical redox reactions on their surface [190] and thus exhibit high theoretical capacitance. In the last years, manganese oxide, a typical metal oxide, has been considered as a promising pseudo-capacitor due to the high theoretical specific capacitance, low cost, and environmental friendly nature [12]. Besides, electrically conductive polyaniline (PANI) has been widely studied owing to its high electrical conductivity, fast redox rate and high theoretical specific capacitance [189]. On the other hand, EDLCs store the energy by reversible physical adsorption of ions without any chemical reactions [40]. Compared with pseudo-capacitors, EDLCs suffer from low energy density and poor capacitance [191]. To solve this problem and improve the electrochemical performance, pseudo-capacitors can be integrated into EDLCs by fabricating a hybrid structure and thus fully utilize the advantages of each component in the combined system.

Recently, graphene-based supercapacitors have attracted significant attention for EDLCs and other energy storage devices due to its fast electron mobility and high electrical conductivity [106]. Especially the design of ternary hybrid electrodes as novel hierarchical structures can effectively boost the electrochemical performance [192]–[194]. For instance, Wu *et al.* [195] fabricated a high performance supercapacitor based on ternary composite of manganese dioxide nanorods and graphene nanoribbons embedded in PANI matrix by two-step *in-situ* polymerization method and obtained a high specific capacitance of 472 F/g at a current density of 1 A/g and a cyclic stability of 79.7% after

5000 cycles. In another study, Huang and co-workers [196] investigated the electrochemical properties of reduced graphene oxide/manganese oxide/PANI composite electrodes by using potassium permanganate ($KMnO_4$) as manganese oxide source and also initiating agent for the polymerization of aniline followed by the hydrothermal method. This synthesized composite having fiber-like structures showed a high specific capacitance of 344 F/g and capacitance retention of nearly 100% after 6000 cycle of charging-discharging. Consequently, hydrothermal approach and wet chemistry method are mostly used to synthesize manganese oxide/graphene/polyaniline hybrid composites in the literature.

In particular, the deposition of manganese oxide on the surface of graphene is achieved through redox deposition by using oxidizing agents such as $KMnO_4$ but this kind of a strong agent can dramatically change the nature of the composites during the fabrication process [11]. Additionally, all of the aforementioned techniques are time-consuming and need many post-treatment processes and harmful chemicals. At this point, there is a tendency for the development of alternative approaches for the integration of manganese oxide on the graphene. Very recently, our group reported the design and fabrication of graphene-based hybrid composites in an easy and controllable manner *via* core-shell electrospinning [197]. With this technique, it is possible to integrate different functional nanoparticles and polymers and thus utilize hybrid materials with improved performance. Moreover, electrospun graphene-based fibers with their interconnected mesoporous texture provides a platform for the post-synthesis and integration of various *in-situ* materials like PANI into the fiber structure [11].

In this study, we reported a facile and straightforward route for the fabrication of hierarchical PANI coated graphene and manganese oxide embedded in carbon fibers (CF) *via* core-shell electrospinning. Polyacrylonitrile (PAN) polymer was selected as a carrier to increase the interconnections in fiber network and also carbon content. In addition, $KMnO_4$ was replaced by mild manganese (II) chloride tetrahydrate, which can oxidize to manganese oxide during heat treatment. In order to fully understand the effect of graphene on the structure and electrochemical performance of electrodes, two different types of

graphene including thermally exfoliated graphene oxide (TEGO) and graphene nanoplatelet (GNP) were selected based on the number of graphene layers. In order to increase the conductivity, the surfaces of these new design composite electrodes were also coated by PANI via *in-situ* polymerization of aniline monomer for the production of supercapacitor electrodes. Structural and morphological properties of composite electrodes were analyzed by spectroscopic and microscopic techniques in detail.

5.2 Experimental

5.2.1 Materials

The following materials have been used for the experiments: polyacrylonitrile (PAN, Mw: 150000 g/mol, Sigma-Aldrich), N, N-dimethyl formamide (DMF, Sigma-Aldrich, 99%), aniline (Sigma-Aldrich, 99.5%), ammonium persulfate (APS, Sigma, 98%), manganese (II) chloride tetrahydrate (Sigma-Aldrich, 99.99%), sulfuric acid (H_2SO_4, Sigma-Aldrich, 98%). Thermally exfoliated graphene oxide (TEGO) and graphene nano platelet (GNP) were purchased from NANOGRAFEN Co., Turkey. TEGO contains 27 graphene layers and 2.1 wt% oxygen content and its surface area is about 11 m^2/g. GNP has single plates with the length of 50 nm having 8.1 wt% oxygen functional groups and its surface area is around 85 m^2/g. The densities of TEGO and GNP are 1.05 g/cm^3 and 2.30 g/cm^3, respectively.

5.2.2 Preparation of Mn_3O_4/graphene embedded carbon fibers by core-shell electrospinning

Mn_3O_4/graphene-based fibers were fabricated by using tri-axial electrospinning equipment purchased from Yflow Company and converted into carbon fibers (CF) by applying heat treatment. For the fabrication of Mn_3O_4/TEGO-CF, 0.03 wt% TEGO and 1 wt% $MnCl_2$ were dispersed in DMF by sonicating the mixture for 15 min. PAN polymer with a concentration of 5 wt% was then poured into the sonicated dispersion followed by stirring for 1 day in order to attain homogeneous and stable mixtures. In the case of Mn_3O_4/GNP-CF, 0.5 wt% GNP and 1 wt% $MnCl_2$ were sonicated in DMF solvent and then 5 wt% PAN polymer was added into the mixture and stirred for 1 day. The

electrospinning process was performed with an applied voltage of 12 kV, flow rate of 9 µL/min with the nozzle to collector distance of 10 cm while atmospheric air was used as core material. For two different graphene solutions, electrospinning parameters were kept same. The amount of graphene used in electrospun solutions was dependent on the density of graphene and thus TEGO was adjusted as 0.03 wt% due to its comparably lower density than GNP. Finally, Mn_3O_4/TEGO-CF and Mn_3O_4/GNP-CF were obtained by performing heat treatment where $MnCl_2$ was oxidized to Mn_3O_4 and PAN was carbonized. During heat treatment, fibers were stabilized by applying oxidation process up to 300˚C under air for 2 h and then heated up to 800˚C for 2 h under argon atmosphere.

5.2.3 Fabrication of PANI@Mn₃O₄/graphene carbon fibers

PANI polymer was coated on the surface of fabricated fibers by *in-situ* chemical polymerization of aniline monomer in the presence of ammonium persulfate (APS) as the initiator. Briefly, Mn_3O_4/graphene-CF were immersed in 50 mL of 1 M H_2SO_4 aqueous solution containing 0.5 mL of aniline monomer. In the following, 0.5 g of APS was dispersed in 20 mL distilled water and then added dropwise to the aniline containing acid solution. The mixture was stirred at about 0˚C for 2 h followed by the filtration and washing process with ethanol and distilled water. Finally, the obtained composite samples were kept at 60 ˚C in oven for drying.

5.2.4 Electrode preparation and their electrochemical tests

Electrochemical performances of the produced composite electrodes were evaluated by PARSTAT MC (Princeton Applied Research) under a three-electrode system in 1 M H_2SO_4 aqueous electrolyte using platinum wire as a counter electrode and Ag/AgCl as a reference electrode in the potential range of 0-0.8 V. PANI@Mn_3O_4/graphene-CF samples were directly used as free-standing working electrodes without using any binder in electrochemical tests.

5.2.5 Characterization

The morphologies of fabricated structures were analyzed by Leo Supra 35VP field emission Scanning Electron Microscopy (SEM). X-ray diffraction (XRD) measurements were carried out by using a Bruker D2 PHASER desktop diffractometer with a CuKα radiation source. Raman spectroscopy was used to identify the surface characteristics of composite samples by using a Renishaw inVia Reflex Raman Microscopy System with the laser wavelength of 532 nm at room temperature in the range of 100-3500 cm^{-1}. The functional groups in the produced structures were determined by Netzsch Fourier Transform Infrared Spectroscopy (FTIR).

5.3 Results and discussion

5.3.1 Structural characterization and morphological investigation of PANI@Mn$_3$O$_4$/graphene-based electrodes

The fabrication procedure of PANI coated Mn$_3$O$_4$/graphene-based electrodes is illustrated in Figure 5.1. Firstly, PAN/MnCl$_2$ solution containing two different graphene sources of GNP and TEGO were electrospun separately. During electrospinning process, electrospun solution comes up against a high electric field, which stretches the polymeric droplet at the tip of the nozzle and thus initiates a continuous fiber formation on an electrically grounded plate [197]. Figure 5.2a and Figure 5.3a represent SEM images of electrospun PAN/MnCl$_2$/TEGO and PAN/MnCl$_2$/GNP fibers with an average diameter of 200 nm and 270 nm, respectively. Both of electrospun fibers formed continuous network without beads. The heat treatment of electrospun fibers was applied in two steps of stabilization of fibers under air up to 300˚C and carbonization of PAN polymer under argon atmosphere up to 800˚C. The oxidation of MnCl$_2$ particles into Mn$_3$O$_4$ started at around 180˚C under air atmosphere and continued until 300˚C [198]. The growth of Mn$_3$O$_4$ particles during heat treatment on the surface of Mn$_3$O$_4$/TEGO-CF and MN$_3$O$_4$/GNP-CF is shown in Figure 5.2b and Figure 5.3b, respectively. After oxidation process, Mn based particles has started to grow in cubical form but densely sticked to each other in fiber structure. Also, elemental analysis revealed that the percentage of manganese in the TEGO-based fibers increased from 5.5 wt% up to 73.5 wt% given in Table **5.1**. In

comparison of electrospun PAN/MnCl$_2$/TEGO with Mn$_3$O$_4$/TEGO-CF, Cl was completely eliminated after heat treatment indicating successful oxidation of manganese. A similar trend was also observed for GNP based electrospun and CF fibers. At the final step, PANI as conductive polymer was deposited on the surface of fibers by *in-situ* chemical polymerization method. The presence of oxygen functional groups on the surface of both GNP and TEGO facilitates the polymerization of PANI and provide homogeneous coating since these functional groups are acting as anchor sites by attaching to the aniline monomer [195]. After polymerization, the percentage of nitrogen on the surface of PANI@Mn$_3$O$_4$/TEGO-CF and PANI@Mn$_3$O$_4$/GNP-CF increased from 1.5 wt% up to 19 wt% and 18.5 wt%, respectively which supported the formation of PANI on the surface of composites. Figure 5.2c and Figure 5.3c shows SEM images of PANI coated Mn$_3$O$_4$/TEGO-CF and Mn$_3$O$_4$/GNP-CF, respectively. Needle-like PANI-based nanowires were observed on the surface of both types of carbon fibers.
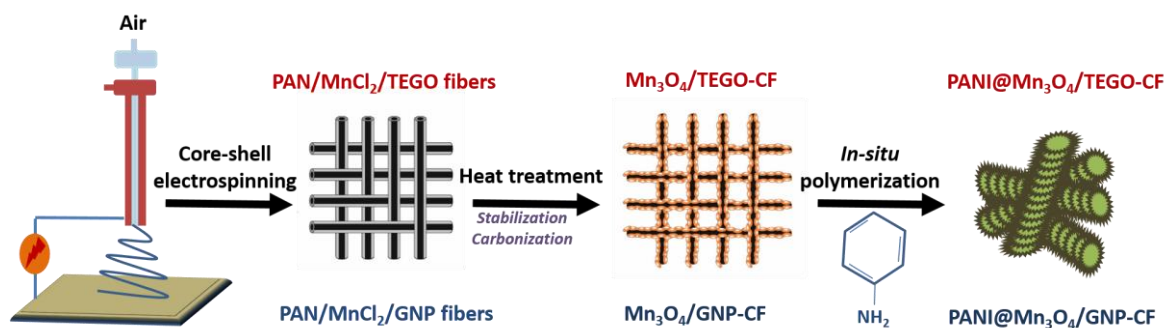
Figure 5.1 Schematic representation of synthesis procedure of PANI coated Mn$_3$O$_4$/graphene-based electrodes.
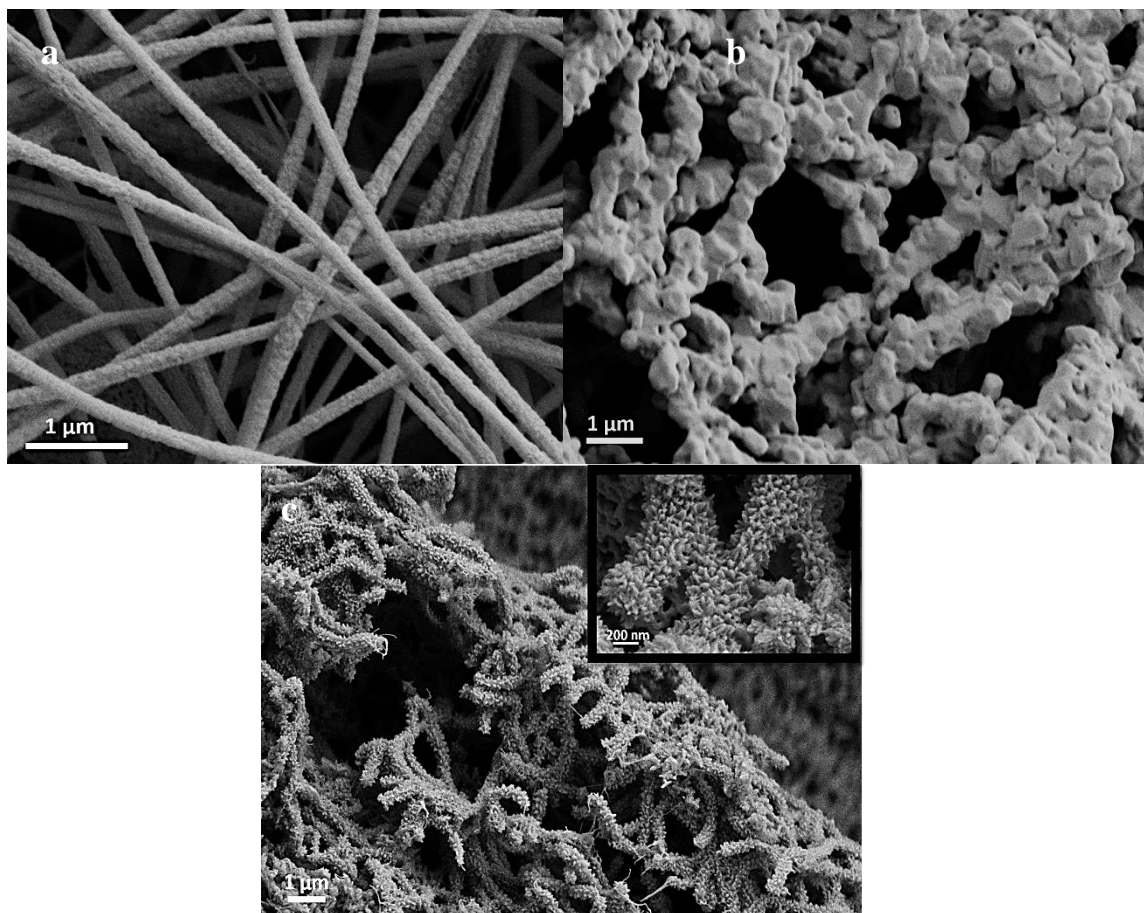
Figure 5.2 SEM images of **(a)** electrospun PAN/MnCl$_2$/TEGO fibers, **(b)** Mn$_3$O$_4$/TEGO-CF, and **(c)** PANI@Mn$_3$O$_4$/TEGO-CF
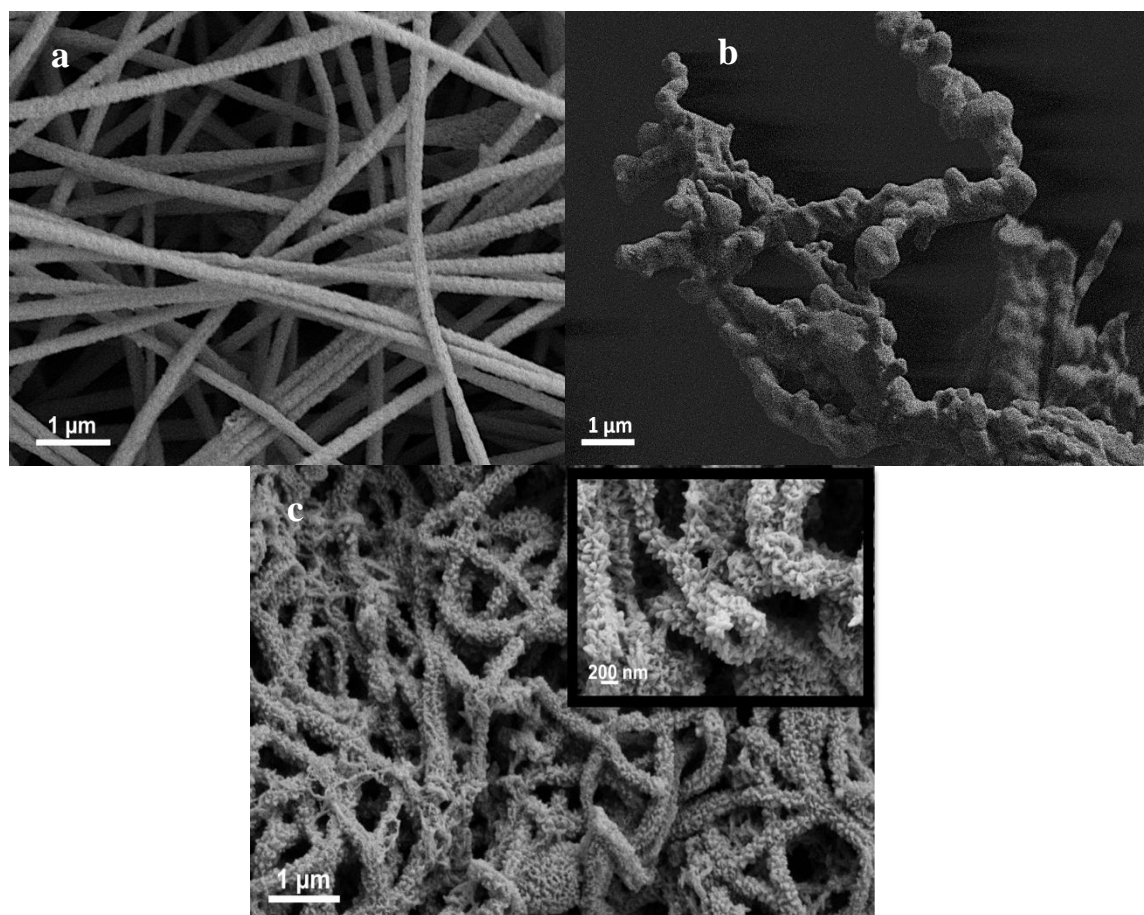
Figure 5.3 SEM images of **(a)** electrospun PAN/MnCl$_2$/GNP fibers, **(b)** Mn$_3$O$_4$/GNP-CF, and **(c)** PANI@Mn$_3$O$_4$/GNP-CF

Table 5.1 Elemental analysis of PANI@Mn$_3$O$_4$/graphene based hybrid composites

Samples	C (wt%)	O (wt%)	N (wt%)	Mn (wt%)	Cl (wt%)
Electrospun PAN/MnCl$_2$/TEGO	46	8.5	34.5	5.5	5.5
Mn$_3$O$_4$/TEGO-CF	4	21	1.5	73.5	-
PANI@Mn$_3$O$_4$/TEGO-CF	53	27	19	1	-
Electrospun PAN/MnCl$_2$/GNP	47.5	6	35	5.5	6
Mn$_3$O$_4$/GNP-CF	10	16.5	1.5	72	-
PANI@Mn$_3$O$_4$/GNP-CF	45.5	35	18.5	1	-

XRD characterization was performed to investigate the structural changes in the produced fibers in step-wise process and results are given in Figure 5.4. Electrospun samples has a broad characteristic peak at $2\Theta=16.5°$ associated to 100 plane of PAN polymer [161]. A sharp peak at $2\Theta=26°$ belongs to the 200 graphitic plane of both TEGO and GNP [8]. In Figure 5.4a, small reflection peaks at $2\Theta=15.5°$, $20°$ and $31°$ indicate the presence of manganese chloride hydrate in the electrospun fiber structure (PDF 25-1043). After carbonization, a typical crystalline pattern of tetragonal hausmannite Mn_3O_4 (PDF 80-0382) is observed in both XRD spectra of Mn_3O_4/TEGO-CF and Mn_3O_4/GNP-CF. Also, the reflection peaks at $2\Theta=26°$ is also attributed to the 200 graphitic plane of TEGO and GNP. In Figure 5.4b, an additional carbon peak is seen at $2\Theta=45°$ corresponding to 100 carbon plane of Mn_3O_4/GNP-CF [199]. However, carbon peaks are not dominant in the XRD spectrum of Mn_3O_4/TEGO-CF due to much lower TEGO content in fiber structure. In the last process by PANI coating, there is a broad XRD peak appeared at $2\Theta=23°$ attributed to the emeraldine salt form of PANI [194]. Therefore, XRD supported successful and homogeneous deposition of PANI on the surface of fibers by suppressing the characteristic peaks of other components in the structure.
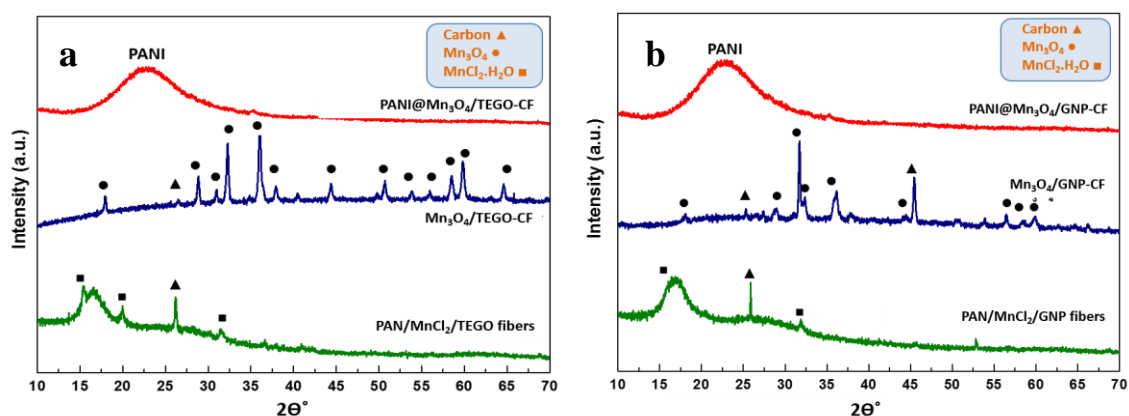
Figure 5.4 XRD spectra of electrospun, carbonized and PANI coated composite fibers having **(a)** TEGO and **(b)** GNP

In order to further understand the structural changes of composites, FTIR spectral analysis was conducted after each production step. In the FTIR spectrum of electrospun PAN/MnCl$_2$/TEGO in Figure 5.5a, the bands at 2930 cm^{-1}, 2243 cm^{-1}, 1452 cm^{-1} are

attributed to the C–H bonds in CH_2, nitrile bond (C≡N), and tensile vibration of CH_2 of PAN polymer, respectively[8]. A peak at 1631 cm^{-1} is related to the C=C aromatic vibration of TEGO [192]. Moreover, O-H vibration at 3375 cm^{-1} corresponds to the $MnCl_2.H_2O$ in the electrospun fiber. It is not possible to see Mn-Cl stretching bands in the present spectrum since these bands appear in the IR regions of 300-200 cm^{-1} [200]. After carbonization, characteristic PAN peaks disappeared in the FTIR spectrum of Mn_3O_4/TEGO-CF meaning the successful cyclization and dehydrogenation[8]. A sharp peak at 595 cm^{-1} is assigned to Mn-O stretching vibration band of Mn_3O_4 [192]. After PANI deposition, new structure has C=C stretching vibrations of quinoid and benzoid rings in the emeraldine salt at 1565 cm^{-1} and 1473 cm^{-1} [71], C-N stretching of the secondary aromatic amine at 1281 cm^{-1} [201], and C-H bending at 781 cm^{-1} [71]. The bands in the region of 1000-1150 cm^{-1} is related to the bending vibration of C-H mode [194]. A decrease in the intensity of Mn-O stretching vibration of Mn_3O_4 at 591 cm^{-1} indicates that ternary hybrid is fully covered by PANI polymer. A similar trend was also observed for GNP-based composites shown in Figure 5.5b.
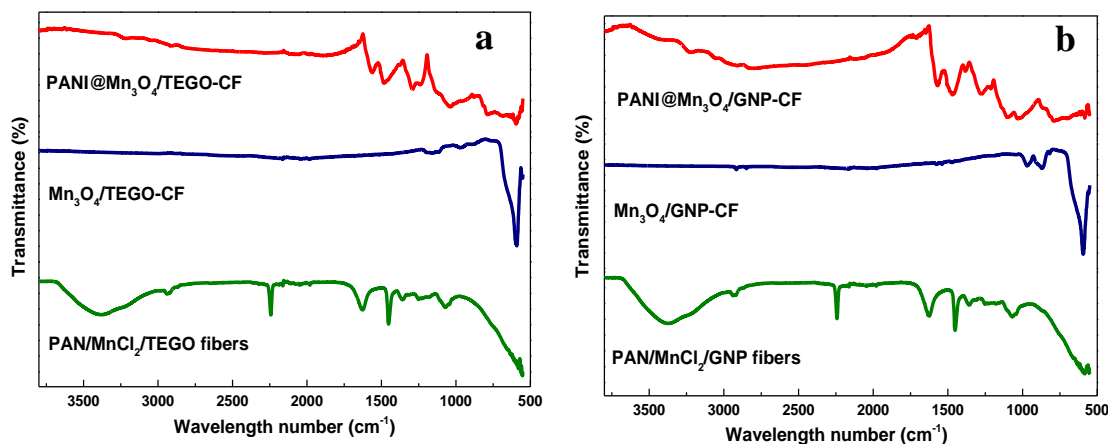
Figure 5.5 FTIR spectra of electrospun, carbonized and PANI coated composite fibers having **(a)** TEGO and **(b)** GNP

In addition to FTIR characterization, Raman spectroscopy was also conducted to confirm the existence of graphene in the composite fibers. Typical D and G bands of graphene-based materials are seen at 1356 cm^{-1} and 1578 cm^{-1} in Figure 5.6. In the Raman

spectra of ternary hybrid fibers, there is a slight shift in the peak position of D band due to the π-π* interactions between aniline monomer with TEGO and GNP [201]. It is well known that D band is related to the disorderness and intensity ratio of D and G bands (I_D/I_G) is changed by the alteration of structures [202]. I_D/I_G values of electrospun PAN/MnCl$_2$/TEGO and PAN/MnCl$_2$/GLS were calculated as 1.01 and 1.44, respectively. Whereby, after heat treatment process, the values decreased down to 0.97 and 0.99, respectively. This stems from the rearrangement of the structures in a more ordered manner and an increase in the crystallinity due to the formation of highly crystalline Mn$_3$O$_4$ phase. The peak at 645 cm^{-1} is attributed to the symmetric stretching vibration of Mn-O [203] whereby the intensity of this peak significantly increased after heat treatment and this verifies the successful oxidation of manganese during heat treatment. Also, this peak is shifted to the left after PANI decoration owing to the H-bonding interactions between Mn$_3$O$_4$, graphene, and PANI together [204], [205]. Moreover, PANI@Mn$_3$O$_4$/TEGO-CF and PANI@Mn$_3$O$_4$/GNP-CF hybrids have additional peaks at 1157 cm^{-1} corresponding to the aromatic C-H in-plane bending of benzoid ring [71], 1399 cm^{-1} attributed to C-N$^+$ stretching [206], 1529 cm^{-1} due to the stretching vibrations of C=N of emeraldine base [207], and 1648 cm^{-1} related to the C-C stretching of the benzenoid ring [206]. Consequently, spectroscopic analyses were justifed the creation of carbon network, the existence of graphene layers and the phase changes in manganese based catalyst.
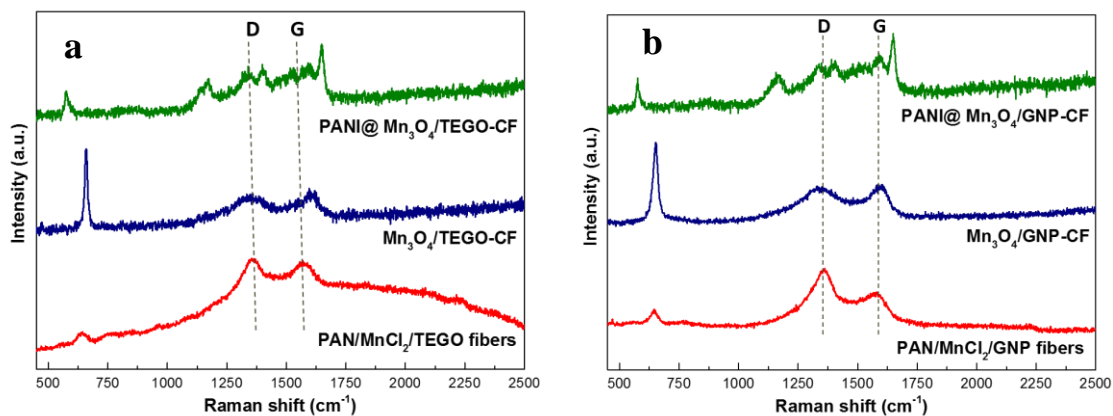
Figure 5.6 Raman spectra of PANI@Mn$_3$O$_4$/graphene based composites by the addition of **(a)** TEGO and **(b)** GNP.

5.3.2 Electrochemical performance of PANI coated Mn$_3$O$_4$/graphene CF electrodes

Cyclic voltammetry (CV) analysis was carried out to examine the electrochemical behavior of PANI@Mn$_3$O$_4$ TEGO-CF and PANI@Mn$_3$O$_4$/GNP-CF composite electrodes in 1 M H$_2$SO$_4$. In Figure 5.7a and Figure 5.7b, all the CV curves of both GNP and TEGO based ternary hybrids are close to rectangular shape without any redox peaks. Especially GNP based electrodes is more like an ideal EDLC when compared to one having TEGO at the rate of 1 mV/s as seen in Figure 5.7d. The absence of Faradaic peaks in CV curve of a hybrid composite which contains pseudo-capacitor components like manganese oxide and PANI is attributed to effective interactions of redox active sites together and thus easy electron transfer in a wide range of potentials [208].

The specific capacitance of electrodes based on the CV tests (C$_{cv}$) was calculated by the following equation

$$C_{cv} = IdV/(2m\vartheta\Delta V) \tag{1}$$

where C$_{cv}$ is the specific capacitance (F/g), I is the current (A), m is the weight of active materials (g), ϑ is the scan rate (V/s), and ΔV is the potential window (V). Table **5.2** summarizes the specific capacitance values of the produced electrodes. Specific capacitance values of PANI@Mn$_3$O$_4$/TEGO-CF at different scan rates of 1, 5, and 10 mV were calculated as 326, 100, and 63 F/g, respectively. Typically, by increasing the scan rate, the specific capacitance value started to decrease due to the kinetically limited penetration of electrolyte ions. In the case of PANI@Mn$_3$O$_4$/TEGO-CF, by increasing the scan rate up to 20 mV/s, a sharp decrease of capacitance to 20% of its initial value was observed which designates that PANI@Mn$_3$O$_4$/TEGO-CF have poor rate capability (Figure 5.7c). Despite the high specific capacitance, CV of PANI@Mn$_3$O$_4$/TEGO-CF exhibited quasi-reversibility behavior since the charge stored under the positive current is much higher than that of negative current. This might come from the polarization and

ohmic resistance during faradaic process of manganese oxide. In case of irreversible behaviors, the specific capacitance calculated from CV would not show the actual capacitance activity of the electrode [208]. In Figure 5.7b, PANI@Mn$_3$O$_4$/GNP-CF with the almost symmetrical and reversible CV curves, showed specific capacitance values of 452, 262, and 190 F/g at scan rates of 1, 5, and 10 mV/s, respectively. By increasing the scan rate, the specific capacitance retained at about 45% of its initial value at 10 mV/s. Higher specific capacitance value of GNP-based hybrid compared to TEGO-based electrode arises from higher content of GNP in the structure which facilitates the synergistic effects between PANI and graphene layers by improving both electrode-electrolyte interactions and interfacial interactions between all components in the structure and shorten the diffusion lengths of ions [201].

Table 5.2 CV results of PANI@Mn$_3$O$_4$/TEGO-CF and PANI@Mn$_3$O$_4$/GNP-CF at different scan rates

	1 mV/s	5 mV/s	10 mV/s
PANI@Mn$_3$O$_4$/TEGO-CF	326	100	63
PANI@Mn$_3$O$_4$/GNP-CF	452	262	190
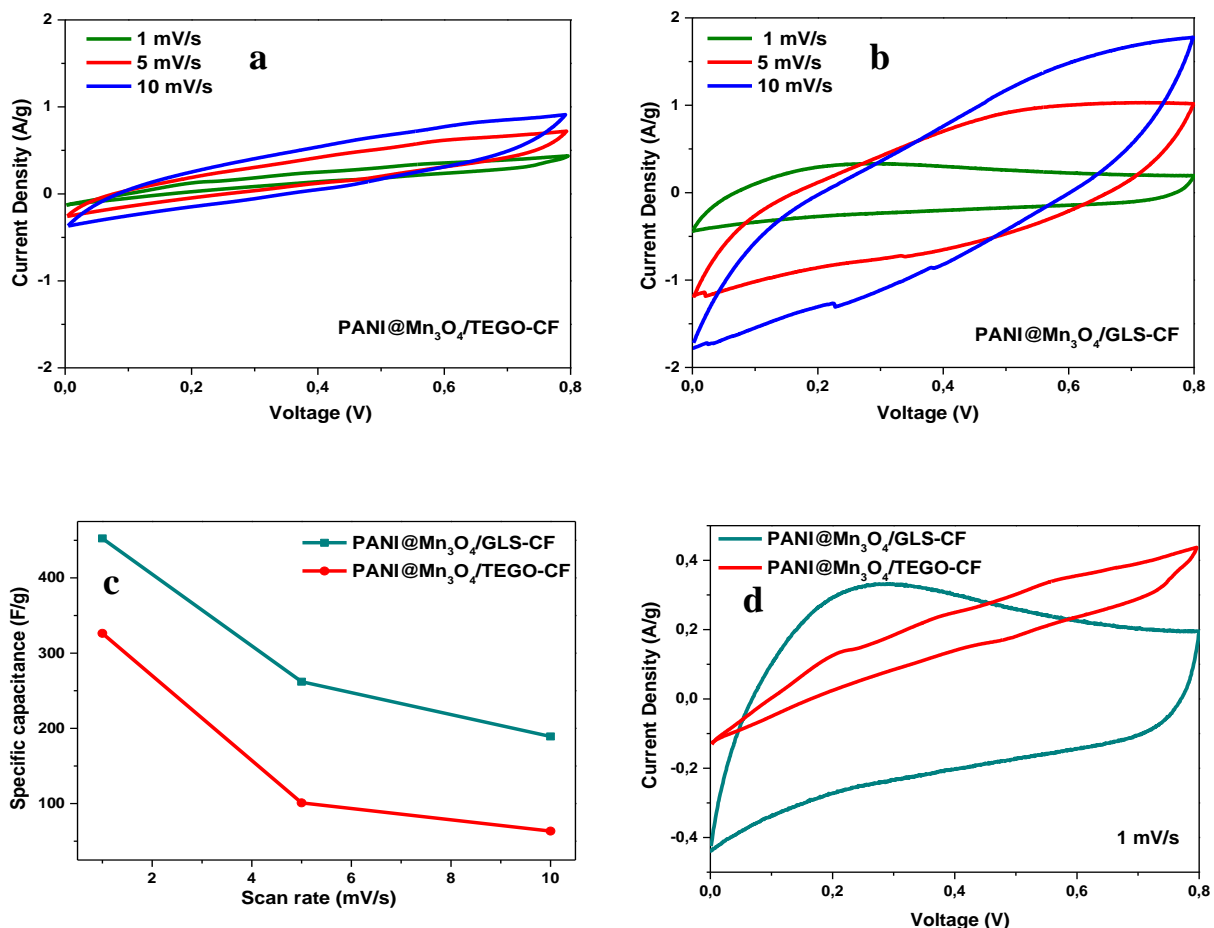
Figure 5.7 CV curves of (a) PANI@Mn$_3$O$_4$/TEGO-CF, (b) PANI@Mn$_3$O$_4$/GNP-CF at different scan rates of 1, 5, and 10 mV/s, (c) specific capacitance of PANI@Mn$_3$O$_4$/TEGO-CF and PANI@Mn$_3$O$_4$/GNP-CF at different scan rates and (d) comparison of electrochemical performance of electrodes at 1 mV/s

The galvanostatic charge-discharge test (GCD) was performed to further evaluate the electrochemical performance of fabricated electrodes. The GCD plots of both electrodes exhibit almost triangular shapes shown in Figure 5.8a and Figure 5.8b. However, in the case of PANI@Mn$_3$O$_4$/TEGO-CF electrode, there is a nonlinearity with longer charging time rather than discharging time which is a reflection of quasi-reversible electrode reaction [208]. During charging process, the irreversible electrochemical polarization fasten the faradaic reduction of manganese oxide into soluble manganese ions in electrolyte and thus decrease the discharging time [209].

The cycling stability of the samples was carried out under a current density of 1 A/g for 1000 cycles of charging-discharging shown in Figure 5.8c. PANI@Mn$_3$O$_4$/TEGO-CF and PANI@Mn$_3$O$_4$/GLS-CF exhibited 66% and 89% retention of capacitance. A relatively poor capacitance retention of PANI@Mn$_3$O$_4$/TEGO-CF is related to the low content of graphene inside the structure leading to the fast degradation of pseudocapacitive components. Also, TEGO has multi-layer structure and it forms intercalated structure during electrospining whereas GNP contains single platelets and this causes exfoliated structure. Therefore, different dispersion state based on material properties directly affects the electrochemical performance and single platelet graphene seems more advantageous rather than multi-layer graphene due to its large surface area and high surface oxygen functional groups that strenghten the interfacial interactions between polymer matrix and catalyst.
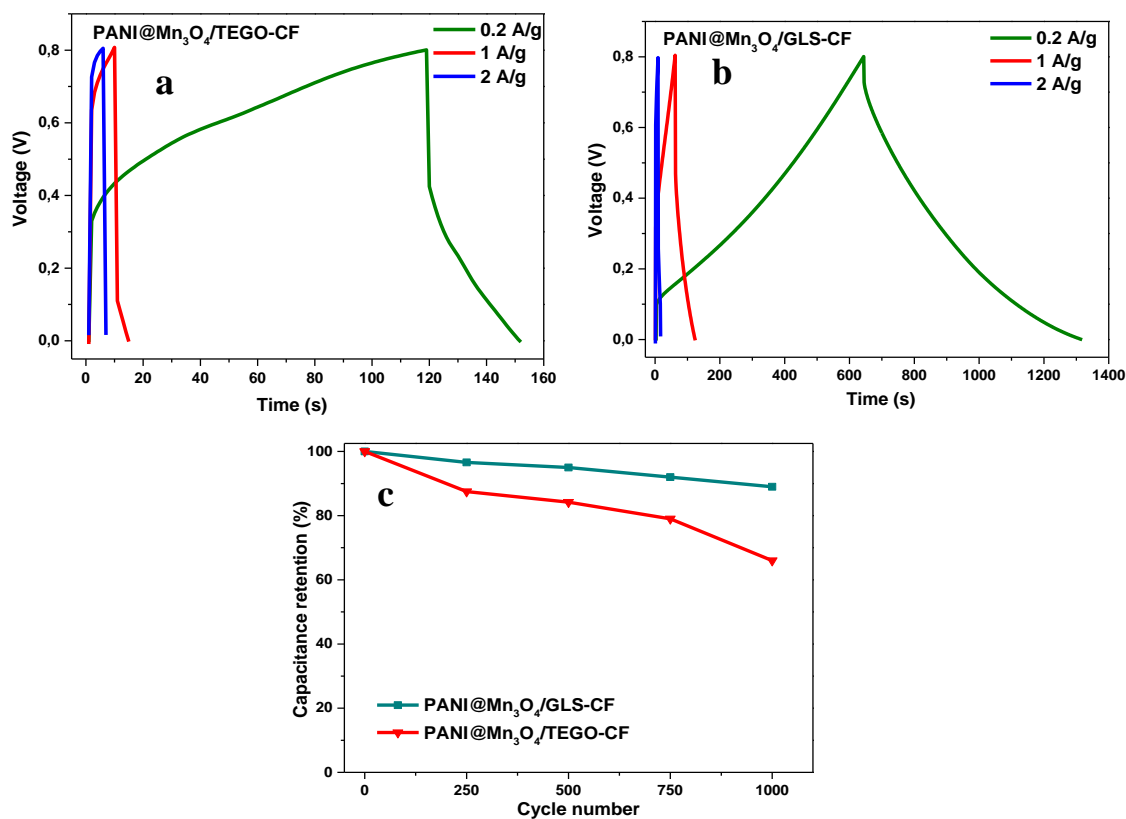
Figure 5.8 GCD curves of **(a)** PANI@Mn_3O_4/TEGO-CF, **(b)** PANI@Mn_3O_4/GNP-CF at current densities of 0.2, 1, and 2 A/g, and **(c)** cycling stability of upon charging-discharging at a current density of 1 A/g.

5.4 Conclusions

In the present work, a series of PANI coated Mn_3O_4/graphene embedded carbon fibers with different graphene sources were synthesized through core-shell electrospinning, carbonization and *in-situ* polymerization techniques. Multi-layer graphene and single platelets graphene were incorporated into the fiber structure and the effect of number of graphene layers on the electrochemical performance of electrodes was investigated by CV and GCD tests. The spectroscopy analysis confirmed the strong interactions between the components of ternary hybrid composites. PANI coated Mn_3O_4/GNP-CF exhibited a high specific capacitance of 452 F/g at a scan rate of 1 mV/s and 89% capacitance retention after 1000 cycle of charging-discharging. The introduction of graphene single platelets into the fiber structure facilitated both ion and electron transport and provided highly electroactive sites and shortened the diffusion paths by bridging the adjacent individual PANI chains. Additionally, relatively high oxygen functional groups of GNP enhanced the interfacial interactions between electrode components. On the other hand, PANI coated Mn_3O_4/TEGO-CF showed a specific capacitance of 326 F/g at a scan rate of 1 mV/s with poor cycling stability of 66% after 1000 cycles of charge-discharge at a current density of 0.2 A/g. Low content of graphene in the structure of PANI@Mn_3O_4/TEGO-CF caused a rapid polarization of manganese oxide ions and thus irreversible reactions during charge-discharge fastened the degradation of electrode. Consequently, the number of graphene layers, its surface oxygen functional groups as well as its dispersion state greatly affected the electrochemical performance of supercapacitor electrodes and these complex designed ternary hybrid electrodes bring a new insight in fabrication of high performance energy storage devices.

CHAPTER 6 **CONCLUSIONS**

This study was conducted in three major sections. The findings for each step can be summarized as follows:

1) *Design and fabrication of hollow and filled graphene-based polymeric spheres via core-shell electrospraying:*

Firstly, the effect of electric field on the exfoliation process of graphene sheets during electrospraying was investigated in details. Electrospraying prevents the agglomeration of graphene sheets by enhancing the intercalation of polymeric chains into graphene sheets. Raman analysis showed that electrosprayed graphene preserves its multi-layer nature.

In the next step, three-different types of polymers were used as spacers between the graphene sheets by converting the 2D structure to different graphene-based architectures. The proper polymer concentration for the formation of spherical particles was investigated by using the Mark-Houwink-Sakurada equations. Three types of electrospun solutions with different polymers were prepared and electrosprayed separately. The hollowness of spheres was controlled by changing core solvent. Consequently, by tailoring process parameters like voltage and flow rate and appropriate polymer concentration, graphene-based polymeric spheres with desirable size and hollowness opens up new directions especially in energy applications such as Li-ion batteries, fuel cells, and supercapacitors.

2) *Design of Pt-supported 1D and 3D multilayer graphene-based structural composite electrodes with controlled morphology by core-shell electrospinning/electrospraying*

In this part of study, three different forms of Pt-decorated graphene based structures with controlled dimensionality were successfully fabricated through core-shell electrospraying/electrospinning approach. The proper polymer concentration for the formation of three different structures of sphere, fibers, and foam was determined by using Mark-Houwink-Sakurada equations. PAN polymer was used as a carrier during electrospinning whereby, after applying heat treatment it carbonized to carbon. Platinum was used as catalyst in order to increase the catalytic activity of composites. The

morphology and structural properties of composites were investigated *via* microscopic and spectroscopic characterization techniques. Moreover, the electrochemical performance of Pt-decorated graphene-based spheres, fibers, and foam was investigated through CV and GCD methods. Among the three different electrodes, Pt-supported 3D graphene-based spheres showed the highest specific capacitance of 118 F/g at a scan rate of 1 mV/s owing to the homogeneous decoration of Pt particles with a small diameter of 4 nm on the surface. After 1000 cycles of charging-discharging, Pt-decorated graphene-based structures showed high cyclic stability, indicating their potential as high-performance electrodes for energy storage devices.

3) *Free-standing hierarchical hybrid electrodes based on PANI coated Mn_3O_4/graphene embedded carbon fibers for high performance supercapacitors*

In this study, a facile and straightforward route for the fabrication of hierarchical PANI coated graphene and manganese oxide embedded in carbon fibers (CF) *via* core-shell electrospinning has been reported. $MnCl_2$ was used as manganese source, whereby during heat treatment of PAN polymer, it oxidized to manganese oxide. Moreover, multi-layer graphene and single platelets graphene were incorporated into the fiber structure separately and the effect of number of graphene layers on the electrochemical performance of electrodes was investigated by CV and GCD tests. PANI coated Mn_3O_4/GNP-CF exhibited a high specific capacitance of 452 F/g at a scan rate of 1 mV/s and 89% capacitance retention after 1000 cycle of charging-discharging. The introduction of graphene single platelets into the fiber structure facilitated both ion and electron transport, provided highly electroactive sites, and shortened the diffusion paths by bridging the adjacent individual PANI chains. Consequently, the number of graphene layers, its surface oxygen functional groups as well as its dispersion state greatly affected the electrochemical performance of supercapacitor electrodes. Besides high electrochemical performance, low manufacturing cost and processability are the main factors for the utilization of these fabricated electrodes in the industrial applications. Especially use of graphene obtained from waste sources would severely lower the cost of production.

Consequently, low cost and multi-functionalized graphene-based hybrid materials become promising candidates in the energy storage devices.

In the future studies, the content of Mn_3O_4 in the structure will be optimized and the interaction of PANI chains with graphene sheets will be improved by tailoring the synthesis parameters in order to decrease the degradation period of hybrid electrodes. In addition to fibers, Mn_3O_4 and polyaniline will be integrated into the graphene-based spheres and foam to attain high surface area and porous structure through core-shell electrospraying technique.

BIBLIOGRAPHY

[1]   X. Du, I. Skachko, A. Barker, and E. Y. Andrei, "Approaching ballistic transport in suspended graphene," *Nat. Nanotechnol.*, vol. 3, no. 8, pp. 491–495, Aug. 2008.

[2]   A. A. Balandin, S. Ghosh, W. Bao, I. Calizo, D. Teweldebrhan, F. Miao, and C. N. Lau, "Superior Thermal Conductivity of Single-Layer Graphene," *Nano Lett.*, vol. 8, no. 3, pp. 902–907, Mar. 2008.

[3]   Y. Zhu, S. Murali, W. Cai, X. Li, J. W. Suk, J. R. Potts, and R. S. Ruoff, "Graphene and graphene oxide: Synthesis, properties, and applications," *Adv. Mater.*, vol. 22, no. 35, pp. 3906–3924, 2010.

[4]   A. E. Galashev and O. R. Rakhmanova, "Mechanical and thermal stability of graphene and graphene-based materials," *Physics-Uspekhi*, vol. 57, no. 10, pp. 970–989, 2014.

[5]   C. Lee, X. Wei, J. W. Kysar, and J. Hone, "Measurement of the Elastic Properties and Intrinsic Strength of Monolayer Graphene," *Science (80-.).*, vol. 321, no. 5887, pp. 385–388, Jul. 2008.

[6]   S. Mao, G. Lu, and J. Chen, "Three-dimensional graphene-based composites for energy applications," *Nanoscale*, 2014.

[7]   Y. Zhao, C. Jiang, C. Hu, Z. Dong, J. Xue, Y. Meng, N. Zheng, P. Chen, and L. Qu, "Large-scale spinning assembly of neat, morphology-defined, graphene-based hollow fibers," *ACS Nano*, vol. 7, no. 3, pp. 2406–2412, 2013.

[8]   L. Haghighi Poudeh, B. Saner Okan, J. Seyyed Monfared Zanjani, M. Yildiz, and Y. Z. Menceloglu, "Design and Fabrication of Hollow and Filled Graphene-based Polymeric Spheres via Core-Shell Electrospraying," *RSC Adv.*, vol. 5, pp. 91147–91157, 2015.

[9]   K. M. Forward, A. Flores, and G. C. Rutledge, "Production of core/shell fibers by electrospinning from a free surface," *Chem. Eng. Sci.*, vol. 104, pp. 250–259, Dec. 2013.

[10]   J. S. M. Zanjani, B. Saner Okan, Y. Z. Menceloglu, and M. Yildiz, "Design and fabrication of multi-walled hollow nanofibers by triaxial electrospinning as reinforcing agents in nanocomposites," *J. Reinf. Plast. Compos. *, vol. 34, no. 16, pp. 1273–1286, Aug. 2015.

[11]   L. Lim, Y. Liu, W. Liu, R. Tjandra, L. Rasenthiram, Z. Chen, and A. Yu, "All-in-One Graphene Based Composite Fiber: Toward Wearable Supercapacitor," *ACS Appl. Mater. Interfaces*, vol. 9, no. 45, pp. 39576–39583, 2017.

[12]   Z. Wang, Q. Qin, W. Xu, J. Yan, and Y. Wu, "Long Cyclic Life in Manganese Oxide-Based Electrodes," *ACS Appl. Mater. Interfaces*, vol. 8, no. 28, pp. 18078–18088, 2016.

[13]   K. S. Novoselov, A. K. Geim, S. V. Morozov, D. Jiang, Y. Zhang, S. V. Dubonos, I. V. Grigorieva, and A. A. Firsov, "Electric field effect in atomically thin carbon films.," *Science (80-.).*, vol. 306, no. 5696, pp. 666–669, 2004.

[14] P. W. Sutter, J.-I. Flege, and E. A. Sutter, "Epitaxial graphene on ruthenium," *Nat. Mater.*, vol. 7, no. 5, pp. 406–411, May 2008.

[15] K. S. Kim, Y. Zhao, H. Jang, S. Y. Lee, J. M. Kim, K. S. Kim, J.-H. Ahn, P. Kim, J.-Y. Choi, and B. H. Hong, "Large-scale pattern growth of graphene films for stretchable transparent electrodes," *Nature*, vol. 457, no. 7230, pp. 706–710, Feb. 2009.

[16] J. Lu, J. Yang, J. Wang, A. Lim, S. Wang, and K. P. Loh, "One-Pot Synthesis of Fluorescent Carbon Nanoribbons, Nanoparticles, and Graphene by the Exfoliation of Graphite in Ionic Liquids," *ACS Nano*, vol. 3, no. 8, pp. 2367–2375, Aug. 2009.

[17] S. Stankovich, D. a. Dikin, R. D. Piner, K. a. Kohlhaas, A. Kleinhammes, Y. Jia, Y. Wu, S. T. Nguyen, and R. S. Ruoff, "Synthesis of graphene-based nanosheets via chemical reduction of exfoliated graphite oxide," *Carbon N. Y.*, vol. 45, pp. 1558–1565, 2007.

[18] S. Park and R. S. Ruoff, "Chemical methods for the production of graphenes.," *Nat. Nanotechnol.*, vol. 4, no. march, pp. 217–224, 2009.

[19] C. Li and G. Shi, "Three-dimensional graphene architectures," *Nanoscale*, vol. 4, no. 18, p. 5549, 2012.

[20] D. R. Dreyer, S. Park, C. W. Bielawski, and R. S. Ruoff, "The chemistry of graphene oxide," *Chem. Soc. Rev.*, vol. 39, no. 1, pp. 228–240, 2010.

[21] M. Khan, M. N. Tahir, S. F. Adil, H. U. Khan, M. R. H. Siddiqui, A. A. Al-warthan, and W. Tremel, "Graphene based metal and metal oxide nanocomposites: synthesis, properties and their applications," *J. Mater. Chem. A*, vol. 3, no. 37, pp. 18753–18808, 2015.

[22] B. C. Brodie, "On the Atomic Weight of Graphite," *Phil. Trans. R. Soc. Lond.*, vol. 149, no. January, pp. 249–259, 1859.

[23] L. Staudenmaier, "Verfahren zur Darstellung der Graphitsaure," *Ber Dtsch Chem Ges*, vol. 31, pp. 1481–1487, 1898.

[24] J. William S. Hummers and R. E. Offeman, "Preparation of Graphitic Oxide," *J. Am. Chem. Soc*, vol. 80, no. 1937, p. 1339, 1958.

[25] J. Chen, B. Yao, C. Li, and G. Shi, "An improved Hummers method for eco-friendly synthesis of graphene oxide," *Carbon N. Y.*, vol. 64, no. 1, pp. 225–229, 2013.

[26] D. C. Marcano, D. V. Kosynkin, J. M. Berlin, A. Sinitskii, Z. Sun, A. Slesarev, L. B. Alemany, W. Lu, and J. M. Tour, "Improved synthesis of graphene oxide," *ACS Nano*, vol. 4, no. 8, pp. 4806–4814, 2010.

[27] B. Saner, F. Okyay, and Y. Yürüm, "Utilization of multiple graphene layers in fuel cells. 1. An improved technique for the exfoliation of graphene-based nanosheets from graphite," *Fuel*, vol. 89, no. 8, pp. 1903–1910, 2010.

[28] M. J. McAllister, J.-L. Li, D. H. Adamson, H. C. Schniepp, A. A. Abdala, J. Liu, M. Herrera-Alonso, D. L. Milius, R. Car, R. K. Prud'homme, and I. A. Aksay, "Single Sheet Functionalized Graphene by Oxidation and Thermal Expansion of Graphite," *Chem. Mater.*, vol. 19, no. 18, pp. 4396–4404, Sep. 2007.

[29] S. Stankovich, D. A. Dikin, R. D. Piner, K. A. Kohlhaas, A. Kleinhammes, Y. Jia, Y. Wu, S. T. Nguyen, and R. S. Ruoff, "Synthesis of graphene-based nanosheets via chemical reduction of exfoliated graphite oxide," *Carbon N. Y.*, vol. 45, no. 7, pp. 1558–1565, Jun. 2007.

[30] B. Saner, F. Dinç, and Y. Yürüm, "Utilization of multiple graphene nanosheets in fuel cells: 2. the effect of oxidation process on the characteristics of graphene nanosheets," *Fuel*, vol. 90, no. 8, pp. 2609–2616, 2011.

[31] Y. Si and E. T. Samulski, "Synthesis of water soluble graphene," *Nano Lett.*, vol. 8, pp. 1679–82, 2008.

[32] Y. Xu, K. Sheng, C. Li, and G. Shi, "Self-Assembled Graphene Hydrogel via a One-Step Hydrothermal Process," *ACS Nano*, vol. 4, no. 7, pp. 4324–4330, Jul. 2010.

[33] J. Kim, L. J. Cote, F. Kim, W. Yuan, K. R. Shull, and J. Huang, "Graphene Oxide Sheets at Interfaces," *J. Am. Chem. Soc.*, vol. 132, no. 23, pp. 8180–8186, Jun. 2010.

[34] H. Bai, C. Li, X. Wang, and G. Shi, "On the gelation of graphene oxide," *J. Phys. Chem. C*, vol. 115, no. 13, pp. 5545–5551, 2011.

[35] V. H. Luan, H. N. Tien, L. T. Hoa, N. T. M. Hien, E.-S. Oh, J. Chung, E. J. Kim, W. M. Choi, B.-S. Kong, and S. H. Hur, "Synthesis of a highly conductive and large surface area graphene oxide hydrogel and its use in a supercapacitor," *J. Mater. Chem. A*, vol. 1, no. 2, pp. 208–211, 2013.

[36] D. Wang, R. Kou, D. Choi, Z. Yang, Z. Nie, J. Li, L. V. Saraf, D. Hu, J. Zhang, G. L. Graff, J. Liu, M. A. Pope, and I. A. Aksay, "Ternary Self-Assembly of Ordered Metal Oxide−Graphene Nanocomposites for Electrochemical Energy Storage," *ACS Nano*, vol. 4, no. 3, pp. 1587–1595, Mar. 2010.

[37] A. J. Patil, J. L. Vickery, T. B. Scott, and S. Mann, "Aqueous Stabilization and Self-Assembly of Graphene Sheets into Layered Bio-Nanocomposites using DNA," *Adv. Mater.*, vol. 21, no. 31, pp. 3159–3164, Aug. 2009.

[38] G. Eda and M. Chhowalla, "Chemically Derived Graphene Oxide: Towards Large-Area Thin-Film Electronics and Optoelectronics," *Adv. Mater.*, vol. 22, no. 22, pp. 2392–2415, Jun. 2010.

[39] M. Zeng, W. L. Wang, and X. D. Bai, "Preparing three-dimensional graphene architectures: Review of recent developments," *Chinese Phys. B*, vol. 22, no. 9, 2013.

[40] X. Cao, Z. Yin, and H. Zhang, "Three-dimensional graphene materials: preparation,

structures and application in supercapacitors," *Energy Environ. Sci.*, vol. 7, p. 1850, 2014.

[41]   X. Ji, X. Zhang, and X. Zhang, "Three-Dimensional Graphene-Based Nanomaterials as Electrocatalysts for Oxygen Reduction Reaction," *J. Nanomater.*, vol. 2015, pp. 1–9, 2015.

[42]   O. C. Compton, Z. An, K. W. Putz, B. J. Hong, B. G. Hauser, L. Catherine Brinson, and S. T. Nguyen, "Additive-free hydrogelation of graphene oxide by ultrasonication," *Carbon N. Y.*, vol. 50, no. 10, pp. 3399–3406, Aug. 2012.

[43]   H. Bai, C. Li, X. Wang, and G. Shi, "A pH-sensitive graphene oxide composite hydrogel," *Chem. Commun.*, vol. 46, no. 14, p. 2376, 2010.

[44]   Y. Xu, Q. Wu, Y. Sun, H. Bai, and G. Shi, "Three-Dimensional Self-Assembly of Graphene Oxide and DNA into Multifunctional Hydrogels," *ACS Nano*, vol. 4, no. 12, pp. 7358–7362, Dec. 2010.

[45]   H. P. Cong, X. C. Ren, P. Wang, and S. H. Yu, "Macroscopic multifunctional graphene-based hydrogels and aerogels by a metal ion induced self-assembly process," *ACS Nano*, vol. 6, no. 3, pp. 2693–2703, 2012.

[46]   W. Chen, S. Li, C. Chen, and L. Yan, "Self-Assembly and Embedding of Nanoparticles by In Situ Reduced Graphene for Preparation of a 3D Graphene/Nanoparticle Aerogel," *Adv. Mater.*, vol. 23, no. 47, pp. 5679–5683, Dec. 2011.

[47]   G. He, H. Tang, H. Wang, and Z. Bian, "Highly Selective and Active Pd-In/three-dimensional Graphene with Special Structure for Electroreduction CO_2 to Formate," *Electroanalysis*, pp. 1–11, 2017.

[48]   Y. Ma and Y. Chen, "Three-dimensional graphene networks: synthesis, properties and applications," *Natl. Sci. Rev.*, vol. 2, pp. 40–53, 2014.

[49]   X. Xie, Y. Zhou, H. Bi, K. Yin, S. Wan, and L. Sun, "Large-range control of the microstructures and properties of three-dimensional porous graphene," *Sci. Rep.*, vol. 3, pp. 1–6, 2013.

[50]   K. Sheng, Y. Sun, C. Li, W. Yuan, and G. Shi, "Ultrahigh-rate supercapacitors based on eletrochemically reduced graphene oxide for ac line-filtering," *Sci. Rep.*, vol. 2, no. 1, p. 247, Dec. 2012.

[51]   K. Chen, L. Chen, Y. Chen, H. Bai, and L. Li, "Three-dimensional porous graphene-based composite materials: electrochemical synthesis and application," *J. Mater. Chem.*, vol. 22, no. 39, p. 20968, 2012.

[52]   J. Zhang, Y. Yu, L. Liu, and Y. Wu, "Graphene-hollow PPy sphere 3D-nanoarchitecture with enhanced electrochemical performance.," *Nanoscale*, vol. 5, no. 7, pp. 3052–7, 2013.

[53]   D. Cai, L. Ding, S. Wang, Z. Li, M. Zhu, and H. Wang, "Facile synthesis of ultrathin-shell graphene hollow spheres for high-performance lithium-ion batteries," *Electrochim. Acta*,

vol. 139, pp. 96–103, 2014.

[54]   Q. Shao, J. Tang, Y. Lin, F. Zhang, J. Yuan, H. Zhang, N. Shinya, and L.-C. Qin, "Synthesis and characterization of graphene hollow spheres for application in supercapacitors," *J. Mater. Chem. A*, vol. 1, pp. 15423–15428, 2013.

[55]   L. Wu, H. Feng, M. Liu, K. Zhang, and J. Li, "Graphene-based hollow spheres as efficient electrocatalysts for oxygen reduction.," *Nanoscale*, vol. 5, pp. 10839–43, 2013.

[56]   X. Huang, K. Qian, J. Yang, J. Zhang, L. Li, C. Yu, and D. Zhao, "Functional nanoporous graphene foams with controlled pore sizes," *Adv. Mater.*, vol. 24, no. 32, pp. 4419–4423, 2012.

[57]   J. Seyyed Monfared Zanjani, B. Saner Okan, I. Letofsky-Papst, M. Yildiz, and Y. Z. Menceloglu, "Rational design and direct fabrication of multi-walled hollow electrospun fibers with controllable structure and surface properties," *Eur. Polym. J.*, vol. 62, pp. 66–76, 2015.

[58]   S. Shilpa, B. M. Basavaraja, S. B. Majumder, and A. Sharma, "Electrospun hollow glassy carbon–reduced graphene oxide nanofibers with encapsulated ZnO nanoparticles: a free standing anode for Li-ion batteries," *J. Mater. Chem. A*, vol. 3, no. 10, pp. 5344–5351, 2015.

[59]   C.-J. Lin, C.-L. Liu, and W.-C. Chen, "Poly(3-hexylthiophene)/Graphene Composites based Aligned Nanofibers for High Performance Field Effect Transistors," *J. Mater. Chem. C*, 2015.

[60]   N. Promphet, P. Rattanarat, R. Rangkupan, O. Chailapakul, and N. Rodthongkum, "An electrochemical sensor based on graphene/polyaniline/polystyrene nanoporous fibers modified electrode for simultaneous determination of lead and cadmium," *Sensors Actuators B Chem.*, vol. 207, pp. 526–534, Feb. 2015.

[61]   M. J. Allen, V. C. Tung, and R. B. Kaner, "Honeycomb carbon: A review of graphene," *Chem. Rev.*, vol. 110, no. 1, pp. 132–145, 2010.

[62]   Z. Chen, W. Ren, L. Gao, B. Liu, S. Pei, and H.-M. Cheng, "Three-dimensional flexible and conductive interconnected graphene networks grown by chemical vapour deposition.," *Nat. Mater.*, vol. 10, no. 6, pp. 424–428, 2011.

[63]   O. Bagoole, M. Rahman, H. Younes, S. Shah, and A. Al Ghaferi, "Three-Dimensional Graphene Interconnected Structure, Fabrication Methods and Applications: Review," *J. Nanomed. Nanotechnol.*, vol. 8, no. 2, 2017.

[64]   M. Zhou, T. Lin, F. Huang, Y. Zhong, Z. Wang, Y. Tang, H. Bi, D. Wan, and J. Lin, "Highly Conductive Porous Graphene/Ceramic Composites for Heat Transfer and Thermal Energy Storage," *Adv. Funct. Mater.*, vol. 23, no. 18, pp. 2263–2269, May 2013.

[65]   G. Ning, Z. Fan, G. Wang, J. Gao, W. Qian, and F. Wei, "Gram-scale synthesis of

nanomesh graphene with high surface area and its application in supercapacitor electrodes," *Chem. Commun.*, vol. 47, no. 21, p. 5976, 2011.

[66] W. Li, S. Gao, L. Wu, S. Qiu, Y. Guo, X. Geng, M. Chen, S. Liao, C. Zhu, Y. Gong, M. Long, J. Xu, X. Wei, M. Sun, and L. Liu, "High-Density Three-Dimension Graphene Macroscopic Objects for High-Capacity Removal of Heavy Metal Ions," *Sci. Rep.*, vol. 3, no. 1, p. 2125, Dec. 2013.

[67] J.-S. Lee, H.-J. Ahn, J.-C. Yoon, and J.-H. Jang, "Three-dimensional nano-foam of few-layer graphene grown by CVD for DSSC," *Phys. Chem. Chem. Phys.*, vol. 14, no. 22, p. 7938, 2012.

[68] Y. Ito, Y. Tanabe, H. J. Qiu, K. Sugawara, S. Heguri, N. H. Tu, K. K. Huynh, T. Fujita, T. Takahashi, K. Tanigaki, and M. Chen, "High-quality three-dimensional nanoporous graphene," *Angew. Chemie - Int. Ed.*, vol. 53, no. 19, pp. 4822–4826, 2014.

[69] S. Mao, K. Yu, J. Chang, D. A. Steeber, L. E. Ocola, and J. Chen, "Direct growth of vertically-oriented graphene for field-effect transistor biosensor," *Sci. Rep.*, vol. 3, pp. 33–36, 2013.

[70] H. Wang, L. Shi, T. Yan, J. Zhang, Q. Zhong, and D. Zhang, "Design of graphene-coated hollow mesoporous carbon spheres as high performance electrodes for capacitive deionization," *J. Mater. Chem. A*, vol. 2, pp. 4739–4750, 2014.

[71] J. Luo, Q. Ma, H. Gu, Y. Zheng, and X. Liu, "Three-dimensional graphene-polyaniline hybrid hollow spheres by layer-by-layer assembly for application in supercapacitor," *Electrochim. Acta*, vol. 173, pp. 184–192, 2015.

[72] S. Mao, Z. Wen, H. Kim, G. Lu, P. Hurley, and J. Chen, "A general approach to one-pot fabrication of crumpled graphene-based nanohybrids for energy applications," *ACS Nano*, vol. 6, no. 8, pp. 7505–7513, 2012.

[73] J. S. Lee, S. I. Kim, J. C. Yoon, and J. H. Jang, "Chemical vapor deposition of mesoporous graphene nanoballs for supercapacitor," *ACS Nano*, vol. 7, no. 7, pp. 6047–6055, 2013.

[74] X. Huang, K. Qian, J. Yang, J. Zhang, L. Li, C. Yu, and D. Zhao, "Functional Nanoporous Graphene Foams with Controlled Pore Sizes," *Adv. Mater.*, vol. 24, no. 32, pp. 4419–4423, Aug. 2012.

[75] H. S. Ahn, J. M. Kim, C. Park, J.-W. Jang, J. S. Lee, H. Kim, M. Kaviany, and M. H. Kim, "A Novel Role of Three Dimensional Graphene Foam to Prevent Heater Failure during Boiling," *Sci. Rep.*, vol. 3, no. 1, p. 1960, Dec. 2013.

[76] H. Gao, F. Xiao, C. B. Ching, and H. Duan, "High-Performance Asymmetric Supercapacitor Based on Graphene Hydrogel and Nanostructured MnO 2," *ACS Appl. Mater. Interfaces*, vol. 4, no. 5, pp. 2801–2810, May 2012.

[77] P. Chen, J.-J. Yang, S.-S. Li, Z. Wang, T.-Y. Xiao, Y.-H. Qian, and S.-H. Yu,

"Hydrothermal synthesis of macroscopic nitrogen-doped graphene hydrogels for ultrafast supercapacitor," *Nano Energy*, vol. 2, no. 2, pp. 249–256, Mar. 2013.

[78] Z. Han, Z. Tang, P. Li, G. Yang, Q. Zheng, and J. Yang, "Ammonia solution strengthened three-dimensional macro-porous graphene aerogel," *Nanoscale*, vol. 5, no. 12, p. 5462, 2013.

[79] H. Sun, Z. Xu, and C. Gao, "Multifunctional, Ultra-Flyweight, Synergistically Assembled Carbon Aerogels," *Adv. Mater.*, vol. 25, no. 18, pp. 2554–2560, May 2013.

[80] Z. Xu, Z. Li, C. M. B. Holt, X. Tan, H. Wang, B. S. Amirkhiz, T. Stephenson, and D. Mitlin, "Electrochemical Supercapacitor Electrodes from Sponge-like Graphene Nanoarchitectures with Ultrahigh Power Density," *J. Phys. Chem. Lett.*, vol. 3, no. 20, pp. 2928–2933, Oct. 2012.

[81] H.-B. Yao, J. Ge, C.-F. Wang, X. Wang, W. Hu, Z.-J. Zheng, Y. Ni, and S.-H. Yu, "A Flexible and Highly Pressure-Sensitive Graphene-Polyurethane Sponge Based on Fractured Microstructure Design," *Adv. Mater.*, vol. 25, no. 46, pp. 6692–6698, Dec. 2013.

[82] X. Cao, Y. Shi, W. Shi, G. Lu, X. Huang, Q. Yan, Q. Zhang, and H. Zhang, "Preparation of novel 3D graphene networks for supercapacitor applications," *Small*, vol. 7, no. 22, pp. 3163–3168, 2011.

[83] A. C. Ferrari, J. C. Meyer, V. Scardaci, C. Casiraghi, M. Lazzeri, F. Mauri, S. Piscanec, D. Jiang, K. S. Novoselov, S. Roth, and A. K. Geim, "Raman spectrum of graphene and graphene layers," *Phys. Rev. Lett.*, vol. 97, p. 187401, 2006.

[84] W. Li, S. Gao, L. Wu, S. Qiu, Y. Guo, X. Geng, M. Chen, S. Liao, C. Zhu, Y. Gong, M. Long, J. Xu, X. Wei, M. Sun, and L. Liu, "High-density three-dimension graphene macroscopic objects for high-capacity removal of heavy metal ions.," *Sci. Rep.*, vol. 3, p. 2125, 2013.

[85] Z. Y. Sui, Y. Cui, J. H. Zhu, and B. H. Han, "Preparation of Three-dimensional graphene oxide-polyethylenimine porous materials as dye and gas adsorbents," *ACS Appl. Mater. Interfaces*, vol. 5, no. 18, pp. 9172–9179, 2013.

[86] H. Bin Yao, J. Ge, C. F. Wang, X. Wang, W. Hu, Z. J. Zheng, Y. Ni, and S. H. Yu, "A flexible and highly pressure-sensitive graphene-polyurethane sponge based on fractured microstructure design," *Adv. Mater.*, vol. 25, no. 46, pp. 6692–6698, 2013.

[87] Y. Shao, M. F. El-Kady, C. W. Lin, G. Zhu, K. L. Marsh, J. Y. Hwang, Q. Zhang, Y. Li, H. Wang, and R. B. Kaner, "3D Freeze-Casting of Cellular Graphene Films for Ultrahigh-Power-Density Supercapacitors," *Adv. Mater.*, pp. 6719–6726, 2016.

[88] X. Yang, J. Zhu, L. Qiu, and D. Li, "Bioinspired effective prevention of restacking in multilayered graphene films: Towards the next generation of high-performance supercapacitors," *Adv. Mater.*, vol. 23, no. 25, pp. 2833–2838, 2011.

[89] Q. Wu, Y. Xu, Z. Yao, A. Liu, and G. Shi, "Supercapacitors Based on Flexible Graphene/Polyaniline Nanofiber Composite Films," *ACS Nano*, vol. 4, no. 4, pp. 1963–1970, 2010.

[90] C. Tan, X. Huang, and H. Zhang, "Synthesis and applications of graphene-based noble metal nanostructures," *Mater. Today*, vol. 16, no. 1–2, pp. 29–36, Jan. 2013.

[91] W. Shi, J. Zhu, D. H. Sim, Y. Y. Tay, Z. Lu, X. Zhang, Y. Sharma, M. Srinivasan, H. Zhang, H. H. Hng, and Q. Yan, "Achieving high specific charge capacitances in Fe3O4/reduced graphene oxide nanocomposites," *J. Mater. Chem.*, vol. 21, no. 10, p. 3422, 2011.

[92] Q. Cheng, J. Tang, N. Shinya, and L. C. Qin, "Co(OH)2nanosheet-decorated graphene-CNT composite for supercapacitors of high energy density," *Sci. Technol. Adv. Mater.*, vol. 15, no. 1, 2014.

[93] M. Li, Z. Tang, M. Leng, and J. Xue, "Flexible solid-state supercapacitor based on graphene-based hybrid films," *Adv. Funct. Mater.*, vol. 24, no. 47, pp. 7495–7502, 2014.

[94] M. Jahan, Q. Bao, and K. P. Loh, "Electrocatalytically Active Graphene − Porphyrin MOF Composite for Oxygen Reduction Reaction," *J. Am. Chem. Soc.*, vol. 134, no. 15, pp. 6707–6713, 2012.

[95] B. G. Choi, M. Yang, W. H. Hong, J. W. Choi, and Y. S. Huh, "3D macroporous graphene frameworks for supercapacitors with high energy and power densities," *ACS Nano*, vol. 6, no. 5, pp. 4020–4028, 2012.

[96] S. Korkut, J. D. Roy-Mayhew, D. M. Dabbs, D. L. Milius, and I. A. Aksay, "High Surface Area Tapes Produced with Functionalized Graphene," *ACS Nano*, vol. 5, no. 6, pp. 5214–5222, Jun. 2011.

[97] Z. Niu, J. Chen, H. H. Hng, J. Ma, and X. Chen, "A Leavening Strategy to Prepare Reduced Graphene Oxide Foams," *Adv. Mater.*, vol. 24, no. 30, pp. 4144–4150, Aug. 2012.

[98] M. F. El-Kady, V. Strong, S. Dubin, and R. B. Kaner, "Laser Scribing of High-Performance and Flexible Graphene-Based Electrochemical Capacitors," *Science (80-.).*, vol. 335, no. 6074, pp. 1326–1330, Mar. 2012.

[99] L. Zhang, F. Zhang, X. Yang, G. Long, Y. Wu, T. Zhang, K. Leng, Y. Huang, Y. Ma, A. Yu, and Y. Chen, "Porous 3D graphene-based bulk materials with exceptional high surface area and excellent conductivity for supercapacitors," *Sci. Rep.*, vol. 3, no. 1, p. 1408, Dec. 2013.

[100] Y. Zhang, P. Chen, X. Gao, B. Wang, H. Liu, H. Wu, H. Liu, and S. Dou, "Nitrogen-Doped Graphene Ribbon Assembled Core–Sheath MnO@Graphene Scrolls as Hierarchically Ordered 3D Porous Electrodes for Fast and Durable Lithium Storage," *Adv. Funct. Mater.*, vol. 26, no. 43, pp. 7754–7765, 2016.

[101] C. Hu, Y. Zhao, H. Cheng, Y. Wang, Z. Dong, C. Jiang, X. Zhai, L. Jiang, and L. Qu, "Graphene microtubings: Controlled fabrication and site-specific functionalization," *Nano Lett.*, vol. 12, pp. 5879–5884, 2012.

[102] X. Wei, Y. Li, W. Xu, K. Zhang, J. Yin, S. Shi, J. Wei, F. Di, J. Guo, C. Wang, C. Chu, N. Sui, B. Chen, Y. Zhang, H. Hao, X. Zhang, J. Zhao, H. Zhou, and S. Wang, "From two-dimensional graphene oxide to three-dimensional honeycomb-like Ni3S2@graphene oxide composite: Insight into structure and electrocatalytic properties," *R. Soc. Open Sci.*, vol. 4, no. 12, p. 171409, 2017.

[103] H. Wang, K. Sun, F. Tao, D. J. Stacchiola, and Y. H. Hu, "3D honeycomb-like structured graphene and its high efficiency as a counter-electrode catalyst for dye-sensitized solar cells," *Angew. Chemie - Int. Ed.*, vol. 52, no. 35, pp. 9210–9214, 2013.

[104] G. Wang, L. Zhang, and J. Zhang, "A review of electrode materials for electrochemical supercapacitors," *Chem. Soc. Rev.*, vol. 41, no. 2, pp. 797–828, 2012.

[105] A. G. Pandolfo and A. F. Hollenkamp, "Carbon properties and their role in supercapacitors," *J. Power Sources*, vol. 157, no. 1, pp. 11–27, 2006.

[106] Q. Ke and J. Wang, "Graphene-based Materials for Supercapacitor Electrodes - A Review," *J. Mater.*, vol. 2, no. 1, pp. 37–54, 2016.

[107] K. Qin, E. Liu, J. Li, J. Kang, C. Shi, C. He, F. He, and N. Zhao, "Free-Standing 3D Nanoporous Duct-Like and Hierarchical Nanoporous Graphene Films for Micron-Level Flexible Solid-State Asymmetric Supercapacitors," *Adv. Energy Mater.*, p. 1600755, 2016.

[108] W. Fan, Y. Y. Xia, W. W. Tjiu, P. K. Pallathadka, C. He, and T. Liu, "Nitrogen-doped graphene hollow nanospheres as novel electrode materials for supercapacitor applications," *J. Power Sources*, vol. 243, pp. 973–981, 2013.

[109] W. Fan, C. Zhang, W. W. Tjiu, K. P. Pramoda, C. He, and T. Liu, "Graphene-Wrapped Polyaniline Hollow Spheres As Novel Hybrid Electrode Materials for Supercapacitor Applications," *ACS Appl. Mater. Interfaces*, vol. 5, no. 8, pp. 3382–3391, Apr. 2013.

[110] Z. Yan, W. Yao, L. Hu, D. Liu, C. Wang, and C.-S. Lee, "Progress in the preparation and application of three-dimensional graphene-based porous nanocomposites," *Nanoscale*, vol. 7, no. 13, pp. 5563–5577, 2015.

[111] Y. Xu, Z. Lin, X. Huang, Y. Liu, Y. Huang, and X. Duan, "Flexible solid-state supercapacitors based on three-dimensional graphene hydrogel films," *ACS Nano*, vol. 7, no. 5, pp. 4042–4049, 2013.

[112] Y. He, W. Chen, X. Li, Z. Zhang, J. Fu, C. Zhao, and E. Xie, "Freestanding three-dimensional graphene/Mno2 composite networks as ultralight and flexible supercapacitor electrodes," *ACS Nano*, vol. 7, no. 1, pp. 174–182, 2013.

[113] C. Wang, Y. Li, Y.-S. Chui, Q.-H. Wu, X. Chen, and W. Zhang, "Three-dimensional Sn–

graphene anode for high-performance lithium-ion batteries," *Nanoscale*, vol. 5, no. 21, p. 10599, 2013.

[114] L. Chu, M. Li, Y. Wang, X. Li, Z. Wan, S. Dou, and Y. Chu, "Multishelled NiO Hollow Spheres Decorated by Graphene Nanosheets as Anodes for Lithium-Ion Batteries with Improved Reversible Capacity and Cycling Stability," *J. Nanomater.*, vol. 2016, 2016.

[115] J. Luo, J. Liu, Z. Zeng, C. F. Ng, L. Ma, H. Zhang, J. Lin, Z. Shen, and H. J. Fan, "Three-dimensional graphene foam supported Fe3O4 lithium battery anodes with long cycle life and high rate capability," *Nano Lett.*, vol. 13, no. 12, pp. 6136–6143, 2013.

[116] Y. Tang, F. Huang, H. Bi, Z. Liu, and D. Wan, "Highly conductive three-dimensional graphene for enhancing the rate performance of LiFePO 4 cathode," *J. Power Sources*, vol. 203, pp. 130–134, 2012.

[117] S. H. Bae, K. Karthikeyan, Y. S. Lee, and I. K. Oh, "Microwave self-assembly of 3D graphene-carbon nanotube-nickel nanostructure for high capacity anode material in lithium ion battery," *Carbon N. Y.*, vol. 64, pp. 527–536, 2013.

[118] S. X. Yu, L. W. Yang, Y. Tian, P. Yang, F. Jiang, S. W. Hu, X. L. Wei, and J. X. Zhong, "Mesoporous anatase TiO2 submicrospheres embedded in self-assembled three-dimensional reduced graphene oxide networks for enhanced lithium storage," *J. Mater. Chem. A*, vol. 1, no. 41, p. 12750, 2013.

[119] W. Yang, K. R. Ratinac, S. P. Ringer, P. Thordarson, J. J. Gooding, and F. Braet, "Carbon Nanomaterials in Biosensors: Should You Use Nanotubes or Graphene?," *Angew. Chemie Int. Ed.*, vol. 49, no. 12, pp. 2114–2138, Mar. 2010.

[120] F. Yavari, Z. Chen, A. V. Thomas, W. Ren, H. M. Cheng, and N. Koratkar, "High sensitivity gas detection using a macroscopic three-dimensional graphene foam network," *Sci. Rep.*, vol. 1, pp. 1–5, 2011.

[121] C. C. Kung, P. Y. Lin, F. J. Buse, Y. Xue, X. Yu, L. Dai, and C. C. Liu, "Preparation and characterization of three dimensional graphene foam supported platinum-ruthenium bimetallic nanocatalysts for hydrogen peroxide based electrochemical biosensors," *Biosens. Bioelectron.*, vol. 52, pp. 1–7, 2014.

[122] T. Yang, Q. Guan, Q. H. Li, L. Meng, L. L. Wang, C. X. Liu, and K. Jiao, "Large-area, three-dimensional interconnected graphene oxide intercalated with self-doped polyaniline nanofibers as a free-standing electrocatalytic platform for adenine and guanine," *J. Mater. Chem. B*, vol. 1, no. 23, pp. 2926–2933, 2013.

[123] H. Wang, G. Wang, Y. Ling, F. Qian, Y. Song, X. Lu, S. Chen, Y. Tong, and Y. Li, "High power density microbial fuel cell with flexible 3D graphene–nickel foam as anode," *Nanoscale*, vol. 5, no. 21, p. 10283, 2013.

[124] Y. C. Yong, X. C. Dong, M. B. Chan-Park, H. Song, and P. Chen, "Macroporous and monolithic anode based on polyaniline hybridized three-dimensional Graphene for high-

performance microbial fuel cells," *ACS Nano*, vol. 6, no. 3, pp. 2394–2400, 2012.

[125] S. Zhao, Y. Li, H. Yin, Z. Liu, E. Luan, F. Zhao, Z. Tang, and S. Liu, "Three-dimensional graphene/Pt nanoparticle composites as freestanding anode for enhancing performance of microbial fuel cells," *Sci. Adv.*, vol. 1, no. 10, pp. e1500372–e1500372, 2015.

[126] T. Kuilla, S. Bhadra, D. Yao, N. H. Kim, S. Bose, and J. H. Lee, "Recent advances in graphene based polymer composites," *Prog. Polym. Sci.*, vol. 35, no. 11, pp. 1350–1375, 2010.

[127] B. Luo, S. Liu, and L. Zhi, "Chemical approaches toward graphene-based nanomaterials and their applications in energy-related areas," *Small*, vol. 8, no. Xx, pp. 630–646, 2012.

[128] K. Coleman and R. S. Edwards, "Graphene synthesis: Relationship to applications," *Nanoscale*, pp. 38–51, 2012.

[129] Z. Zhang, F. Xiao, and S. Wang, "Hierarchically structured MnO_2/graphene/carbon fiber and porous graphene hydrogel wrapped copper wire for fiber-based flexible all-solid-state asymmetric supercapacitors," *J. Mater. Chem. A*, vol. 3, no. 21, pp. 11215–11223, 2015.

[130] J. S. Lee, S. I. Kim, J. C. Yoon, and J. H. Jang, "Chemical vapor deposition of mesoporous graphene nanoballs for supercapacitor," *ACS Nano*, vol. 7, no. 7, pp. 6047–6055, 2013.

[131] Z. Zhang, F. Xiao, L. Qian, J. Xiao, S. Wang, and Y. Liu, "Facile Synthesis of 3D MnO_2-Graphene and Carbon Nanotube-Graphene Composite Networks for High-Performance, Flexible, All-Solid-State Asymmetric Supercapacitors," *Adv. Energy Mater.*, vol. 4, no. 10, p. n/a-n/a, 2014.

[132] Z. Liu, Z. Tu, Y. Li, F. Yang, S. Han, W. Yang, L. Zhang, G. Wang, C. Xu, and J. Gao, "Synthesis of three-dimensional graphene from petroleum asphalt by chemical vapor deposition," *Mater. Lett.*, vol. 122, pp. 285–288, May 2014.

[133] J. Yoo, S. P. Patole, and H. Lee, "Method for fabricating three dimensional graphene structures using catalyst templates," US20120128573 A1, 2012.

[134] P. Guo, H. Song, and X. Chen, "Hollow graphene oxide spheres self-assembled by W/O emulsion," *J. Mater. Chem.*, vol. 20, no. 45 mL, p. 4867, 2010.

[135] Z. Zhang, F. Xiao, Y. Guo, S. Wang, and Y. Liu, "One-pot self-assembled three-dimensional TiO2-graphene hydrogel with improved adsorption capacities and photocatalytic and electrochemical activities," *ACS Appl. Mater. Interfaces*, vol. 5, pp. 2227–2233, 2013.

[136] Z. Zhang, L. Wang, J. Xiao, F. Xiao, and S. Wang, "One-Pot Synthesis of Three-Dimensional Graphene/Carbon Nanotube/SnO_2 Hybrid Architectures with Enhanced Lithium Storage Properties," *ACS Appl. Mater. Interfaces*, vol. 7, no. 32, pp. 17963–17968, 2015.

[137] Z. Zhang, G. Chen, H. Wang, and W. Zhai, "Enhanced thermoelectric property by the construction of a nanocomposite 3D interconnected architecture consisting of graphene nanolayers sandwiched by polypyrrole nanowires," *J. Mater. Chem. C*, vol. 3, no. 8, pp. 1649–1654, 2015.

[138] K. Xu, G. Chen, and D. Qiu, "Convenient construction of poly(3,4-ethylenedioxythiophene)–graphene pie-like structure with enhanced thermoelectric performance," *J. Mater. Chem. A*, vol. 1, no. 40, p. 12395, 2013.

[139] K. Xu, G. Chen, and D. Qiu, "In Situ Chemical Oxidative Polymerization Preparation of Poly(3,4-ethylenedioxythiophene)/Graphene Nanocomposites with Enhanced Thermoelectric Performance," *Chem. - An Asian J.*, vol. 10, no. 5, pp. 1225–1231, 2015.

[140] K. Chi, Z. Zhang, J. Xi, Y. Huang, F. Xiao, S. Wang, and Y. Liu, "Freestanding graphene paper supported three-dimensional porous graphene-polyaniline nanocomposite synthesized by inkjet printing and in flexible all-solid-state supercapacitor," *ACS Appl. Mater. Interfaces*, vol. 6, no. 18, pp. 16312–16319, 2014.

[141] Z. Zhang, F. Xiao, J. Xiao, and S. Wang, "Functionalized carbonaceous fibers for high performance flexible all-solid-state asymmetric supercapacitors," *J. Mater. Chem. A*, vol. 3, no. 22, pp. 11817–11823, 2015.

[142] L. Wu, H. Feng, M. Liu, K. Zhang, and J. Li, "Graphene-based hollow spheres as efficient electrocatalysts for oxygen reduction.," *Nanoscale*, vol. 5, no. 22, pp. 10839–43, 2013.

[143] Z. Zhang, F. Xiao, J. Xi, T. Sun, S. Xiao, H. Wang, S. Wang, and Y. Liu, "Encapsulating pd nanoparticles in double-shelled graphene@carbon hollow spheres for excellent chemical catalytic property.," *Sci. Rep.*, vol. 4, p. 4053, 2014.

[144] Y. Xu, Y. Zhu, F. Han, C. Luo, and C. Wang, "3D Si/C fiber paper electrodes fabricated using a combined electrospray/electrospinning technique for Li-ion batteries," *Adv. Energy Mater.*, pp. 1–7, 2014.

[145] Z. Sun, E. Zussman, A. L. Yarin, J. H. Wendorff, and A. Greiner, "Compound Core-Shell Polymer Nanofibers by Co-Electrospinning," *Adv. Mater.*, vol. 15, no. 22, pp. 1929–1932, 2003.

[146] a. K. Moghe and B. S. Gupta, "Co-axial Electrospinning for Nanofiber Structures: Preparation and Applications," *Polym. Rev.*, vol. 48, no. February 2015, pp. 353–377, 2008.

[147] C.-J. Lin, C.-L. Liu, and W.-C. Chen, "Poly(3-hexylthiophene)/Graphene Composites based Aligned Nanofibers for High Performance Field Effect Transistors," *J. Mater. Chem. C*, 2015.

[148] S. Shilpa, B. M. Basavaraja, S. B. Majumder, and A. Sharma, "Electrospun hollow glassy carbon–reduced graphene oxide nanofibers with encapsulated ZnO nanoparticles: a free standing anode for Li-ion batteries," *J. Mater. Chem. A*, vol. 3, no. 10, pp. 5344–5351,

2015.

[149] G. Eda and S. Shivkumar, "Bead structure variations during electrospinning of polystyrene," *J. Mater. Sci.*, vol. 41, pp. 5704–5708, 2006.

[150] K. H. Yoon, J. Unyong, and C. C. Eun, "Production of uniform-sized polymer core-shell microcapsules by coaxial electrospraying," *Langmuir*, vol. 24, no. 14, pp. 2446–2451, 2008.

[151] M. S. a Rahaman, a. F. Ismail, and a. Mustafa, "A review of heat treatment on polyacrylonitrile fiber," *Polym. Degrad. Stab.*, vol. 92, pp. 1421–1432, 2007.

[152] R. H. Colby, "Structure and linear viscoelasticity of flexible polymer solutions: Comparison of polyelectrolyte and neutral polymer solutions," *Rheol. Acta*, vol. 49, pp. 425–442, 2010.

[153] D. Li, M. B. Müller, S. Gilje, R. B. Kaner, and G. G. Wallace, "Processable aqueous dispersions of graphene nanosheets.," *Nat. Nanotechnol.*, vol. 3, pp. 101–105, 2008.

[154] B. S. Okan, A. Yürüm, N. Gorgülü, S. A. Gürsel, and Y. Yürüm, "Polypyrrole coated thermally exfoliated graphite nanoplatelets and the effect of oxygen surface groups on the interaction of platinum catalysts with graphene-based nanocomposites," *Ind. Eng. Chem. Res.*, vol. 50, pp. 12562–12571, 2011.

[155] T. N. Blanton and D. Majumdar, "X-ray diffraction characterization of polymer intercalated graphite oxide," *Powder Diffr.*, vol. 27, no. 2, pp. 104–107, Jun. 2012.

[156] R. Zhang, Y. Hu, J. Xu, W. Fan, and Z. Chen, "Flammability and thermal stability studies of styrene–butyl acrylate copolymer/graphite oxide nanocomposite," *Polym. Degrad. Stab.*, vol. 85, no. 1, pp. 583–588, Jul. 2004.

[157] A. Palm, "Raman Spectrum of Polystyrene.," *J. Phys. Chem.*, vol. 55, pp. 1320–1324, 1951.

[158] A. Arinstein and E. Zussman, "Electrospun polymer nanofibers: Mechanical and thermodynamic perspectives," *J. Polym. Sci. Part B Polym. Phys.*, vol. 49, pp. 691–707, 2011.

[159] J. McDonald-Wharry, M. Manley-Harris, and K. Pickering, "Carbonisation of biomass-derived chars and the thermal reduction of a graphene oxide sample studied using Raman spectroscopy," *Carbon N. Y.*, vol. 59, pp. 383–405, 2013.

[160] M. Naebe, J. Wang, A. Amini, H. Khayyam, N. Hameed, L. H. Li, Y. Chen, and B. Fox, "Mechanical property and structure of covalent functionalised graphene/epoxy nanocomposites.," *Sci. Rep.*, vol. 4, p. 4375, 2014.

[161] S. Lee, J. Kim, B. C. Ku, J. Kim, and H. I. Joh, "Structural Evolution of Polyacrylonitrile Fibers in Stabilization and Carbonization," *Adv. Chem. Eng. Sci.*, vol. 2, no. 2, pp. 275–

282, 2012.

[162] D. A. C. Brownson, D. K. Kampouris, and C. E. Banks, "An overview of graphene in energy production and storage applications," *J. Power Sources*, vol. 196, no. 11, pp. 4873–4885, 2011.

[163] G. W. Zhou, J. Wang, P. Gao, X. Yang, Y. S. He, X. Z. Liao, J. Yang, and Z. F. Ma, "Facile spray drying route for the three-dimensional graphene-encapsulated Fe2O3 nanoparticles for lithium ion battery anodes," *Ind. Eng. Chem. Res.*, vol. 52, pp. 1197–1204, 2013.

[164] J. K. Gan, Y. S. Lim, A. Pandikumar, N. M. Huang, and H. N. Lim, "Graphene/polypyrrole-coated carbon nanofiber core–shell architecture electrode for electrochemical capacitors," *RSC Adv.*, vol. 5, pp. 12692–12699, 2015.

[165] Z. Niu, J. Chen, H. H. Hng, J. Ma, and X. Chen, "A leavening strategy to prepare reduced graphene oxide foams," *Adv. Mater.*, vol. 24, pp. 4144–4150, 2012.

[166] X. Xu, Y. Liu, M. Wang, C. Zhu, T. Lu, R. Zhao, and L. Pan, "Hierarchical hybrids with microporous carbon spheres decorated three-dimensional graphene frameworks for capacitive applications in supercapacitor and deionization," *Electrochim. Acta*, vol. 193, pp. 88–95, 2016.

[167] Y. Z. Menceloglu, B. Saner Okan, and M. Yildiz, "Method For Production of Three-Dimensional Closed Graphene-Based Nano-/Microstructures," US9,850,572(B2), 2017.

[168] J. S. Monfared Zanjani, B. S. Okan, I. Letofsky-Papst, Y. Menceloglu, and M. Yildiz, "Repeated self-healing of nano and micro scale cracks in epoxy based composites by tri-axial electrospun fibers including different healing agents," *RSC Adv.*, vol. 5, no. 89, pp. 73133–73145, 2015.

[169] B. H. Kim and K. S. Yang, "Structure and electrochemical properties of electrospun carbon fiber composites containing graphene," *J. Ind. Eng. Chem.*, vol. 20, no. 5, pp. 3474–3479, Sep. 2014.

[170] T. H. Kao, C. C. Cheng, C. F. Huang, and J. K. Chen, "Using coaxial electrospinning to fabricate core/shell-structured polyacrylonitrile–polybenzoxazine fibers as nonfouling membranes," *RSC Adv.*, vol. 5, no. 72, pp. 58760–58771, 2015.

[171] L. Kou, T. Huang, B. Zheng, Y. Han, X. Zhao, K. Gopalsamy, H. Sun, and C. Gao, "Coaxial wet-spun yarn supercapacitors for high-energy density and safe wearable electronics.," *Nat. Commun.*, vol. 5, no. May, p. 3754, 2014.

[172] Y. Yan, T. Wang, X. Li, H. Pang, and H. Xue, "Noble metal-based materials in high-performance supercapacitors," *Inorg. Chem. Front.*, vol. 4, no. 1, pp. 33–51, 2017.

[173] V. Nallathambi, J.-W. Lee, S. P. Kumaraguru, G. Wu, and B. N. Popov, "Development of high performance carbon composite catalyst for oxygen reduction reaction in PEM Proton

Exchange Membrane fuel cells," *J. Power Sources*, vol. 183, no. 1, pp. 34–42, Aug. 2008.

[174] D. Zhang, X. Zhang, Y. Chen, C. Wang, Y. Ma, H. Dong, L. Jiang, Q. Meng, and W. Hu, "Supercapacitor electrodes with especially high rate capability and cyclability based on a novel Pt nanosphere and cysteine-generated graphene," *Phys. Chem. Chem. Phys.*, vol. 14, p. 10899, 2012.

[175] J. Villermaux and L. Blavier, "Free radical polymerization engineering—I," *Chem. Eng. Sci.*, vol. 39, no. 1, pp. 87–99, 1984.

[176] M. M. Demir, M. A. Gulgun, Y. Z. Menceloglu, S. S. Abramchuk, E. E. Makhaeva, A. R. Khokhlov, V. G. Matveeva, and M. G. Sulman, "Palladium Nanoparticles by Electrospinning from Poly (acrylonitrile- co -acrylic acid) - PdCl 2 Solutions . Relations between Preparation Conditions , Particle Size , and Catalytic Activity," *Macromolecules*, vol. 37, pp. 1787–1792, 2004.

[177] J. . Deitzel, J. Kleinmeyer, D. Harris, and N. C. Beck Tan, "The effect of processing variables on the morphology of electrospun nanofibers and textiles," *Polymer (Guildf).*, vol. 42, no. 1, pp. 261–272, 2001.

[178] J. S. Monfared Zanjani, B. S. Okan, Y. Z. Menceloglu, and M. Yildiz, "Nano-engineered design and manufacturing of high-performance epoxy matrix composites with carbon fiber/selectively integrated graphene as multi-scale reinforcements," *RSC Adv.*, vol. 6, no. 12, pp. 9495–9506, 2016.

[179] D. H. Reneker and A. L. Yarin, "Electrospinning jets and polymer nanofibers," *Polymer (Guildf).*, vol. 49, no. 10, pp. 2387–2425, 2008.

[180] Y. Dzenis, "Spinning continious fibers for nanotechnology," *Science (80-.).*, vol. 304, no. June, pp. 1917–1919, 2004.

[181] R. Sellin, C. Grolleau, S. Arrii-Clacens, S. Pronier, J. M. Clacens, C. Coutanceau, and J. M. Léger, "Effects of temperature and atmosphere on carbon-supported platinum fuel cell catalysts," *J. Phys. Chem. C*, vol. 113, no. 52, pp. 21735–21744, 2009.

[182] V. L. Nguyen, M. Ohtaki, V. N. Ngo, M. T. Cao, and M. Nogami, "Structure and morphology of platinum nanoparticles with critical new issues of low- and high-index facets," *Adv. Nat. Sci. Nanosci. Nanotechnol.*, vol. 3, no. 2, p. 25005, 2012.

[183] G. Eda and M. Chhowalla, "Graphene-based Composite Thin Films for Electronics," *Nano Lett.*, vol. 9, no. 2, pp. 814–818, 2009.

[184] M. Sudan Saha and J. Zhang, "Carbon nanotubes and nanofibers and their supported catalysts for direct methanol fuel cells," in *Nanostructured and Advanced Materials for Fuel Cells*, Boca Raton: CRC Press, 2013, pp. 444–467.

[185] Z. Lei, L. Lu, and X. S. Zhao, "The electrocapacitive properties of graphene oxide reduced by urea," *Energy Environ. Sci.*, vol. 5, no. 4, pp. 6391–6399, 2012.

[186] X. Yang, H. Niu, H. Jiang, Q. Wang, and F. Qu, "High energy density all-solid-state asymmetric supercapacitor based on MoS2/graphene nanosheet and MnO2/graphene hybrid electrodes," *J. Mater. Chem. A*, vol. 4, pp. 11264–11275, 2016.

[187] X. Fan, X. Chen, and L. Dai, "3D graphene based materials for energy storage," *Curr. Opin. Colloid Interface Sci.*, vol. 20, no. 5–6, pp. 429–438, 2015.

[188] M. Yang, J. M. Jeong, Y. S. Huh, and B. G. Choi, "High-performance supercapacitor based on three-dimensional MoS2/graphene aerogel composites," *Compos. Sci. Technol.*, vol. 121, pp. 123–128, 2015.

[189] K. Shen, F. Ran, X. Zhang, C. Liu, N. Wang, X. Niu, Y. Liu, D. Zhang, L. Kong, L. Kang, and S. Chen, "Supercapacitor electrodes based on nano-polyaniline deposited on hollow carbon spheres derived from cross-linked co-polymers," *Synth. Met.*, vol. 209, pp. 369–376, 2015.

[190] M. F. El-Kady, M. Ihns, M. Li, J. Y. Hwang, M. F. Mousavi, L. Chaney, A. T. Lech, and R. B. Kaner, "Engineering three-dimensional hybrid supercapacitors and microsupercapacitors for high-performance integrated energy storage," *Proc. Natl. Acad. Sci.*, vol. 112, no. 14, p. 201420398, 2015.

[191] A. Borenstein, O. Hanna, R. Attias, S. Luski, T. Brousse, and D. Aurbach, "Carbon-based composite materials for supercapacitor electrodes: a review," *J. Mater. Chem. A*, vol. 5, no. 25, pp. 12653–12672, 2017.

[192] W. Chen, X. Tao, Y. Li, H. Wang, D. Wei, and C. Ban, "Hydrothermal synthesis of graphene-MnO2-polyaniline composite and its electrochemical performance," *J. Mater. Sci. Mater. Electron.*, vol. 27, no. 7, pp. 6816–6822, 2016.

[193] G. Han, Y. Liu, L. Zhang, E. Kan, S. Zhang, J. Tang, and W. Tang, "MnO2 nanorods intercalating graphene oxide/polyaniline ternary composites for robust high-performance supercapacitors," *Sci. Rep.*, vol. 4, pp. 1–7, 2014.

[194] M. G. Hosseini and E. Shahryari, "Synthesis, Characterization and Electrochemical Study of Graphene Oxide-Multi Walled Carbon Nanotube-Manganese Oxide-Polyaniline Electrode as Supercapacitor," *J. Mater. Sci. Technol.*, vol. 32, no. 8, pp. 763–773, 2016.

[195] T. Wu, C. Wang, Y. Mo, X. Wang, J. Fan, Q. Xu, and Y. Min, "A ternary composite with manganese dioxide nanorods and graphene nanoribbons embedded in a polyaniline matrix for high-performance supercapacitors," *RSC Adv.*, vol. 7, no. 53, pp. 33591–33599, 2017.

[196] W. Huang, T. Yao, Q. Hao, W. Wang, X. Xia, and X. Wang, "Synthesis and electrochemical properties of graphene oxide/manganese oxide/polyaniline and its reduced composites," *RSC Adv.*, vol. 4, no. 100, pp. 56615–56624, 2014.

[197] L. Haghighi Poudeh, D. Cakiroglu, F. Ç. Cebeci, M. Yildiz, Y. Z. Menceloglu, and B. Saner Okan, "Design of Pt-Supported 1D and 3D Multilayer Graphene-Based Structural Composite Electrodes with Controlled Morphology by Core–Shell

Electrospinning/Electrospraying," *ACS Omega*, vol. 3, no. 6, pp. 6400–6410, Jun. 2018.

[198] M. Augustin, D. Fenske, I. Bardenhagen, A. Westphal, M. Knipper, T. Plaggenborg, J. Kolny-Olesiak, and J. Parisi, "Manganese oxide phases and morphologies: A study on calcination temperature and atmospheric dependence.," *Beilstein J. Nanotechnol.*, vol. 6, pp. 47–59, Jan. 2015.

[199] I. Stamatin, A. Morozan, A. Dumitru, V. Ciupina, G. Prodan, J. Niewolski, and H. Figiel, "The synthesis of multi-walled carbon nanotubes (MWNTs) by catalytic pyrolysis of the phenol-formaldehyde resins," *Phys. E Low-Dimensional Syst. Nanostructures*, vol. 37, no. 1–2, pp. 44–48, 2007.

[200] W. E. Estes, J. R. Wasson, J. W. Hall, and W. E. Hatfield, "Characterization of some mixed-halide copper(II) dimers of the general formula [Cu2XnX'6-n]2- (X = chloride(1-) and X' = bromide(1])): evidence for the preference of chloride bridges in the mixed-halide species," *Inorg. Chem.*, vol. 17, no. 12, pp. 3657–3664, Dec. 1978.

[201] H. Wang, L. Ma, M. Gan, T. Zhou, X. Sun, W. Dai, H. Wang, and S. Wang, "Design and assembly of reduced graphene oxide/polyaniline/urchin-like mesoporous TiO2 spheres ternary composite and its application in supercapacitors," *Compos. Part B Eng.*, vol. 92, pp. 405–412, May 2016.

[202] M. Ullah, J. Seyyed Monfared Zanjani, L. Haghighi Poudeh, M. Siddiq, B. Saner Okan, M. Yıldız, and Y. Menceloglu, "Manufacturing functionalized mono-crystalline diamond containing electrospun fibers reinforced epoxy composites with improved mechanical characteristics," *Diam. Relat. Mater.*, vol. 76, no. January, pp. 90–96, 2017.

[203] Y. Wang, Z. Ji, X. Shen, K. Xu, and A. Yuan, "Facile synthesis of Mn3O4/reduced graphene oxide nanocomposites with enhanced capacitive performance," *J. Alloys Compd.*, vol. 684, pp. 366–371, 2016.

[204] K. Ghosh, C. Y. Yue, M. M. Sk, and R. K. Jena, "Development of 3D Urchin-Shaped Coaxial Manganese Dioxide@Polyaniline (MnO2@PANI) Composite and Self-Assembled 3D Pillared Graphene Foam for Asymmetric All-Solid-State Flexible Supercapacitor Application," *ACS Appl. Mater. Interfaces*, vol. 9, no. 18, pp. 15350–15363, 2017.

[205] K. Wu, Q. Zeng, B. Zhang, X. Leng, D. Su, I. R. Gentle, and D.-W. Wang, "Structural Origin of the Activity in Mn 3 O 4 -Graphene Oxide Hybrid Electrocatalysts for the Oxygen Reduction Reaction," *ChemSusChem*, vol. 8, no. 19, pp. 3331–3339, 2015.

[206] R. K. Agrawalla, S. Paul, P. K. Sahoo, A. K. Chakraborty, and A. K. Mitra, "A facile synthesis of a novel three-phase nanocomposite: Single-wall carbon nanotube/silver nanohybrid fibers embedded in sulfonated polyaniline," *J. Appl. Polym. Sci.*, p. n/a-n/a, Nov. 2014.

[207] Q. Zhou, Y. Li, L. Huang, C. Li, and G. Shi, "Three-dimensional porous graphene/polyaniline composites for high-rate electrochemical capacitors," *J. Mater.*

Chem. A, vol. 2, no. 41, pp. 17489–17494, 2014.

[208] G. Z. Chen, "Understanding supercapacitors based on nano-hybrid materials with interfacial conjugation," *Prog. Nat. Sci. Mater. Int.*, vol. 23, no. 3, pp. 245–255, 2013.

[209] Y. X. Du, X. Zhao, Z. L. Huang, Y. Z. Li, and Q. H. Zhang, "Freestanding composite electrodes of MnOx embedded carbon nanofibers for high-performance supercapacitors," *Rsc Adv.*, vol. 4, no. 74, pp. 39087–39094, 2014.

APPENDIX A

(a)   (b)   (c)
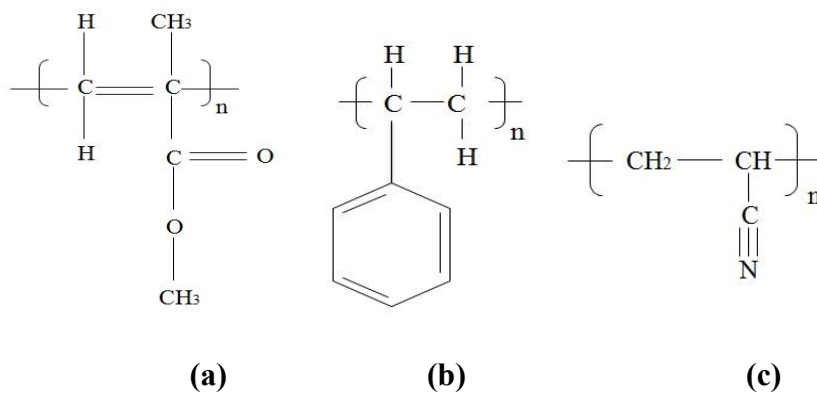
Appendix A1 The Chemical structures of (a) PMMA, (b) PS, and (c) PAN polymers

Appendix A2 Electrospraying parameters of PS-TEGO, PMMA-TEGO, and PAN-TEGO spheres

Polymer type	Polymer concentration (wt%)	Solvent	TEGO amount (wt%)	Flowrate (μL/min)	Voltage (kV)	Distance (cm)
PMMA	20	DMF	0	13	13	10
	20	DMF	0.005	17	15	10
	20	DMF	0.01	18	16	10
	20	DMF	0.02	17	15	10
PS	20	DMF	0	13	13	10
	20	DMF	0.005	16	16	10
	20	DMF	0.01	17	16	10
	20	DMF	0.02	17	16	10
PAN	5	DMF	0	15	13	10
	5	DMF	0.02	18	15	10
	3.5	DMF	0.05	14	13	10

Appendix A3 The positions and intensities of D, G, 2D peaks, I_D/I_G and I_G/I_{2D} values of untreated TEGO, sonicated and electrosprayed TEGO

	D		G		2D		I_D/I_G	I_G/I_{2D}
	Position (cm^{-1})	Intensity (a.u.)	Position (cm^{-1})	Intensity (a.u.)	Position (cm^{-1})	Intensity (a.u.)		
TEGO	1346	4297	1575	20033	2713	8590	0.2	2.3
Sonicated TEGO	1352	2047	1578	18346	2717	9111	0.2	2.0
Electrosprayed TEGO	-	-	1581	24014	2721	11829	-	2.0

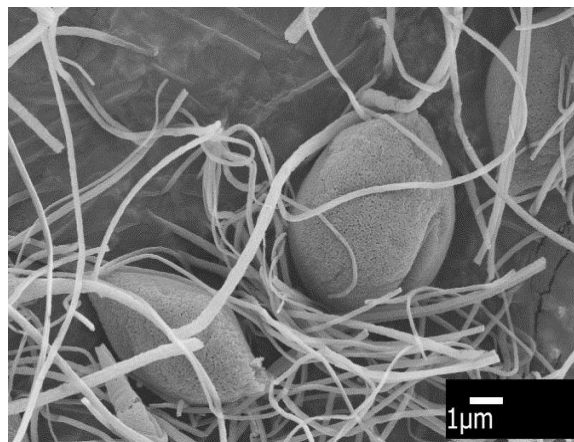**Appendix A4** Mark-Houwink-Sakurada constants for PMMA, PS, and PAN polymers at room temperature.

Polymer type	Solvent	a	K_H (10^{-3} mL/g)
PMMA	DMF	0.625	25
PS	DMF	0.603	31.8
PAN	DMF	0.780	17.7

Appendix A5 XRD diffraction peak intensities and positions of TEGO based PMMA and PS based spheres

|	TEGO amount (wt%)	XRD polymer peak intensity	2θ of polymer peak
PMMA	0	305	14.4
	0.005	287	13.9
	0.01	189	13.7
	0.02	184	13.5
PS	0	205	19.9
	0.005	169	19.6
	0.01	152	19.5
	0.02	150	19.2

Appendix A6 Raman intensities of PS and PS-0.02 wt% TEGO spheres

TEGO amount (wt%)	Intensity of 3050 cm^{-1} peak	Intensity of 2900 cm^{-1} peak	Intensity of 1600 cm^{-1} peak	Intensity of 995 cm^{-1} peak
0	48003	22031	9870	66635
0.02	14170	7269	3701	21170

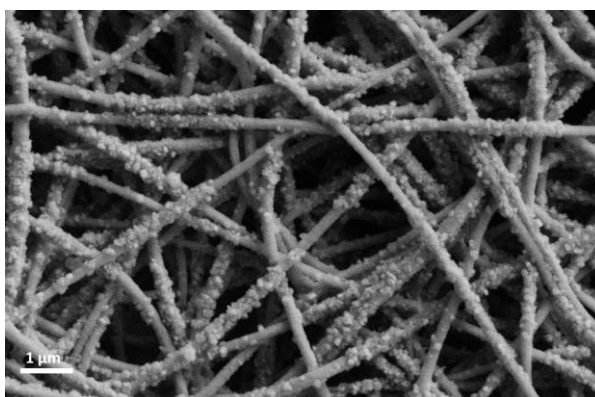**Appendix A7** SEM image of PMMA spheres containing 0.02 wt% TEGO using methanol as a core material with the flow rate of 5 µL/min
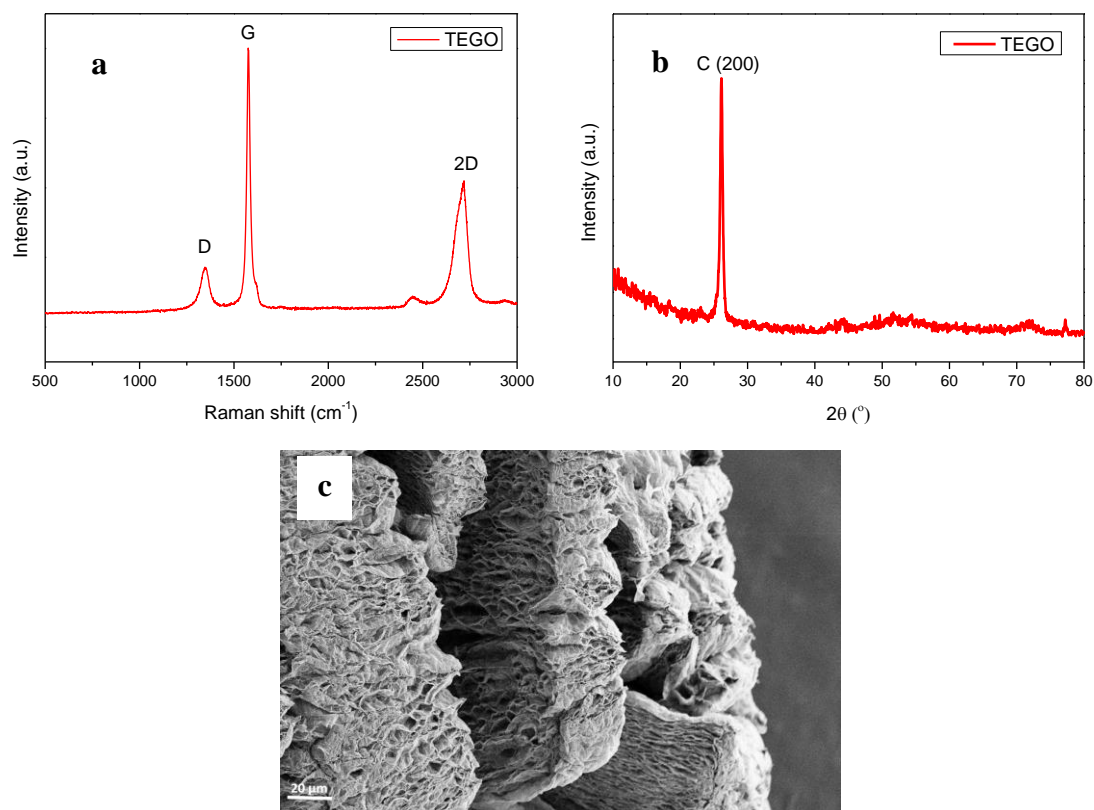
APPENDIX B

Appendix B1 Characterization results of as received TEGO: **(a)** Raman spectrum, **(b)** XRD spectrum, and **(c)** SEM image.

BET surface area of TEGO is 11 m^2/g.

Appendix B2 SEM image of graphene-based fibers containing 0.1 wt% Pt

117

Mark-Houwink-Sakurada equations:

$$C* = 1/[\eta] \qquad (1)$$

$$[\eta] = K_H M^a \qquad (2)$$

Appendix B3 Mark-Houwink-Sakurada constants for PAN polymers at room temperature.

Polymer type	Solvent	a	K_H (10^{-3} mL/g)
PAN	DMF	0.780	17.7

where C* corresponds to the solution concentration where the hydrodynamic volumes begin to overlap and C_e is the entanglement concentration which separates the semi-dilute unentangled and semi-dilute entangled regimes. C_e value is approximately equal to 10C* for neutral polymers in good solvent systems. By combining (1) and (2) the following expression can be obtained:

$$C* = 5.65 \times 10^4 Mw^{-0.780}$$
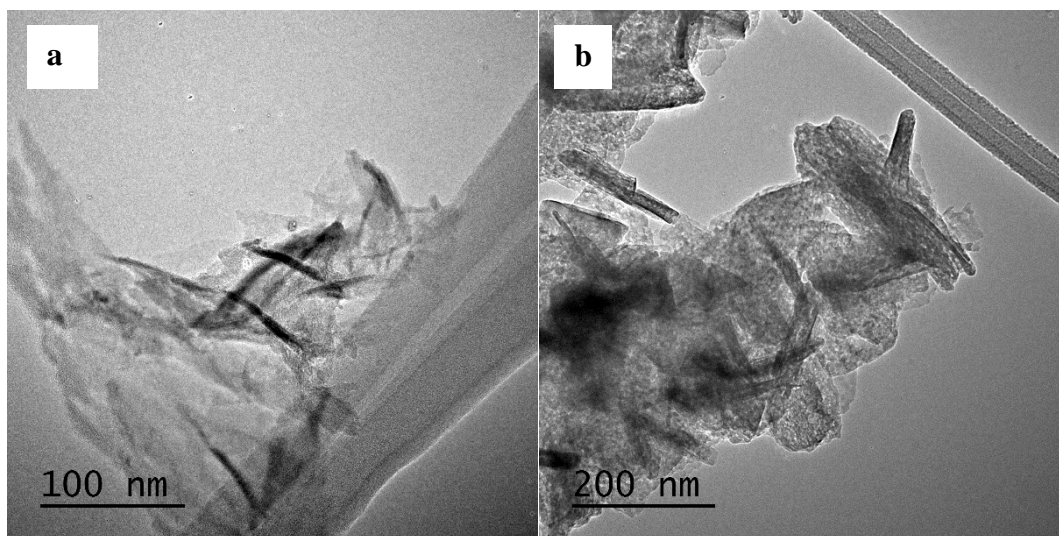
Appendix B4 (a) and **(b)** TEM images of Pt decorated graphene-based fibers at different regions.
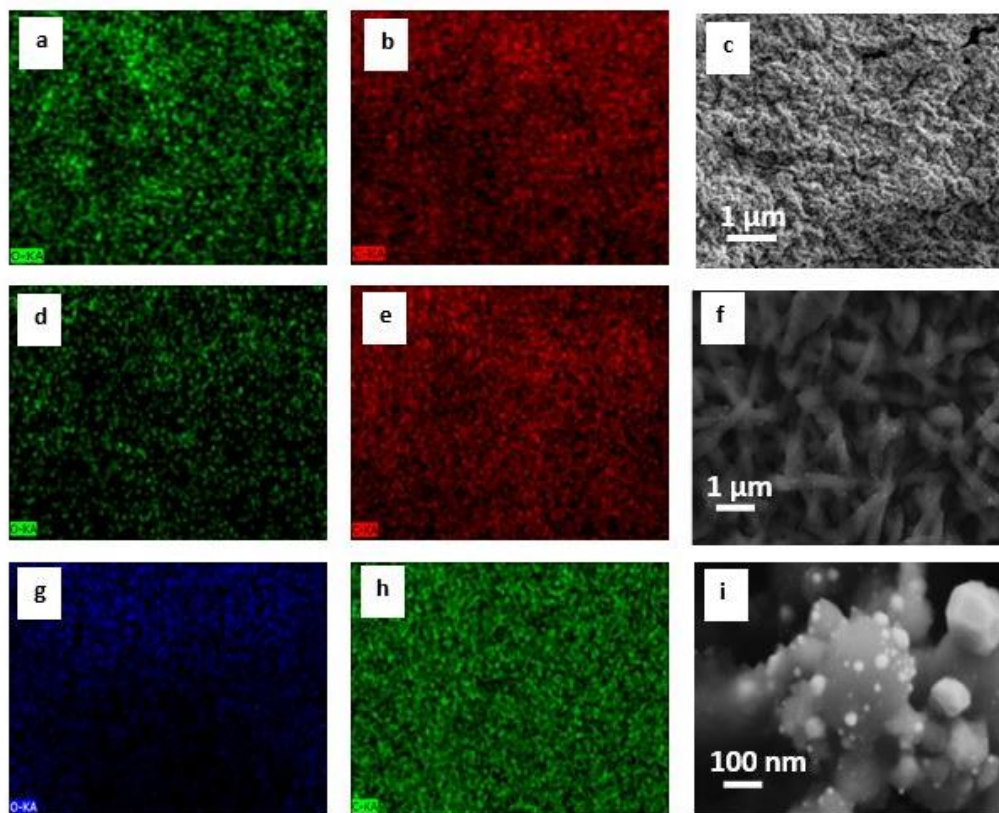
Appendix B5. Elemental mapping images of **(a)** oxygen and **(b)** carbon and **(c)** SEM image of Pt decorated graphene-based foam, elemental mapping of **(d)** oxygen and **(e)** carbon and **(f)** SEM image of Pt decorated graphene-based fiber, elemental mapping of **(g)** oxygen and **(h)** carbon and **(i)** SEM image of Pt decorated graphene-based spheres.

Appendix B6 Elemental analysis of the Pt-graphene-based foam, fibers, and spheres

Pt decorated graphene-based structures	C (wt%)	O (wt%)	Pt (wt%)
Foam	61	30	9
Fibers	70	25	5
Spheres	39	41	20
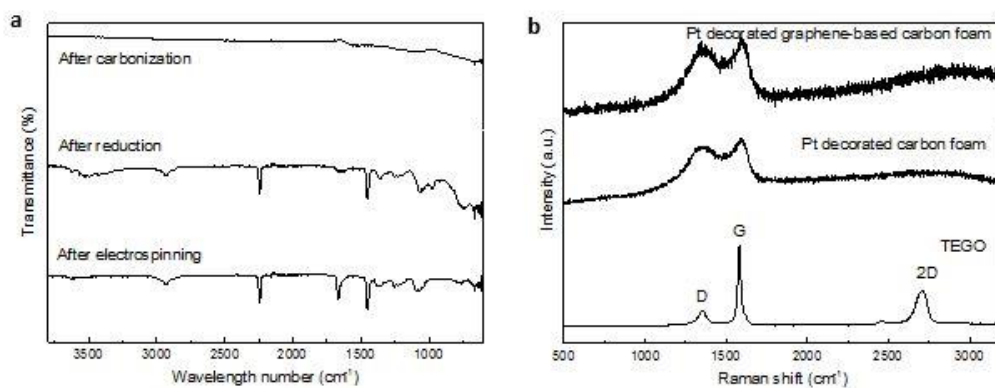
Appendix B7 (a) FTIR spectra of neat, reduced, and carbonized Pt decorated graphene-based foam, and **(b)** Raman spectra of TEGO, Pt decorated carbon foam without graphene and Pt decorated graphene-based carbon foam
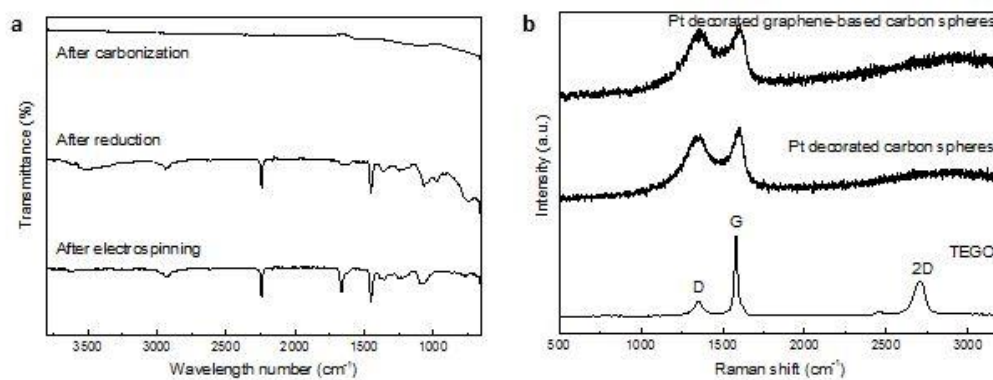
Appendix B8 (a) FTIR spectra of neat, reduced, and carbonized Pt decorated graphene-based spheres, and **(b)** Raman spectra of TEGO, Pt decorated carbon spheres without graphene and Pt decorated graphene-based carbon spheres
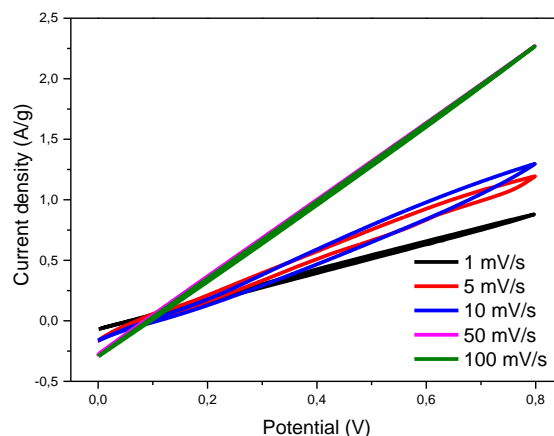
Appendix B9 CV plots of Pt decorated neat TEGO sheets at different scan rates of 1, 5, 10, 50, and 100 mv/s.

The coulombic efficiency of the structures, η, were determined using following equation:

$$\eta = t_D/t_C \times 100\% \qquad (3)$$

where, t_D and t_C are discharging and charging times, respectively.

Appendix B10 Coulombic efficiency of Pt decorated graphene-based structures

	Spheres	Fibers	Foam
Coulombic efficiency (%) at a current density of 2 A/g	131	43	80

High coulombic efficiency of sphere structures was attributed to the rapid shrinkage of 3D pores which causes the decomposition of electrodes as time passes. This result was also confirmed by cyclic stability tests in which spheres shows a capacitance loss of 12% after 1000 cycles of charging-discharging.

CURRICULUM VITAE

Leila Haghighi Poudeh

Sabancı University,

Faculty of Engineerings and Natural Sciences,

Orhanlı 34956 Tuzla/İstanbul

Contact: leilah@sabanciuniv.edu

EDUCATION

2014-2018	Ph.D. in Materials Science and Engineering, Sabanci University/Turkey (3.3/4)
2012-2014	M.S. in Materials Science and Engineering-Ceramics, Istanbul Technical University/Turkey (3.2/4)
2006-2011	B.S. in Materials Science and Engineering-Ceramics, Tabriz University/Iran (2.7/4)

WORK EXPERIENCE

2016-2018   **Coordinator teaching assistant**, Sabanci University, *Introduction to materials science*

2014-2018   **Research assistant,** Sabanci University; *SUNUM, SU-IMC*

2014-2016   **Teaching assistant**, Sabanci University, *Differential equations*

2011-2014   **Research assistant,** Istanbul Technical University, *Particulate materials laboratory (PML)*

RESEARCH EXPERIENCE

2014-2018   **Ph.D. Dissertation**, *Design and manufacturing of dimensionally controlled graphene-based hybrid structures by core-shell electrospinning for energy storage systems*

Prof. Dr. Mehmet Yıldız (advisor) and Assoc Prof. Dr. Burcu Saner Okan (co-advisor), Sabanci University

2012-2014   **M.S. Thesis**, *Production of WO_3-MoO_3-Cr_2O_3 composite powders via spray drying and their sintering behavior*

Assoc. Prof. Dr. Burak Özkal (advisor), Istanbul Technical University

2006-2011   **B.S. Thesis**, *The effect of Chromite-Silica sands on the performance of ladle filler sands for continuous casting*

Prof. Dr. Mahdi Kakroudi (advisor), Tabriz University

PUBLICATIONS

1. **Haghighi Poudeh, Leila** and Cakmak Cebeci, Fevzi and Menceloglu, Yusuf Z and Yildiz, Mehmet and Saner Okan, Burcu. "*Free-Standing Hierarchical Hybrid Electrodes Based on PANI Coated Mn_3O_4/Graphene Embedded Carbon Fibers for High Performance Supercapacitors*", 2018. (Submitted)

2. Çakal Saraç, Elçin and **Haghighi Poudeh, Leila** and Seyyed Monfared Zanjani, Jamal and Pehlivan, Zeki Semih and Çakmak Cebeci, Fevzi and Aydin, İsmail, and Menceloglu, Yusuf and Saner Okan, Burcu. "*Investigation of synergetic effect of CVD grown carbon fiber on graphene as a bicomponent reinforcement on the structural, thermal and mechanical properties of polyamide 6.6 nanocomposites*", 2018. (Submitted)

3. Seyyed Monfared Zanjani, Jamal and **Haghighi Poudeh, Leila**, and Girginer Ozunlu, Burcu, and Yagcı, Yavuz Emre, and Menceloglu, Yusuf, and Saner Okan, Burcu "*The effect of graphene nanoplatelets on crystallization and mechanical reinforcement*

behaviors of homo- and co-polymer polypropylene based nanocomposites", 2018. (Submitted)

4. **Haghighi Poudeh, Leila** and Cakiroglu, Dilek and Cakmak Cebeci, Fevzi and Yildiz, Mehmet and Menceloglu, Yusuf Z and Saner Okan, Burcu. "*Design of Pt supported 1D and 3D multi-layer graphene-based structural composite electrodes with controlled morphology by core-shell electrospinning/electrospraying*". ACS Omega, 2018, Vol 3, pages 6400-6410.

5. Ullah ,Mohib and Seyyed Monfared Zanjani, Jamal and **Haghighi Poudeh, Leila** and Siddiq, Mohammad and Saner Okan, Burcu and Yıldız, Mehmet and Menceloglu, Yusuf Z. "*Manufacturing functionalized mono-crystalline diamond containing electrospun fibers reinforced epoxy composites with improved mechanical characteristics*". Diamond and Related Materials, 2017, Vol.76, pages 90-96.

6. **Haghighi Poudeh, Leila** and Saner Okan, Burcu and Seyyed Monfared Zanjani, Jamal and Yıldız, Mehmet and Menceloğlu, Yusuf Z. "*Design and fabrication of hollow and filled graphene-based polymeric spheres via core-shell electrospraying*", RSC Advances, 2015, Vol.5, No.111, 91147-91157.

BOOK CHAPTERS
Haghighi Poudeh, Leila and Yildiz, Mehmet and Menceloglu, Yusuf Z and Saner Okan, Burcu. "*Three-dimensional Graphene Structures, Production Methods Properties, and Applications*". Graphene- Growth, Synthesis and Integration Methods, Handbook on the Graphene Materials, WILEY-Scrivener Publisher, USA, 2018. (accepted-under publication)

CONFERENCES

1. **Haghighi Poudeh, Leila** and Saner Okan, Burcu and Cebeci, Fevzi Cakmak and Yildiz, Mehmet and Menceloglu, Yusuf.Z. "Dimension control of graphene-based composite structures by core-shell electrospinning technology and development of new emerging hybrid electrodes for the energy storage devices" 2. Ulusal Karbon Konferansi, 2018, Istanbul, Turkey.

2. **Haghighi Poudeh, Leila** and Cakiroglu, Dilek and Cebeci, Fevzi Cakmak and Yildiz, Mehmet and Menceloglu, Yusuf.Z and Saner Okan, Burcu. "Design and Fabrication of 3D Graphene Based Composite Structures via Core-shell Electrospinning Technique for Energy Storage Systems". Graphene Week 2017, Athens, Greece.

3. **Haghighi Poudeh, Leila** and Saner Okan, Burcu and Yıldız, Mehmet and Menceloğlu, Yusuf Z. "Platinum decorated 3D/2D Graphene-based composites: New emerging hybrid electrodes in the energy storage systems". 6. Fiziksel Kimya Kongresi, 2017, Zonguldak, Turkey. Oral presentation

4. **Haghighi Poudeh, Leila** and Menceloglu, Yesim and Saner Okan, Burcu and Yıldız, Mehmet and Menceloğlu, Yusuf Z. "Production of Multi-walled Mn3O4-Graphene Based Fibers via Tri-axial Electrospinning: New Generation of Hybrid Electrodes in the Energy Storage Devices". GRAPHENE 3RD Emerging 2D Materials & Graphene Conference 2016, Istanbul, Turkey. Poster presentation

5. Ateş Türkmen, Tülin and **Haghighi Poudeh, Leila** and Saner Okan, Burcu and Altürk Parlak, Elif. "Effect of Graphene Oxide on Organic Photovoltaics". GRAPHENE 3RD Emerging 2D Materials & Graphene Conference 2016, Istanbul, Turkey. Poster presentation

6. **Haghighi Poudeh, Leila** and Saner Okan, Burcu and Seyyed Monfared Zanjani, Jamal and Yıldız, Mehmet and Menceloğlu, Yusuf Z. "Design and Fabrication of Three Dimensional Graphene Spheres with Controlled Hollowness via Core-shell Electrospraying Technique". NanoTR12, 2016, Istanbul, Turkey. Oral presentation

7. **Haghighi Poudeh, Leila** and Saner Okan, Burcu and Seyyed Monfared Zanjani, Jamal and Yıldız, Mehmet and Menceloğlu, Yusuf Z. "Integration of graphene sheets into three dimensional spherical structures with controlled hollowness via core-shell electrospraying technique". Graphene Week 2016, Warsaw, Poland. Poster presentation

8. **Haghighi Poudeh, Leila** and Saner Okan, Burcu and Seyyed Monfared Zanjani, Jamal and Yıldız, Mehmet and Menceloğlu, Yusuf Z. "Hollow and filled graphene-based polymeric spheres via core-shell electrospinning", Graphene-Related Technologies from Laboratory to Industry, 2015, Istanbul, Turkey. Oral presentation

9. **Haghighi Poudeh, Leila** and Saner Okan, Burcu and Yıldız, Mehmet and Menceloğlu, Yusuf Z. "Synthesis and characterization of graphene-based polymeric spheres via tri-axial electrospinning", 2nd Turkey-Japan Workshop on Polymeric Composite Materials, 2015, Çeşme, Izmir, Turkey. Oral presentation

10. Saner Okan, Burcu and Seyyed Monfared Zanjani, Jamal and **Haghighi Poudeh, Leila** and Yıldız, Mehmet and Menceloğlu, Yusuf Z. "Fabrication of graphene-reinforced multi-walled electrospun fibers as reinforcing agent for epoxy composites", COST Action MP1202 scientific workshop, 2014, Istanbul, Turkey. Oral presentation